PARAMETRIC STUDY OF TURBINE BLADE INTERNAL COOLING AND FILM COOLING

A Dissertation

by

AKHILESH PRABHAKAR RALLABANDI

Submitted to the Office of Graduate Studies of
Texas A&M University
in partial fulfillment of the requirements for the degree of

DOCTOR OF PHILOSOPHY

August 2010

Major Subject: Mechanical Engineering

PARAMETRIC STUDY OF TURBINE BLADE INTERNAL COOLING AND

FILM COOLING

A Dissertation

by

AKHILESH PRABHAKAR RALLABANDI

Submitted to the Office of Graduate Studies of
Texas A&M University
in partial fulfillment of the requirements for the degree of

DOCTOR OF PHILOSOPHY

Approved by:

Chair of Committee,	Je-Chin Han
Committee Members,	Sai Lau
	Kumbakonam Rajagopal
	Hamn-Ching Chen
Head of Department,	Dennis O'Neal

August 2010

Major Subject: Mechanical Engineering

ABSTRACT

Parametric Study of Turbine Blade Internal Cooling and Film Cooling . (August 2010)

Akhilesh Prabhakar Rallabandi, B. Tech, Indian Institute of Technology, Madras;

M. Tech, Indian Institute of Technology, Madras

Chair of Advisory Committee: Dr. Je-Chin Han

Gas turbine engines are extensively used in the aviation and power generation industries. They are used as topping cycles in combined cycle power plants, or as stand alone power generation units.

Gains in thermodynamic efficiency can be realized by increasing the turbine inlet temperatures. Since modern turbine inlet temperatures exceed the melting point of the constituent superalloys, it is necessary to provide an aggressive cooling system. Relatively cool air, ducted from the compressor of the engine is used to remove heat from the hot turbine blade. This air flows through passages in the hollow blade (internal cooling), and is also ejected onto the surface of the blade to form an insulating film (film cooling).

Modern land-based gas turbine engines use high Reynolds number internal flow to cool their internal passages. The first part of this study focuses on experiments pertaining to passages with Reynolds numbers of up to 400,000. Common turbulator designs (45degree parallel sharp-edged and round-edged) ribs are studied. Older correlations are found to require corrections in order to be valid in the high Reynolds number parameter space.

The effect of rotation on heat transfer in a typical three-pass serpentine channel is studied using a computational model with near-wall refinement. Results from this computational study indicate that the hub experiences abnormally high heat transfer

under rotation. An experimental study is conducted at Buoyancy numbers similar to an actual engine on a wedge shaped model trailing edge, roughened with pin-fins and equipped with slot ejection. Results show an asymmetery between the leading and trailing surfaces due to rotation - a difference which is subdued due to the provision of pin-fins.

Film cooling effectiveness is measured by the PSP mass transfer analogy technique in two different configurations: a flat plate and a typical high pressure turbine blade. Parameters studied include a step immediately upstream of a row of holes; the Strouhal number (quantifying rotor-stator interaction) and coolant to mainstream density ratio. Results show a deterioration in film cooling effectiveness with on increasing the Strouhal number. Using a coolant with a higher density results in higher film cooling effectiveness.

To Mum, Dad, Vandana and, of course, Radha

ACKNOWLEDGMENTS

First, I would like to acknowledge my advisor, Dr. Je-Chin Han for his guidance through my Ph.D., and for involving me in a wide variety of challenging projects. I would also like to acknowledge Dr. Hamn-Ching Chen for his guidance on various compuational projects. I would like to acknowledge committee members, Dr. Lau, Dr. Rajagopal and Dr. Ranjan for their valuable suggestions and discussions. I am also indebted to all my colleagues at the Turbine Heat Transfer lab, Dr. Yang, Dr. Rhee, Janice, Diganta, Liu, Mike, Jiang, Nawaf, Kevin, Shiou-Jiuan, Josh and Sarah, personnel at the department, Randall Tucker, Eddy Denk, Izzy Ramirez and Jason Caswell. Dr. Don Knuth's TEX has allowed me to survive several deadlines. Last but not least, I would like to acknowledge my wife, Radha, whose support and proof-reading skills have proven to be invaluable during my Ph.D.

NOMENCLATURE

$\bar{f}$ Fanning friction factor

χ Mole fraction

η Film cooling effectiveness, Eq.5.14

Ω Rotating speed of rotating rig (rad/s) or rotating speed of wake rod (rpm), depending on context

ρ Density, kg/m^3

ρ_c Coolant density

ρ_M Mainstream density

Bo Buoyancy number, Eq.4.6

C_D Discharge coefficient, Eq.4.1

d Film cooling hole diameter

DR Coolant to mainstream density ratio

e Rib height

e^+ Roughness Reynolds number, Eq.2.8

f_0 Smooth surface friction factor

G Heat transfer roughness function, Eq.2.10

h Heat transfer coefficient

k_{air} Thermal conductivity of air, W/m^2K

M Blowing (mass flux) ratio

Nu Nusselt number

Nu_0 Nusselt number corresponding to turbulent flow in smooth pipe

Nu_s Measured stationary Nusselt number for same Reynolds number (to show effect of rotation)

P Static pressure, Pa

p Rib-rib pitch

q Heat rate, W Eq.2.2

q''_{loss} Heat loss

R Friction roughness function, Eq.2.9

Ro Rotation number, Eq.4.4

St Stanton number, $St = \frac{Nu}{RePr}$

T_B Bulk mean temperature

T_C Coolant temperature, Eq.5.14

T_f Film temperature, Eq.5.14

T_w Wall temperature

T_∞ Mainstream temperature, Eq.5.14

TP Thermal Performance parameter

V_c Coolant velocity

V_M Mainstream velocity

TABLE OF CONTENTS

LIST OF TABLES

LIST OF FIGURES

CHAPTER I

INTRODUCTION

Gas turbine engines play a central role in modern civilization. They are extensively used in the aviation industry as aircraft engines. They are used in the power-generation industry as topping cycles in combined cycle power plants. They are also used as power-plants for ships. The robust and efficient use of these devices is therefore an economic necessity.

Gas turbine inlet temperatures (Fig.1, modified form [1]) have been increasing over the past few decades due to significant improvements in cooling and material technologies. This trend of increasing blade thermal loading is expected to exacerbate in the future, especially with probable implementation of policies favoring Carbon and Capture and Sequestration.

Two potential methods to sequester CO_2 (based on Cumpsty [2] and Chyu et al. [3] are:

- **IGCC based clean coal technolgies.** Coal is subject to a shift reaction in the gasifier, yielding CO_2 which is immediately ready for sequestration after pressurization. The shift reaction yields a mixture of CO and H_2, a Syngas. The syngas is then used in an efficient combined cycle power plant, with a land-based gas-turbine engine comprising the topping cycle. O

- **Oxy-fuel combustion.** This method involves CO_2 capture in flue gases. Since the concentation of CO_2 is very low in the flue gases, it is very difficult to perform this. A method to increase the concentration of CO_2 is to perform the combustion in the absence of nitrogen (by supplying pure oxygen). Due to the

The journal model is International Journal of Heat and Mass Transfer.

absence of nitrogen as a diluatant, the temperatures reached inside the engine are very high - much higher than those than can be handled by common cooling technolgies. Steam is used as a dilutant instead (because it can be condensed in the flue-gas stream) making carbon capture much easier.

Both the aforementioned methods result in high concentrations of water vapour in the hot-gas, therefore increasing the heat-load on the blade (due to the higher thermal conductivity of water-vapor). It is thus evident that gas turbine is expected to be a very relevant topic in the future also.

In general, gas turbine cooling is achieved by bleeding some relatively cool air from the compressor and using it inside the gas turbine blades to remove heat transferred into the blade from the hot mainstream. The cooling air flows through internal cooling passages inside the blade. These passages are specifically designed to maximize the heat transfer. In modern gas turbine blades, this is usually done by the use of contact area enhancers and turbulence promoters, such as ribs and pin-fins in the passages.

Some of this cooling air is ejected onto the surface of the turbine blade to form an insulating film - with the goal of reducing contact of the blade with the hot mainstream gas. A schematic of both schemes is shown in Fig. 2.
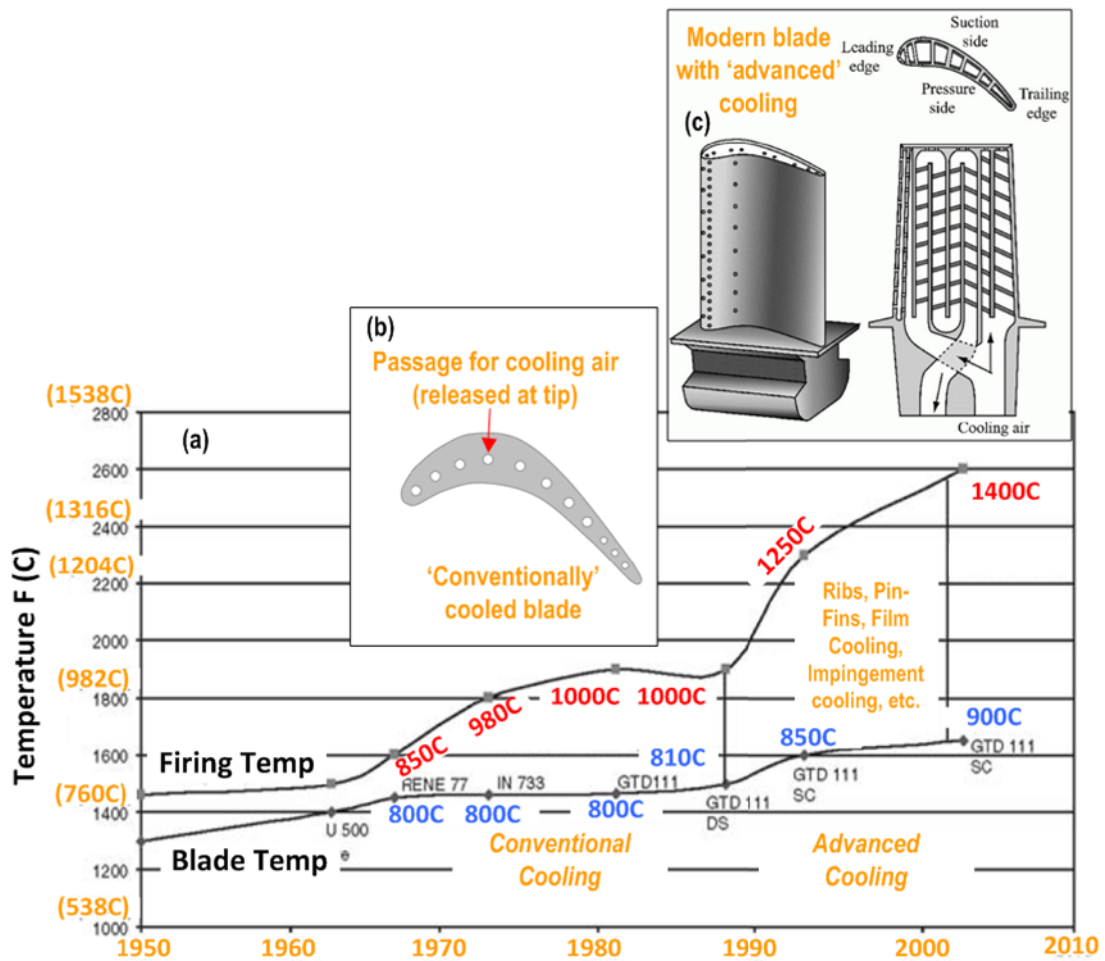
(a)Courtesy: Gas Turbine Handbook, Boyce, 2006 (b) Landis and Downs
(2009) (c) Thermal fluids engineering lab, Tokyo A&T University

Fig. 1. Trend of increasing turbine inlet temperature.
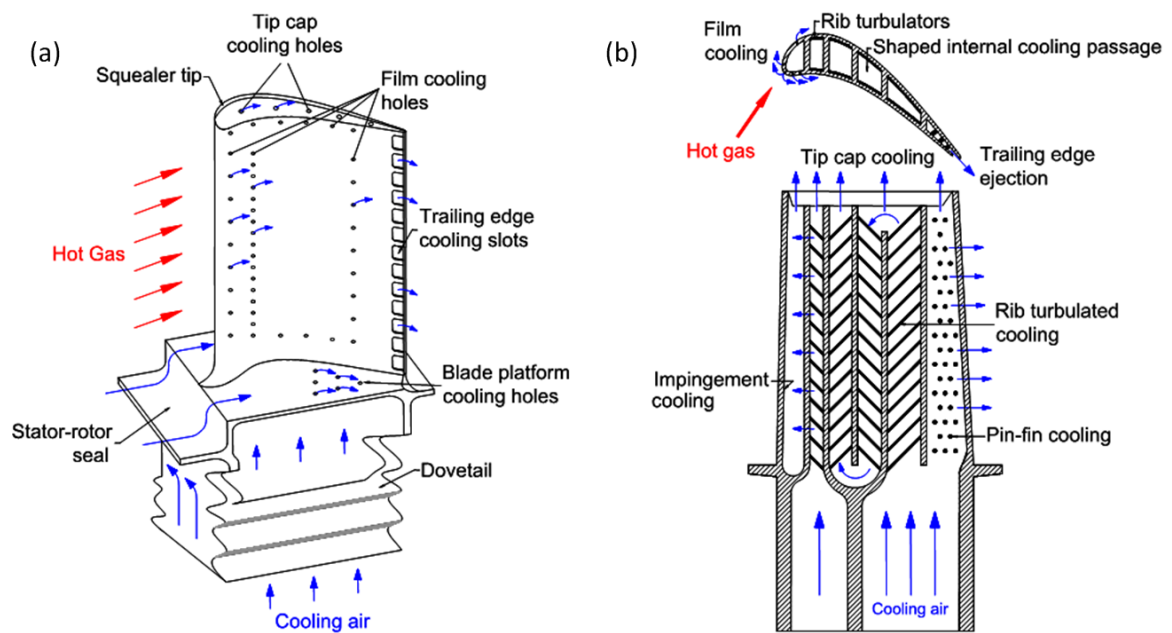
Fig. 2. (a)Film cooling on a gas turbine blade (b) Internal cooling of a gas turbine blade, showing passages with ribs and pin-fins.

CHAPTER II

ROUGHENED STATIONARY CHANNELS AT HIGH

REYNOLDS NUMBERS - EXPERIMENTAL STUDY*

Land based gas turbine engines have significantly larger blades - and therefore operate at much higher internal Reynolds numbers ($\sim$ 500,000). Correlations currently in literature have been developed for aviation gas turbine engines - whose Reynolds numbers are *an order of mangnitude* lower than land based gas turbine engines. Tests have been conducted to investigate whether the lower-range correlations are still valid at higher values of Re.

A. Literature Survey

Han et al. [4] conducted tests on channels with various aspect ratios using orthogonal low blockage ratio ribs (0.02<e/D<0.08) for spacing to height (p/e) ratios ranging from 10 to 20. It was concluded that, for the spacing values studied, taller ribs placed closer together (higher e/D and lower p/e) performed the best. Han and Park [5] and Park et al. [6] studied heat transfer with non-orthogonal ribs and concluded that the secondary flows induced by the ribs increase the heat transfer coefficient on the ribbed surface. They concluded that using ribs angled at 45deg - 60deg was the most beneficial from a thermal performance point of view. The effect of channel aspect ratio has been studied by Han et al. [5] and Park et al.[6].

_____

* Reprinted with permission from AP Rallabandi, H Yang and JC Han, Heat transfer and pressure drop correlations for square channels with 45 deg ribs at high Reynolds numbers, Journal of Heat Transfer 131 (2009) 071703; A. Rallabandi, N. Alkhamis and J.C. Han, Heat Transfer and Pressure Drop Measurements for a Square Channel with 45deg Round Edged Ribs at High Reynolds Numbers, Journal of Turbomachinery (2010) , In Press.

Though the ribbed side heat transfer augmentation is of the same order in all cases, the friction factor is much higher for channels with wider aspect ratios. Studies by Taslim et al.[7] have focused on cooling passages embedded in the leading edge of the blade. Zhang et al. [8] performed studies on a ribbed triangular channel. A flow visualization of the secondary flows is presented in [9], and a computational picture of secondary flows is painted in [10]. Su et al.[11] performed computations on a rotating channel with inclined ribs and presented predictions of secondary flows in the first channel. High blockage channels have been investigated by Taslim et al. [12] and more recently by Bailey et al. [13]. Taslim et al. found that friction factors increased with reduced rib spacing. Bailey et al. found that the Normalized Nusselt number Ratio (Nu/Nuo) was reduced by increasing the Reynolds number. They also found a monotonic dependence of Nu on e/D. Further derivatives of the inclined rib concept (crossed ribs, V-shaped ribs, inverted V shaped ribs[14, 15], broken parallel ribs, V-shaped broken ribs, delta and wedge shaped ribs [16], etc.) have been studied. V-shaped ribs are shown to enhance heat transfer over parallel ribs - at lower friction factors than comparable parallel ribs. The broken V-shaped ribs are found to enhance heat transfer further - at a comparable pressure drop. Studies have shown a deterioration in heat transfer enhancement due to the filleting - though compensated by a reduction in corresponding friction factor [13, 17, 18, 19]. This deterioration in heat transfer coefficient was found to be less at higher Re [18]. The reduction in friction factor was found to be larger at a higher e/D ratio [13, 17] - indicating that this effect could actually be beneficial. Dippery and Sabersky [20] detailed a method to analyze the pressure drop and heat transfer in a rough duct using non-dimensional parameters based on the turbulent boundary layer law-of-the-wall. Han et al. [5, 18, 21] adapted these parameters to rib-roughened channels. This correlation has been applied to various rib configurations (v-shaped, v-shaped broken

etc.) [15] and aspect ratios[6]. At lower Reynolds numbers in the ribbed channel, both the friction factor and average "fully developed" Nusselt number are found to be relatively low. The typical friction factor tends to attenuate to a constant value as the Reynolds number is increased.[12, 17] The Nusselt number shows a monotonically increasing trend with Reynolds number.

B. Objectives

The objective of this study is to measure heat transfer coefficients (Nu) and friction factors for a 45deg parallel rib roughened high blockage (0.094<e/D<0.188) square channel with spacing (p/e) ranging from 5-10. The Reynolds numbers tested are between 30,000 and 400,000 (with application to land based power turbines). The ribs tested have both sharp and rounded edges.

Current correlations in literature are valid only for aviation gas turbines ($Re <$ $100,000$, $e^+ < 1000$), which are much smaller in size than land-based gas turbines (Re$\sim$ $500,000$, $e^+ \sim 20,000$). The current study seeks to extend the aviation gas turbine correlations to be applicable to land-based gas turbines. These results will be of immense value to engine designers.

The objective of the second part of this study is to measure heat transfer coefficients (Nu) and friction factors for an identical 45deg parallel rib roughened high blockage. The ribs tested in this case have rounded edges and fillets, with radii equal to half the height.
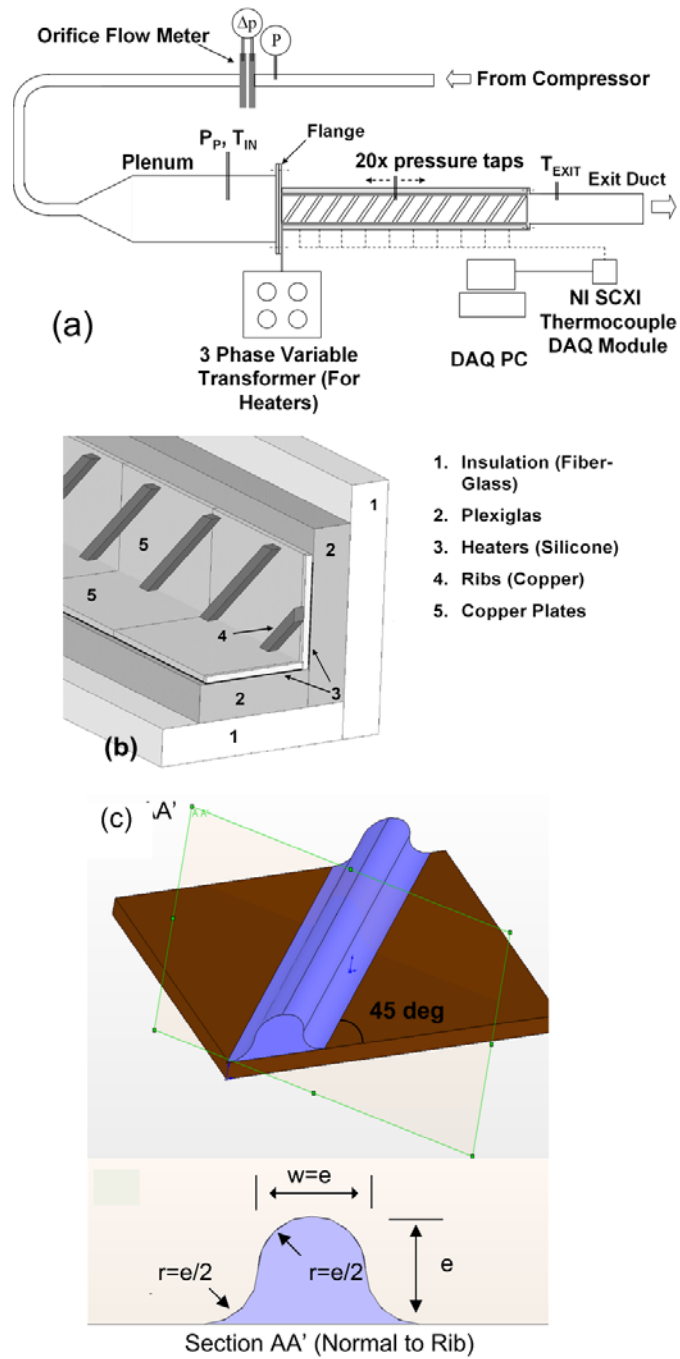
Fig. 3. (a)Test section schematic (b) Construction of test section, showing key features (c) Details of profiled ribs. Corresponding sharp edged ribs have square cross section.

C.   Experimental Details

1.   Test Setup

Air at high pressure is ducted in from 3 Ingersoll Rand Oil Free compressors operating at a pressure of 820kPa (120psi). This air enters the flow loop shown in Fig.3. The flow rate of air is metered using a 50.8mm (2") dia. orifice plate flow meter. This metering is performed by measuring pressures immediately upstream of the orifice plate and across the orifice plate (using digital and inclined Manometers, respectively). The air enters a plenum downstream of the orifice flow meter. The test section is placed immediately downstream of the plenum, such that the flow experiences a sudden contraction (8:1) before entering the instrumented test section. This contraction induces an aerodynamic and thermal "developing" region in the channel before a "fully developed" state is obtained. This is arbitrary to simulate the entrance geometry of blade internal cooling. The test section utilized is detailed in Fig.3. It has a square cross section of 101.6mm x 101.6mm (4" x 4"). Each of the 4 walls is sub-divided into 10 sequential stream-wise regions, comprised of 1 copper plate each. Regions are separated by rubber gaskets to inhibit thermal conduction. Angled (45°) ribs are attached in a non-staggered parallel pattern on the front and back surfaces only. The top and bottom surfaces are left smooth. Ribs used are made of copper and attached to the copper plates using a 0.05mm thick double sided tape (to ensure uniform thermal contact). They are reinforced on either side using small pieces of foil tape. Some ribs do cross over from one region to the next region - and might create a conductive path for heat to flow from one region to another. This effect is neglected in data reduction - as the effect is expected to be minor. Four silicone heaters (manufactured by Watlow Inc.) are glued to the back of each surface (top, front, bottom and back). The power input can be varied by controlling four separate single phase

transformers and measured by measuring the voltage applied to the heater by a digital multi-meter. Each plate is instrumented with T type copper-constantan thermocouples; the front (ribbed) and top (smooth) copper plates have 4 thermocouples each while the back (ribbed) and the bottom (smooth) plates have 1 thermocouple each. The thermocouples are buried inside a 0.4mm (1/64") dia hole drilled on the plate and held in place by using an epoxy resin. These thermocouples are connected to a National Instruments SCXI 1000 Chassis via the NI SCXI 1303 terminal block. The temperatures are measured using the NI Labview Program. Thermocouples in the plenum and in the exit duct are connected to a digital thermometer. Each of the 10 top plates has two pressure taps, located at 25% and 75% of its length. Static pressure is measured using either an inclined manometer or a digital manometer, depending on its value. The test section is installed in a 4cm (1.5") thick Plexiglas housing. Further insulation is provided (while running the heat transfer tests) by encapsulating the entire test section in a thick layer of fiber-glass. Fig. 3(b) shows a cross sectional illustration of the test section. An exit duct downstream of the instrumented channel is provided to ensure thermal and hydraulic fully developed conditions are retained as the flow exits the channel.

2.   Data Reduction

Using the mass flow rate measurements from the orifice flow meter, one can estimate the velocity in the channel (for the channel flow case). A Reynolds number for the channel is defined:

$$Re = \frac{V D_H}{\nu} \tag{2.1}$$

Silicone rubber heaters are used to generate heat that is dissipated within the test section. The resistance of each heater, $R\Omega$ is measured before each run, and is determined to be temperature-independent. The voltage, $VVolts$, supplied across each heater is measured by a multi-meter. The thermal power generated by the resistance heater is given by:

$$q = \frac{V^2}{R} \qquad (2.2)$$

Each heater is affixed to ten copper plates (regions 1-10). The heater provides constant heat flux along its length. Changing the voltage across the heater changes the steady state temperature measured on each copper plate. Since heat transfer coefficients vary from region to region, it is not possible to control the temperature recorded for each plate to a constant value. The voltages across the four heaters are actively controlled to ensure that the temperature difference between the ambient and the plates is around 30C.

An energy budget for each plate is performed to obtain the heat transfer coefficient.

$$h = \frac{q/A - q''_{loss}}{(T_w - T_B)} \qquad (2.3)$$

A, here is the area of the copper plate, and not does not include the area of the ribs. Reported Nusselt numbers are based on the projected area, so as to perform a fair comparison with one roughness element to another.

Here, q''_{loss} is the heat loss, which is determined based on a test. Heat loss occurs due to conduction through the test section to the air in the room. A low conductivity material is placed inside the test section inhibiting heat transfer within

the test section. The heaters are energized, with zero bulk flow. The voltage across the heaters is adjusted to control the steady state temperature. Two steady state temperatures are studied - one lower than the range encountered in the test, and one higher. Based on these two temperatures, a heat loss characteristic is obtained for each of the copper plates. The bulk mean temperature T_B in this case is interpolated from the value measured at the exit of the test section.

The Nusselt number for the current study is defined as:

$$Nu = \frac{hD_H}{k_{air}} \tag{2.4}$$

Static pressure taps are provided along the length of the channel, from which one can estimate the Fanning friction factor using the slope of the static pressure (Pa) vs x plot thus:

$$\bar{f} = \frac{D_H}{2\rho V^2} \left| \frac{dP}{dx} \right| \tag{2.5}$$

Thus determined friction factors are normalized by the Swamee-Jain approximation to the Colebrook correlation, corresponding to a smooth channel to quantify the friction factor penalty incurred by the roughened cases:

$$f_0 = \frac{0.331}{ln(\frac{5.74}{Re^{0.9}})^2} \tag{2.6}$$

The thermal performance defined (based on the projected area Nusselt number, Nu) as:

$$TP = \frac{Nu/Nu_0}{(\bar{f}/f_o)^{1/3}} \tag{2.7}$$

Based on the turbulent boundary layer Law-of-the-wall [4, 20, 22, 23], the fol-

lowing parameters have been defined. The Roughness Reynolds Number:

$$Re_k = e^+ = \frac{e}{D_H} Re(f/2)^{\frac{1}{2}} \tag{2.8}$$

The Friction Roughness Function:

$$R(e^+) = \left(\frac{2}{f}\right)^{0.5} + 2.5ln\left(\frac{4eW}{D(W+H)}\right) + 2.5 \tag{2.9}$$

The Heat Transfer Roughness Function:

$$G(e^+) = R + \frac{\frac{f}{2St} - 1}{\sqrt{\frac{f}{2}}} \tag{2.10}$$

A functional correlation between e^+, G and R has been used in literature to correlate the effect of rib-roughness on friction factor and heat transfer. A similar correlation is sought.

D.   Results and Discussion

1.   Sharp Edged Ribs

Heat transfer correlation. Fig 4 shows heat-transfer (Nusselt Number) results for the smooth case, normalized with the Dittus - Boelter correlation. (Nu/Nu0). This ratio exceeds 1 significantly at low values of x/D as would be expected of a developing turbulent flow in a pipe. At larger values of x/D, it is seen to attenuate to 1, validating the heat transfer measurements. The Nusselt Numbers in the "developed" region are averaged and plotted against Reynolds Number in Fig.5 - as a base-line for comparisons with ribbed heat-transfer results.

Figures 6,7 and 8 depict the variation of the Normalized Nusselt Number (Nu/Nu0) with x/D for various ribbed configurations. The shape of the curves is qualitatively similar to results reported by Han and Zhang for 45° ribs [15] - with a local maxima

(a)   (b)
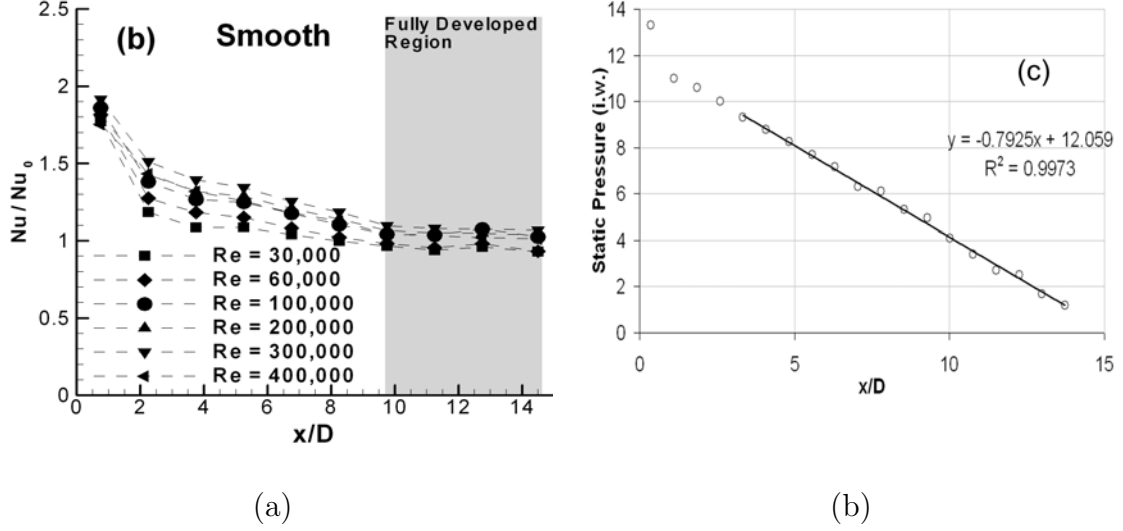
Fig. 4. (a) Normalized Nusselt number ratios for a smooth channel. Ratio approaches
1 in the highlighted "fully developed" region (b) Friction factor derived by
fitting straight line to measured static pressure profile for x/D > 4 for a ribbed
channel.

located at intermediate values of x/D. This local maxima is a signature of the sec-
ondary flow induced by inclined ribs. Ribs placed at 900 to the flow do not display
this behavior. Another trend evident from these figures is that the Nu/Nu_0 strictly
falls with increasing Re - which is also consistent with literature. [4]

Significant enhancements of the heat transfer coefficient on the smooth side are
also observed at high Reynolds numbers and at high values of e/D. This could be
attributed to the secondary flow traveling along the rib "impinging" onto the smooth
surface - and also to the high turbulence levels induced by the ribs. Figures 6,7 and
8 indicate that the enhancements on the smooth side are often comparable to those
on the rough side.

The rib spacing (p/e) also has a decreasing monotonic relationship with the Nus-
selt number (i.e. as the spacing between two consecutive ribs increases, the Nusselt
number decreases). This can be attributed to two reasons. Firstly, the heat trans-
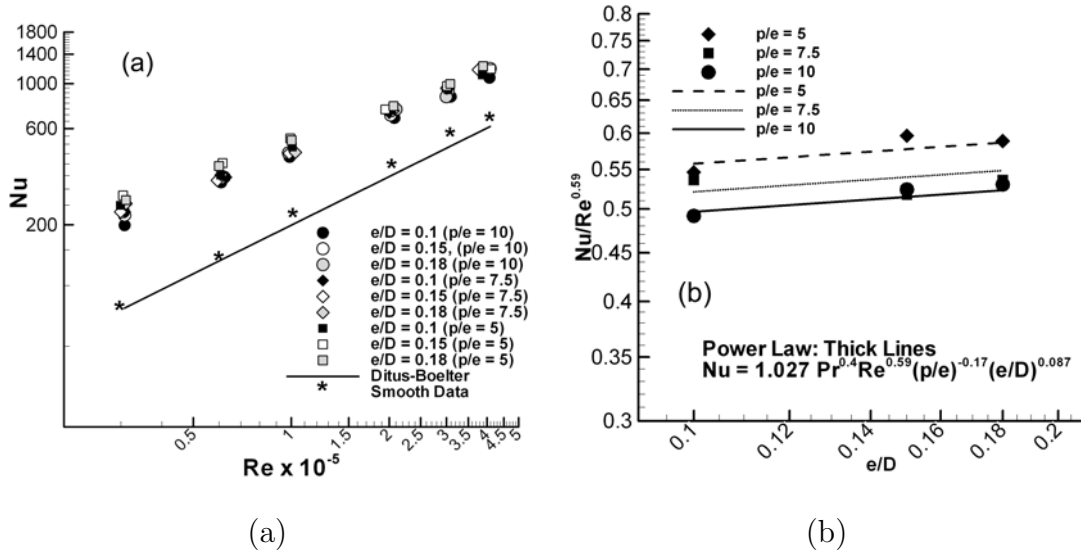
Fig. 5. (a) Fully developed ribbed side average Nusselt numbers obtained in various test cases (b) Correlation for average Nu as a function of Re, rib height (e/D) and spacing (p/e).
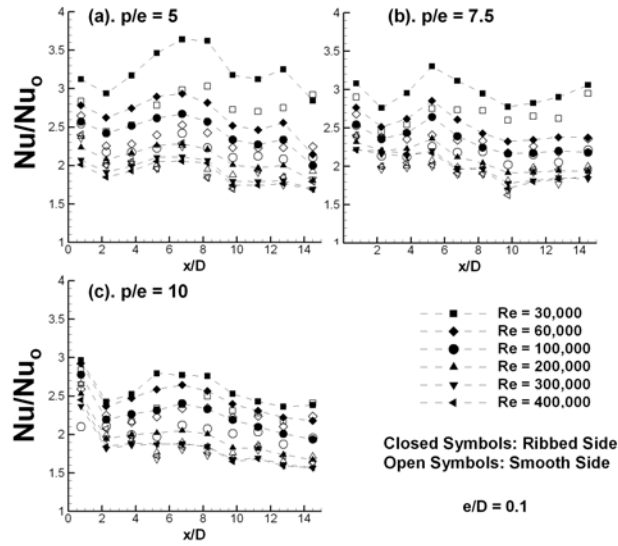
Fig. 6. Nusselt number ratios plotted along the channel for e/D = 0.1: (a) p/e=5, (b) p/e = 7.5 (c) p/e = 10.
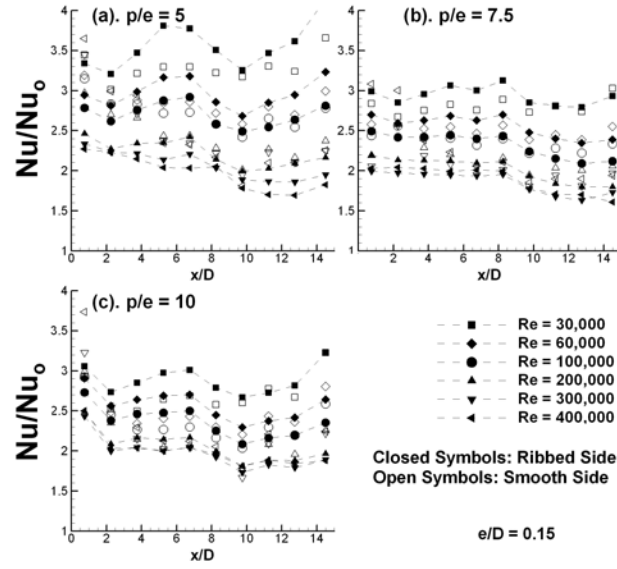
Fig. 7. Nusselt number ratios plotted along the channel for e/D = 0.15: (a) p/e=5, (b) p/e = 7.5 (c) p/e = 10.
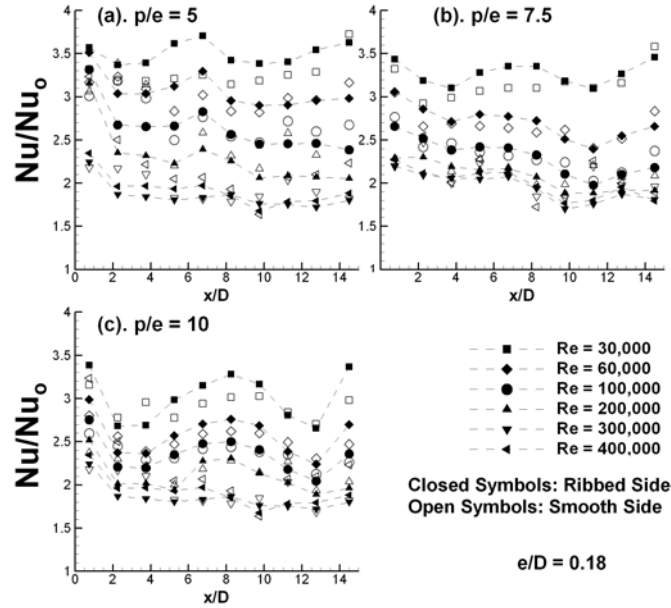
Fig. 8. Nusselt number ratios plotted along the channel for e/D = 0.18: (a) p/e=5, (b) p/e = 7.5 (c) p/e = 10.
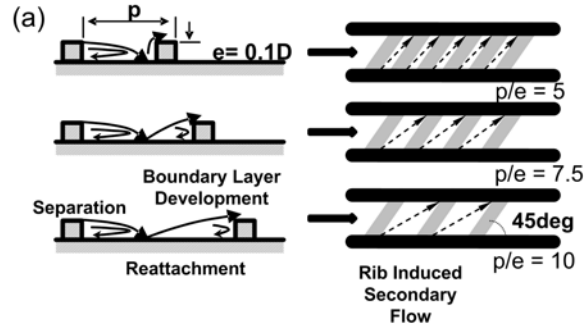
(a) Effect of rib spacing for constant rib height
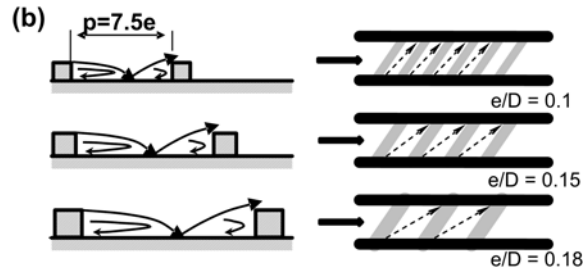
(b) Effect of rib height (for constant p/e)

Fig. 9. Schematic of flow over inclined ribs.

fer interface area between the flow and the test section increases as ribs (which are thermally active, since they are made of copper) are placed more densely within the channel. This would result in a higher heat transfer coefficient based on projected area for the same heat transfer coefficient based on total area. Secondly, a larger number of ribs (smaller p/e) could induce greater secondary flow - and greater turbulence. This effect is schematically explained in Fig.9(a) which compares three separate p/e ratios for a single e/D (0.1). The size of the recirculation zone downstream of the rib in each case remains the same, as does the reattachment (high heat transfer) zone. The boundary layer then starts to develop (reducing local heat transfer as it becomes thicker) until it is tripped by the next rib. This further reduces the heat transfer coefficient for larger values of p/e (as there is more distance between two consecutive

Table I. Total to projected area ratios A_t/A_s for different rib configurations.

	p/e=5	p/e=7.5	p/e=10
Sharp Edged Ribs	1.57	1.37	1.28
Round Edged Ribs	1.32	1.22	1.16

ribs). The combined effect is evident in Figs. 5, 6, 7 and 8.

The rib height has an increasing monotonic relationship with Nusselt Number. This effect can be attributed to the obstruction to the flow, which enhances the secondary flow - and therefore heat transfer, as is demonstrated by Figs. 5, 6, 7 and 8. The recirculation zone, the reattachement zone and the developing boundary layer region all increase in size as e increases (Fig. 9). Heat transfer increases significantly in the separation and reattachment zones due to the increased rib height. This results in an overall increase in heat transfer. An increase in rib height does not result in an increase in total area available for heat transfer for a given p/e, as is demonstrated in Table I.

For the range of parameters (p/e and e/D) studied, Fig. 5 indicates that the ribbed-side averaged Nu values, when plotted on a log-log scale against Re all seem to be linear (with the same slope). This indicates that the relationship between Nu and Re is amenable to correlation by a power law with a parameter independent exponent. A correlation is developed by computing a least squares best fit for the parameter range studied in the experiment.

$$Nu = 1.027 Pr^{0.4} Re^{0.59} \left(\frac{p}{e}\right)^{-0.17} \left(\frac{e}{D}\right)^{0.09} \tag{2.11}$$

$$30,000 < Re < 400,000; 5 < \frac{p}{e} < 10; 0.1 < \frac{e}{D} < 0.2$$

This correlation has a maximum deviation of 7%.

Friction factor correlation. Increasing the number of ribs and height of the ribs (decreasing p/e and increasing e/D) has a beneficial impact on the heat transfer coefficient by tripping the flow, increasing turbulence and inducing secondary swirls. This increase comes at a price: higher friction losses. A designer, therefore needs friction data to complement heat transfer data. Friction factors in a smooth pipe are due to skin-friction only, and have a tendency to reduce with Re [24]. However, when ribs are introduced, the regime shifts from a purely skin friction case to a case dominated by form-drag due to the ribs. The flow encounters obstructions (ribs) and forms separation zones immediately downstream of the ribs, which induces drag on the test section, and therefore a pressure drop in the flow. Ribs also trip the boundary layer - necessitating the development of a new boundary layer after the flow reattaches. This results in thinner boundary layers between the ribs and therefore, higher friction factors.

There is consensus in literature that the friction factor for a ribbed channel remains largely independent of Re, beyond a certain Re. The measurements (Fig. 10 indicate that there is no dependence of on Re. However, $\bar{f}$ /f_o increases with Re, since f_o falls with Re. Clearly, the greater the obstruction (larger e/D) or larger the number of ribs (lower p/e), the greater the disturbance to the flow, and the greater is the friction factor. This is seen in Figs. 10(a) and (b). This relationship is summarized by the correlation:

$$\bar{f} = 2.46 \left(\frac{p}{e}\right)^{-0.62} \left(\frac{e}{D}\right)^{1.23} \tag{2.12}$$
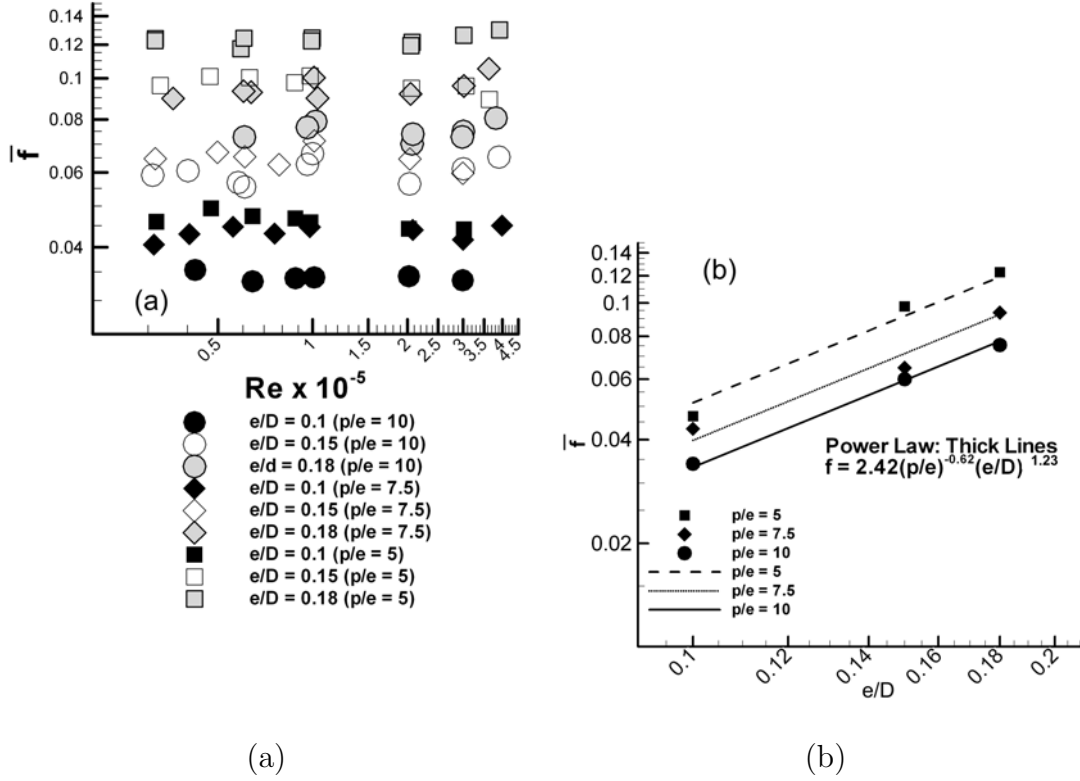
Fig. 10. Friction factors for various test cases (b) Correlation for friction factor as a function of e/D and p/e.

$$30,000 < Re < 400,000; 5 < \frac{p}{e} < 10; 0.1 < \frac{e}{D} < 0.2$$

This correlation has a maximum deviation of 8%. Figure 11 shows comparisons with earlier studies for p/e = 10. At low values of e/D (old tests), the exponent of the vs e/D correlation seems a lot lower than at higher values of e/D. This could be because of increased form drag owing to increased blockage by the ribs.

Thermal performance. Figure 12(a) compares the ribbed-side-average heat transfer enhancement (Nu/Nu0) on the ordinate with $(\bar{f}/f_o)$ on the abscissa. This graph shows the deterioration in performance (decreasing Nu/Nu_o and increasing in $\bar{f}/f_o$) as Re increases. The thermal performance, F, is proportional to the heat transfer
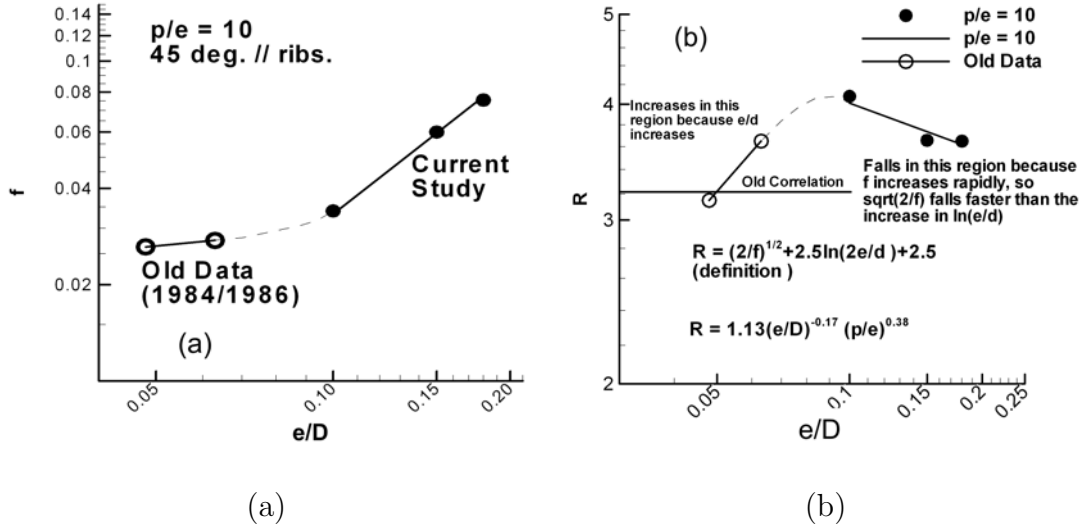
Fig. 11. (a) Comparison of current friction factor with raw data from Han et al. [25, 26] (b) Comparison of current friction roughness (R) with correlation published earlier.

enhancement (Nu/Nu_o) and inversely related the friction factor ratio, $\bar{f}/f_o$. Since Nu/Nu_o, for a given configuration tends to fall with increasing Re and $\bar{f}/f_o$ tends to increase with increasing Re, F decreases with increasing Re. The measured dependence of F on Re is shown in Fig. 12(b). The shortest rib (e/D = 0.1) case has the best thermal performance, whereas the e/D = 0.18 case has the worst performance. This can also be appreciated from Fig. 12(a), which shows that by increasing e/D from 0.1 to 0.18, one increases Nu only by 30%, whereas one increases the corresponding friction factor by 400%! The thermal performance exceeds unity only when Re < 100,000, indicating possible issues with economic viability at higher values of Re. However, when the application demands the removal of a large amount of heat, the turbine designer must be prepared for a disproportionately large pressure drop penalty - as lower Reynolds Numbers would result in lower Nusselt numbers (in absolute value) - and would not satisfy the purpose of removing a large amount of heat.
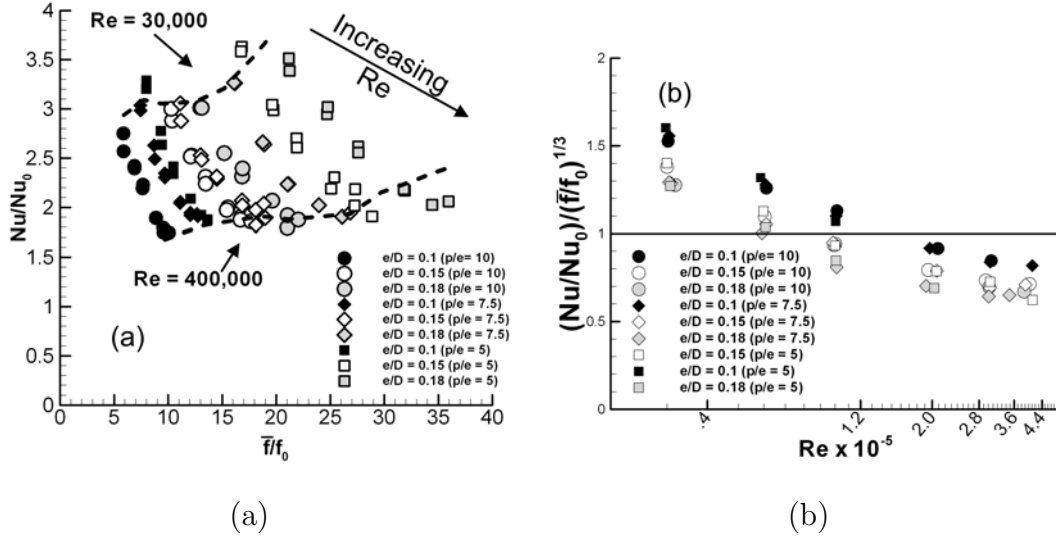
Fig. 12. (a) Ribbed side average Nusselt number enhancement ratio (compared to a smooth channel) plotted against friction factor penalty ratio for all cases (b) Thermal performance for all experimental cases. performance is below 1 for most cases with Reynolds number exceeding 100,000, indicating a significant pressure loss penalty.

Generalized correlation. The parameters G and R (heat transfer and friction roughness, respectively) have been used in literature to absorb the effect of rib-height (e/D) and Reynolds number (Re) into one variable. G and R have been correlated with e+ (a non-dimensional roughness Reynolds Number) and p/e. Expressions of the form $R = C_1(p/e)^m$ and $G = C_2(p/e)^m(e^+)^n$ have been utilized to accurately correlate experimental data. But in our case, Fig.9a indicates a change in slope (in the log-log plot) in vs e/D. Since $\bar{f}$ starts increasing at a much higher rate, corresponding values of R start falling faster as can be seen in Fig. 11. Therefore, variations in e/D will have to be factored in explicitly in the correlation, as shown in Fig. 13(a). The Heat transfer roughness (G), on the other hand, does not vary much with e/D or p/e. (Figs.14(b) and 13(b)). The following correlations are proposed (extending work done by Han et al., 1988):
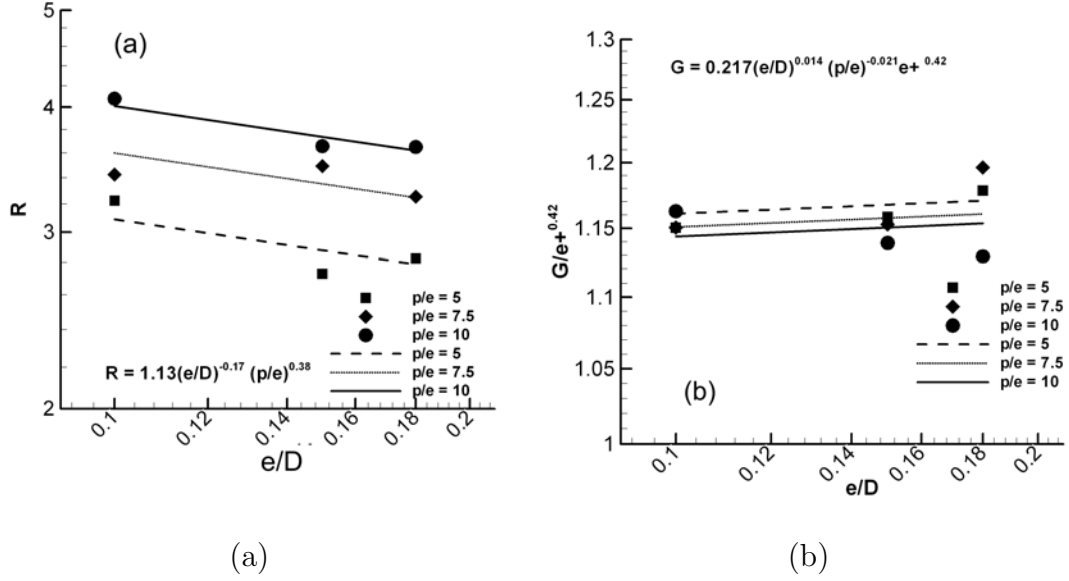
Fig. 13. Correlations for R and G as a function of e/D and p/e.

$$R = 1.13 \left(\frac{e}{D}\right)^{-0.17} \left(\frac{p}{e}\right)^{0.38} \tag{2.13}$$

$$G = 1.24 \left(\frac{e}{D}\right)^{0.014} \left(\frac{p}{e}\right)^{-0.02} (e^+)^{0.42} \tag{2.14}$$

Figures (14(a) and (b)) indicate that the correlations for R and G do not agree with the earlier published correlations. This discrepancy can be attributed to the vastly disjoint nature of the parameter space considered - the older study [4] considers 0.048<e/D<0.078 and 10 < p/e < 20, and Re < 70000; whereas the current study's parameter range is different. The current study explores a range of e/D which is considerably larger than in [4]. The turbulent boundary layer universal logarithmic velocity profile assumption is valid when the surface roughness is relatively small. Larger rib thickness could invalidate this assumption owing to greater form drag caused by flow separating and re-attaching due to the rib in comparison of with the skin friction. This causes a dependence of R and G on e/D as well as on e+. In
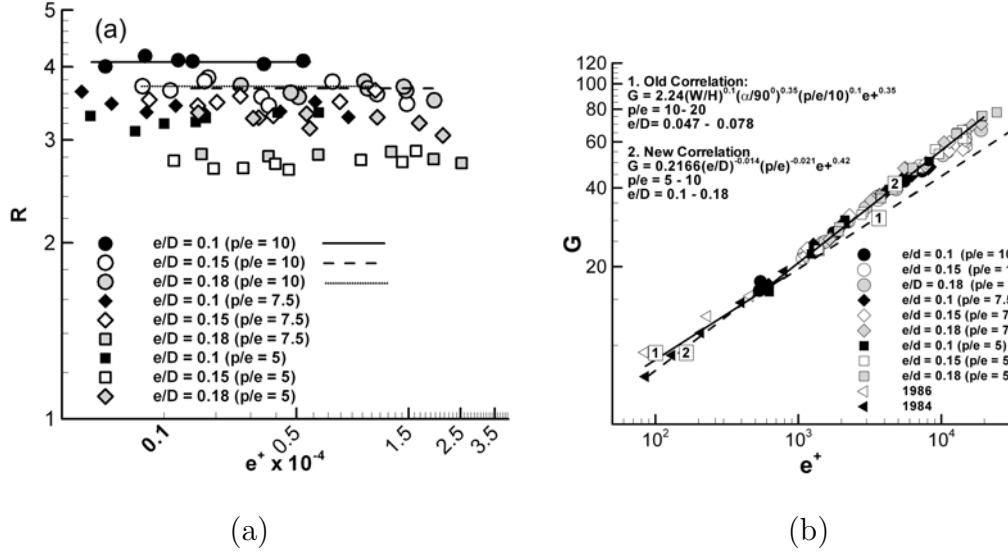
Fig. 14. (a) Variation of friction roughness (R) with roughness Reynolds number (e+)
(b) Heat transfer roughness parameter G from current study plotted against
roughness Reynolds number e+, compared with data from Han et al. [25, 26].

addition, the current study focuses entirely on 45° parallel ribs in a square channel;
the older studies also consider channels with various aspect ratios and various rib
angles. And also, the data in literature [4, 21] has been obtained using center-line
thermocouples embedded on a foil heater; current data has been obtained using copper
plates to regionally average heat transfer coefficients.

Error analysis. The Kline-McClintock [27] scheme has been used to estimate the
experimental uncertainty. The maximum experimental uncertainty in measuring the
Reynolds Number is estimated to 3%; the maximum experimental uncertainty in
Nusselt number (which corresponds with the lowest temperature difference between
the plate and the bulk-mean temperature) is estimated to be 5%. The uncertainty of
the friction factor is estimated to be 7%.
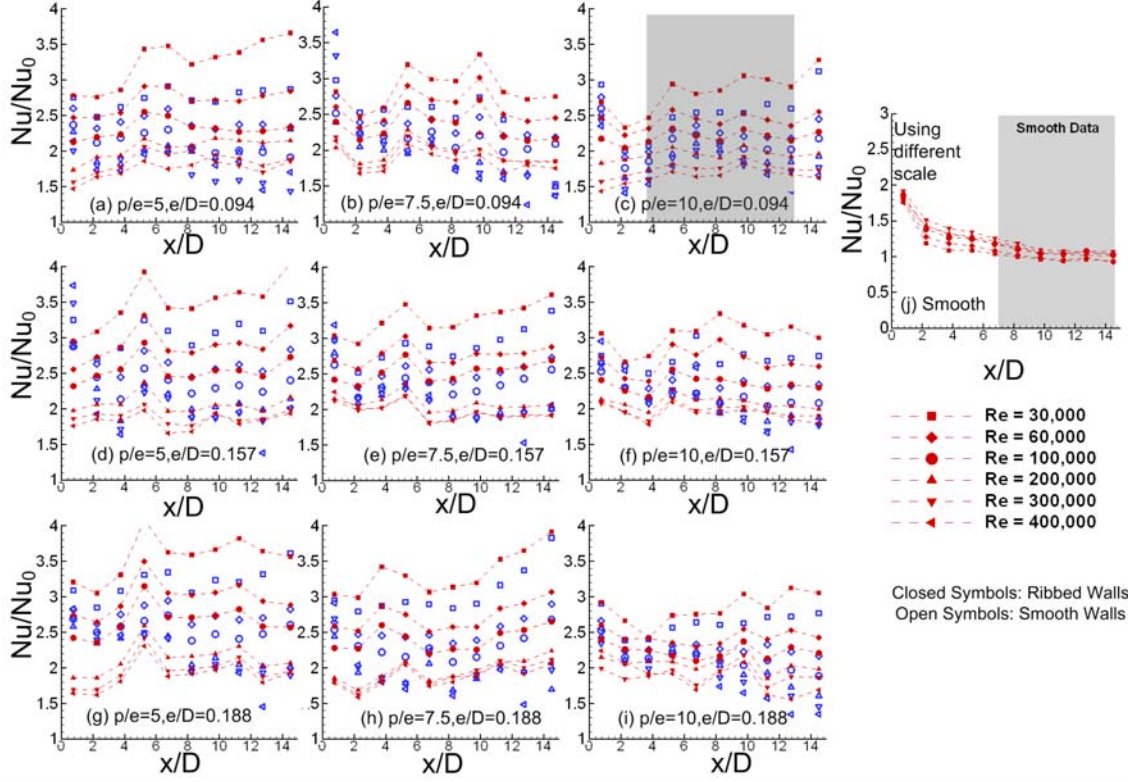
Fig. 15. Measured Nusselt number enhancement ratios for various (indicated) spacing and height values. For the smooth case (i) Nusselt number ratios attenuate to unity with increasing x/D. Shaded regions in (c) and (j) indicate regions considered to compute average Nusselt numbers (Nu_R).

2.   Round Edged Ribs

Heat transfer enhancements. The normalized Nusselt Number (Nu/Nu0) is plotted with x/D in Fig. 15 for various tested configurations. The closed (red) symbols represent the ribbed surface heat transfer enhancement; the open (blue) symbols represent the smooth surface enhancement. Lower Re values demonstrate a larger enhancement than higher Re values - a trend documented extensively in literature. Qualitatively, these curves agree with observations by Han et al. [15] - inclined ribs do introduce a local maxima at intermediate values of x/D (a behavior not encountered
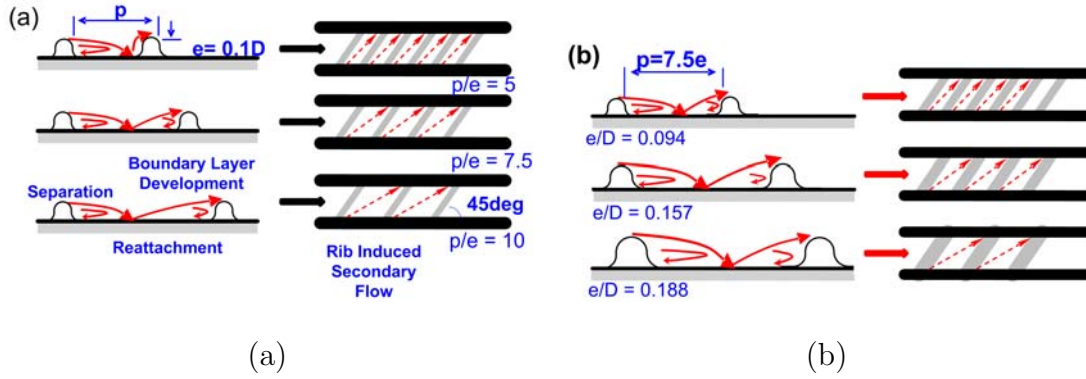
Fig. 16. (a) Effect of rib spacing on flow field (b) Effect of rib height on flow field.

with ribs perpendicular to the flow). Figure 15 indicates that the heat transfer coefficient on the smooth side is also enhanced significantly at higher Re. At higher Re, the enhancements are comparable to those on the ribbed surfaces. This is possibly due to the secondary flow traveling along the rib impinging on the smooth surface - and the high turbulence induced in the flow by the ribs. For the range of spacing ratios (p/e) studied, a decreasing relationship of Nu with p/e is observed. When the spacing is sparse, the heat transfer coefficient reported is low. This is explained in Fig.16. As the spacing between 2 consecutive ribs increases, the boundary layer (which separates on the tip of each rib) reattaches in the region between two ribs and starts developing. The larger the value of p, (the distance between two consecutive ribs), the thicker the boundary layer is when it separates - and the lower the heat transfer. In closely spaced ribs (smaller p/e), frequent tripping ensures that the boundary layer stays thin - and therefore heat transfer coefficients are maintained at a high value. Additionally, the secondary swirls developed due to a large number of inclined ribs also increase the turbulence - therefore further increasing the heat transfer The rib spacing effect can be observed by comparing Figs 15(a), (b) and (c); (d) (e) (f) and (g),(h) and (i). These figures (along with Figs. 17 and 18) clearly
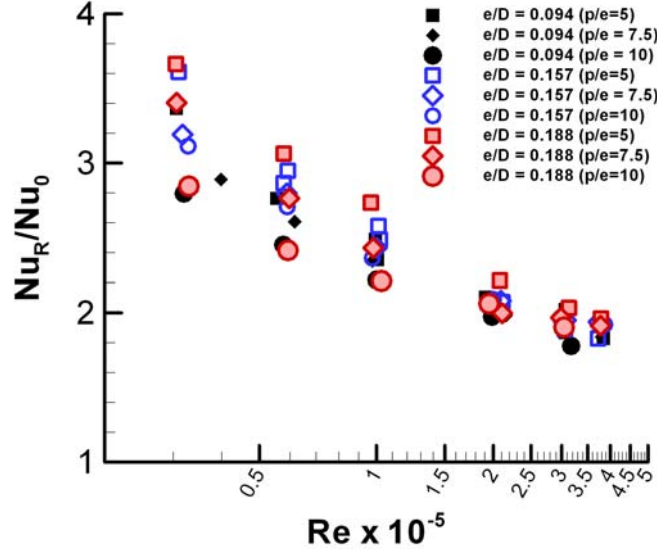
Fig. 17. Variation of averaged Nu/Nuo with Re for various cases.

show the improvement of heat transfer due to reducing the rib spacing. Also, as the spacing between 2 ribs increases, the interface area between the test section and the air increases. This increase in available area for heat transfer adds to the improvement in heat transfer (based on projected area). Figure 19 indicates that when the Nusselt number is based total area (defined as the sum of inter-rib smooth area and the exposed rib area) rather than just the projected area, the rib-spacing does not have an effect on the reported Nusselt number. This indicates that, for the spacing ratios studied, additional enhancement in heat transfer by reducing rib spacing is dominated by the interface area increase due to using a larger number of ribs. The rib height has a less pronounced effect on heat transfer. A larger value of e/D (for the same p/e) does not imply a larger total-to-projected area ratio, since an increase in e also means an increase in p to keep p/e constant. Taller ribs induce stronger secondary flows - and this secondary flow induces more turbulence - and therefore, more
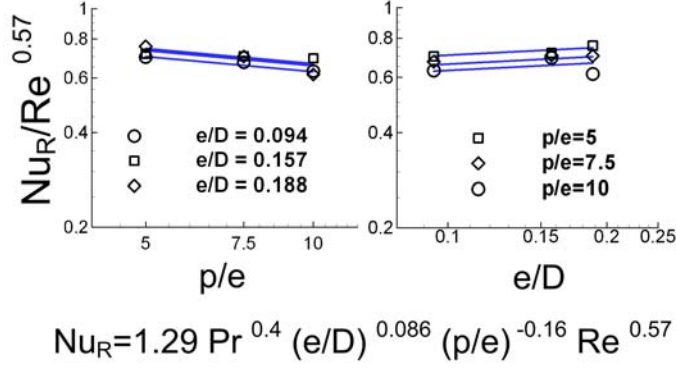
Fig. 18. Proposed Nu power law correlation for round edged ribs (for range 0.095<e/D < 0.19 and 5 < p/e < 10).

heat transfer. However, this effect is negated by the boundary-layer configuration detailed in Fig. 16. A taller rib (for the same p/e) implies a larger spacing (p) between two consecutive ribs. The flow, after separating on the tip of the rib, reattaches in between two consecutive ribs, and a boundary layer starts developing. The larger spacing between two tall ribs implies a thicker boundary layer and consequently, a lower heat transfer coefficient. This negates the beneficial effect of the turbulence induced by the stronger secondary flow. The rib-height effect can be appreciated by comparing Figs 15(a),(d) and 4(g); (b),(e) and (h); (c),(f) and (i).

Friction factors. Friction factors in a smooth pipe are due to skin-friction only, and have a tendency to reduce with Re [24]. Measured friction factors (Fig. 20(b) deviate from the smooth correlation by at most 45% (at high Reynolds numbers). Based on the work of Moody et al. [24], this corresponds to a surface roughness of 0.05mm - which could be due to unevenness of the insulation between two copper plates. However, when ribs are introduced, the regime shifts from a purely skin friction case to a case dominated by form-drag due to the ribs. The flow encounters obstructions (ribs) and forms separation zones immediately downstream of the ribs, which induces
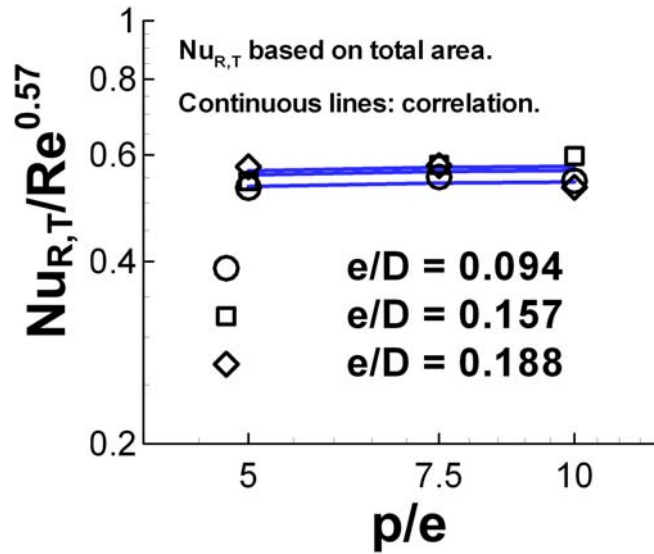
Fig. 19. Effect of rib spacing on Nusselt numbers based on total area (including ribbed and smooth surface areas).

drag on the test section, and therefore a pressure drop in the flow. Ribs also trip the boundary layer - necessitating the development of a new boundary layer after the flow reattaches. This results in thinner boundary layers between the ribs and therefore, higher friction factors. Clearly, when ribs are spaced more closely to each other, the thinner boundary layers (Fig. 16) and the additional form drag due to having more separation zones increase the pressure drop. Reducing the rib spacing (reducing p/e at the same e/D) increases friction factor - and this can be seen in Figs. 20 and 21. Taller ribs (larger e/D at the same p/e) introduce larger separation zones (Fig. 16(b)) - and the additional form drag far outweighs the skin-friction benefit of having thicker boundary layers between two ribs. The measured friction factors indicate that the rib height effect is much stronger than the rib spacing effect. (Fig. 20)
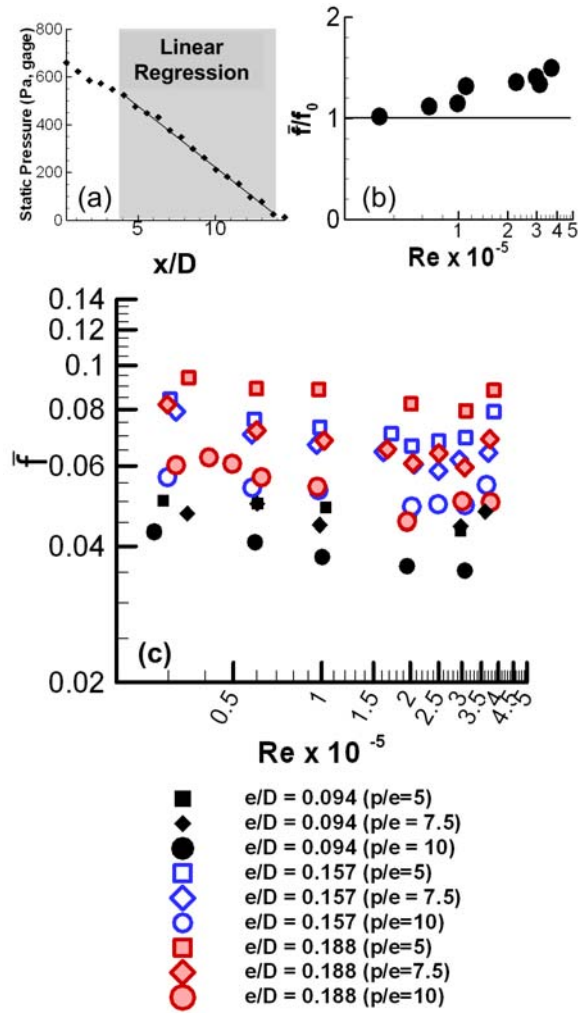
Fig. 20. (a) Linear regression used to determine friction factor (b) Measured smooth friction factor compared with standard correlation (c) Variation of friction factor with Re for various rough cases.

$$\bar{f} = 1.42(e/D)^{0.73}\,(p/e)^{-0.49}\,Re^{-0.07}$$
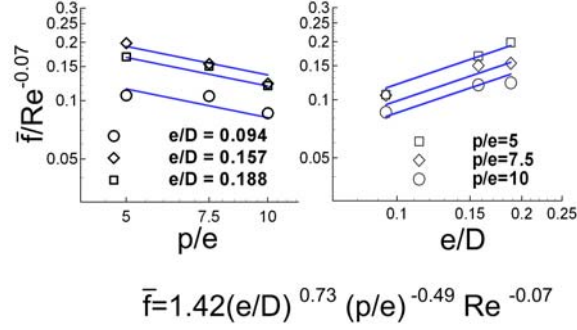
Fig. 21. Proposed friction factor power law correlation for round edged ribs (range : 0.095<e/D < 0.19 and 5 < p/e < 10).

Heat transfer and friction factor correlations. As seen in Fig. 18, measured Nusselt Numbers for this current work can be correlated by:

$$Nu = 1.29 Pr^{0.4} Re^{0.57} \left(\frac{p}{e}\right)^{-0.16} \left(\frac{e}{D}\right)^{0.086} \tag{2.15}$$

$$30,000 < Re < 400,000; 5 < \frac{p}{e} < 10; 0.1 < \frac{e}{D} < 0.2$$

The correlation for sharp edged ribs (for the same parameter range) presented by earlier in this chapter is:

$$Nu = 1.027 Pr^{0.4} Re^{0.59} \left(\frac{p}{e}\right)^{-0.17} \left(\frac{e}{D}\right)^{0.09} \tag{2.16}$$

The similarity of constants and exponents in Eqs. 2.15 and 2.16 indicates that using round edged ribs instead of sharp edged ribs has little or no effect of measured heat transfer coefficients. This is verified by applying the sharp edged correlation to the round edged data in Fig. 22(a). Regressing the round-edged rib friction factor measurements, the following power law correlation is obtained (with a RMS deviation of 8%):
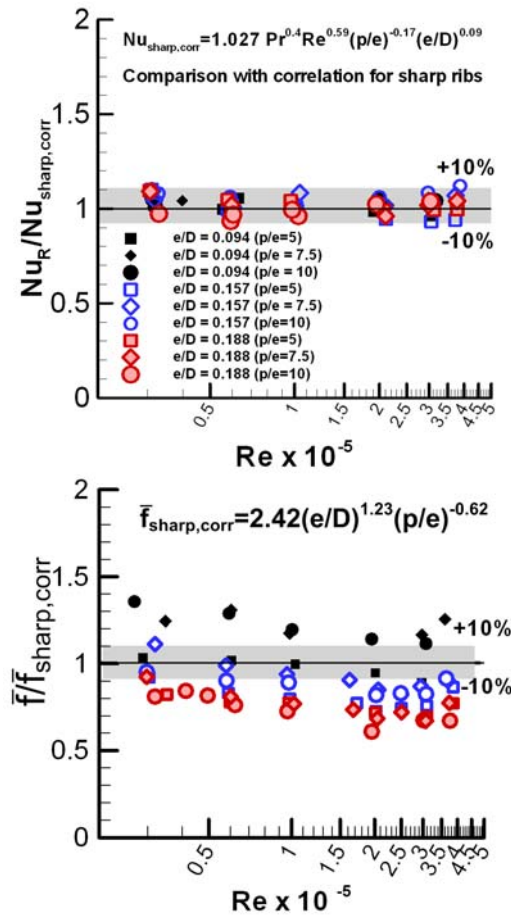
Fig. 22. (a) Comparison of measured round edged rib Nusselt numbers with values predicted for identical sharp edged ribs. (b) Comparison of measured friction factors for round edged ribs with correlation for sharp edged ribs.

$$\bar{f} = 1.42 \left(\frac{p}{e}\right)^{-0.49} \left(\frac{e}{D}\right)^{0.73} Re^{-0.07} \tag{2.17}$$

$$30,000 < Re < 400,000; 5 < \frac{p}{e} < 10; 0.1 < \frac{e}{D} < 0.2$$

A correlation for friction factors incurred by sharp edged ribs is presented earlier in this chapter (with a RMS deviation of 5%):

$$\bar{f} = 2.46 \left(\frac{p}{e}\right)^{-0.62} \left(\frac{e}{D}\right)^{1.23} \tag{2.18}$$

Since the correlation for Nusselt number developed earlier (Eq. 2.16), seems satisfactorily applicable to the round-edged rib data, a natural question arises: Can round-edged rib friction factor also be predicted using the sharp-edged rib correlation? Figure 22(b) answers that question in the negative. For most cases, friction factor is over-predicted by Eq. 2.18. This implies that friction factors for ribs with rounded edges are lower than corresponding sharp-edged cases - a trend in agreement with literature [14, 17]. Friction factor values for the e/D = 0.094 and p/e = 10 are an exception - the correlation seems to under-predict these values - indicating an increase friction factor for the smallest rib-height considered.

Figure 23 compares expected flow fields around sharp edged ribs and round edged ribs. In sharp cornered ribs, flow separation is expected to occur on the tip (as indicated in Fig 16) - increasing heat transfer and friction loss. This separation is avoided in the round-edged ribs - reducing local heat transfer and pressure loss. The recirculation zones formed at the base of the ribs are expected to be much smaller for the round edged cases - increasing local heat transfer and reducing local pressure loss. It is expected that the cumulative effect results in a lower friction factor (compared to sharp-edged ribs) for round-edged ribs - and a similar heat transfer coefficient. The
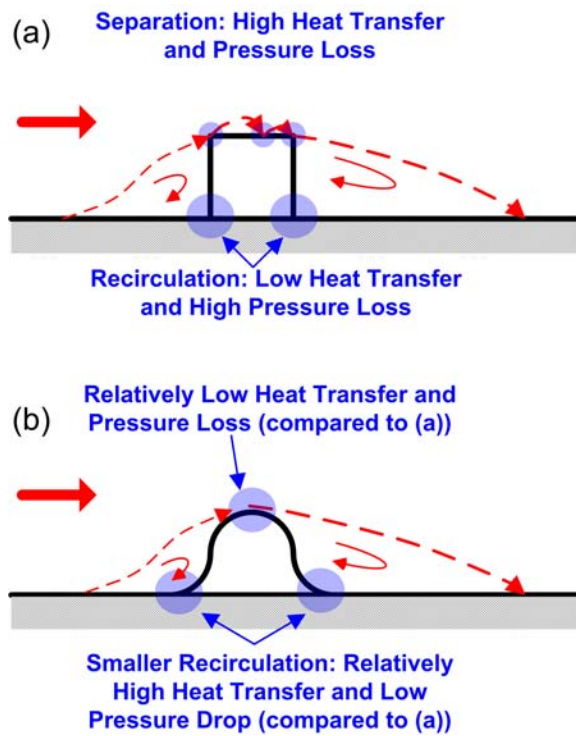
Fig. 23. Speculative flow-field comparisons around sharp and rounded edge ribs indicating regions with high and low heat transfer and pressure losses.
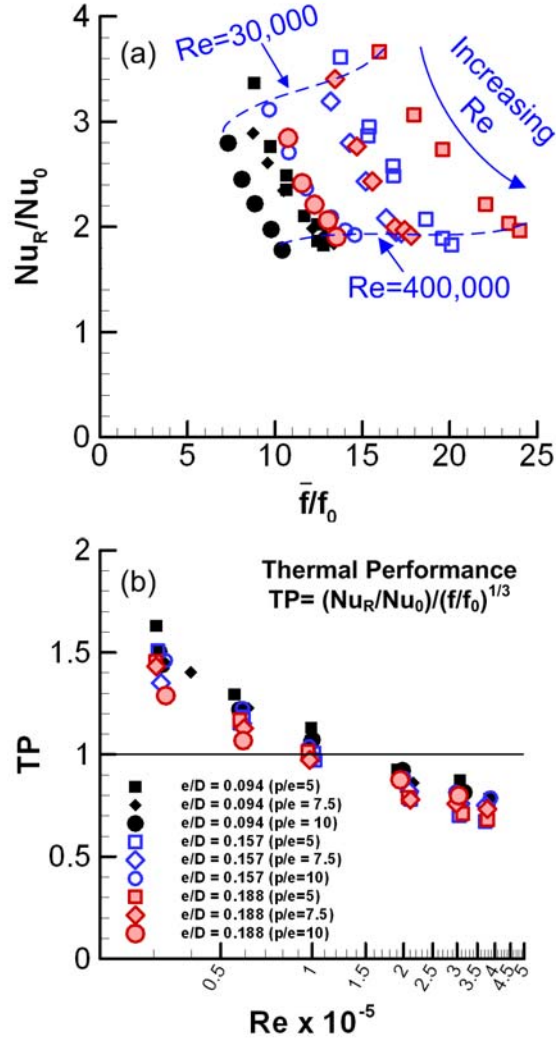
Fig. 24. ((a) Heat transfer enhancement plotted against friction factor penalty (as compared with smooth channel) for various cases (b) Measured Thermal Performance (TP) plotted as a function of Reynolds number. Higher Reynolds numbers offer lower thermal performance.

fillet radii chosen for this study are arbitrary. Reducing the fillet radius will almost certainly increase the friction factor, approaching the sharp edged case. The above correlations might not seem of general value - since they consider only one specific fillet radius (r=e/2). However, since the fillet radius considered is drastic (half the height of the rib), this study gives a lower bound for the friction factor. This study also verifies that the heat transfer coefficient does not suffer any deleterious effects due to using profiled ribs instead of sharp edged ribs for the parameter range in consideration.

Thermal performance. Figure 24(a) compares the ribbed-side-average heat transfer enhancement (Nu/Nu_o) on the ordinate with $(\bar{f}/f_o)$ on the abscissa. This graph shows the deterioration in performance (decreasing Nu/Nu_o and increasing $\bar{f}/f_o$) as Re increases. The thermal performance, TP, is proportional to the heat transfer enhancement (Nu/Nu_o) and inversely related the friction factor ratio, $\bar{f}/f_o$. Since Nu/Nu_o, for a given configuration tends to fall with increasing Re and $\bar{f}/f_o$ tends to increase with increasing Re, TP decreases with increasing Re. The measured dependence of TP on Re is shown in Fig. 24(b) The shortest rib (e/D = 0.094) case has the best thermal performance, whereas the e/D = 0.188 case has the worst performance. The thermal performance exceeds unity only when Re < 100,000, indicating possible issues with economic viability at higher values of Re. However, when the application demands the removal of a large amount of heat, the turbine designer must be prepared for a disproportionately large pressure drop penalty - as lower Reynolds numbers would result in lower Nusselt numbers (in absolute value) - and would not satisfy the purpose of removing a large amount of heat. Friction factors, in absolute value are significantly lower (especially at high e/D and Re values) for round edged ribs in comparison with sharp edged ribs. This results in a slightly higher thermal performance for round-edged ribs.
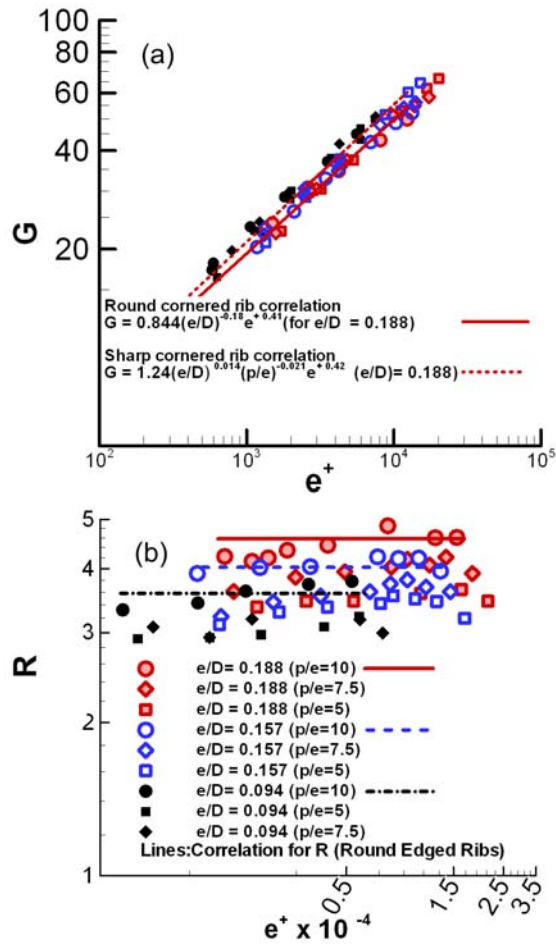
Fig. 25. Measured heat transfer roughness parameter (G) plotted against roughness Reynolds number (e+). Indicated correlations refer to the e/D = 0.188 case. Sharp edged rib correlation does not agree with round edged rib data (b) Measured friction roughness parameter (R) plotted against roughness Reynolds number (e+).
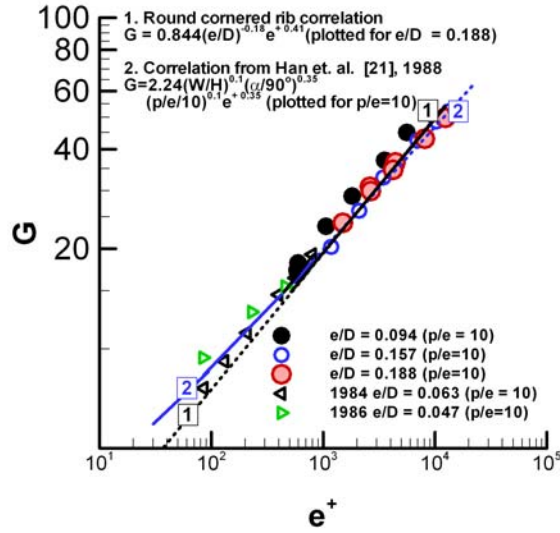
Fig. 26. Heat transfer roughness parameters determined in current work benchmarked against sharp-rib results presented by Han et al. (1984), [25] and Han et al. (1986), [26].

Generalized correlation. The parameters G and R are used in literature to generalize the experimental correlations for possible use in channels with varying aspect ratios. Correlations were presented for sharp edged ribs and compared with older data in the earlier section of this chapter. The current round-edged rib data can be regressed into the following power law correlations:

$$R = 3.34 \left(\frac{e}{D}\right)^{0.25} \left(\frac{p}{e}\right)^{0.29} \tag{2.19}$$

$$G = 0.844 \left(\frac{e}{D}\right)^{-0.18} (e^+)^{0.41} \tag{2.20}$$

for the range,

$0.095 < e/D < 0.188$, $5 < p/e < 10$ and $500 < e^+ < 18000$

Figure 25 indicates that the correlation for sharp ribs over-predicts the heat
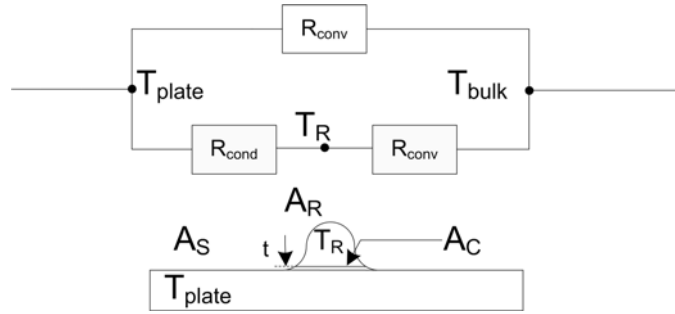
Fig. 27. One dimensional resistance model for the plate-rib system indicating convective and contact resistances.

transfer roughness value. Even though the actual Nusselt number is not affected by using round edged ribs, the heat transfer roughness is found to reduce. This is because G is a composite function which includes a dependence on both on f and St (Eq. 13). In general, a lower G value implies a much better heat transfer performance, and a higher R value indicates a better friction performance. In Fig. 25(a), the correlation corresponding to $e/D = 0.188$ case is sketched using the solid line (Round cornered ribs) and dashed line (sharp cornered ribs), whereas in Fig. 25(b), correlations corresponding to $p/e=10$ (for all three heights) have been sketched.

Benchmarking. Fig. 26 compares results presented in the current work with values presented in [25] and [26]. Though the parameter ranges considered differ vastly, it can be seen that the heat transfer roughness values predicted are similar.

Error analysis. The Kline-McClintock [27] scheme has been used to estimate the experimental uncertainty. The maximum experimental uncertainty in measuring the Reynolds number is estimated to 3%; the maximum experimental uncertainty in Nusselt number (which corresponds with the lowest temperature difference between the plate and the bulk-mean temperature) is estimated to be 8%. Errors in determining the Nusselt numbers are due to bias and precision errors in thermocouple measure-

ments. The uncertainty of the friction factor is estimated to be 8%. Uncertainty in the friction factor is due to precision errors in measuring static pressures in the channel.

Contact resistance. The copper ribs are attached to the copper plates using double sided tape (also made of copper). The contact resistance due to the adhesive layers of the double sided tape could bias the measured Nusselt numbers to a lower value (i.e. a conservative bias). To quantify this effect, an order-of magnitude analysis is performed. Assuming that the copper plate and the rib are both isothermal, a one-dimensional resistance model can be set up (Fig. 27, Eqs. 2.21 and 2.22).

$$\frac{T_{plate} - T_R}{R_{cond}} = \frac{T_R - T_{bulk}}{R_{conv}} = \frac{T_{plate} - T_b ulk}{R_{cond} + R_{conv}} \tag{2.21}$$

$$\frac{T_{plate} - T_R}{T_R - T_{bulk}} = \frac{R_{cond}}{R_{conv}} = \frac{t/kA_c}{1/hA_R} = \frac{\pi h t}{2k} \tag{2.22}$$

The resistance between the plate and the rib (the contact resistance) is R_{cond}. The convective resistance between the rib and the air is R_{conv}. The highest value of h experienced is of the order 1000W/m2-K at Re=400k (assuming average heat transfer coefficient on the rib is equal to the value reported on the plate). Since the tapes are made of copper and have an overall thickness (t) of 0.05mm (including both adhesive layers), the cumulative interface conductivity is assumed to be of the order 0.5 W/m-K (which is very conservative). This yields a ratio (as defined in Eq. 2.22) of 15% for the highest heat transfer case - which indicates a slight conservative bias in the reported Nusselt numbers at the highest Reynolds number. Since the heat transfer coefficient is lower for the other cases, the error due to contact resistance is much lower too.

E.   Conclusions

In this study, the heat transfer and friction characteristics of sharp and round-edged square ribs have been studied and compared. Detailed regionally averaged heat transfer (Nusselt number) enhancement ratio profiles have been presented for both ribbed and smooth surfaces for the parameter range 5<p/e<10, 0.095<e/D<0.19 and 30,000<Re<400,000. Correlations for Nu_R, $\bar{f}$, G and R (heat transfer and friction roughness have been developed).

- In general, at greater heat transfer enhancements (compared to a smooth channel) were observed at larger blockage ratios and at smaller rib-rib spacings. These high heat transfer enhacements were accompanied by large pressure drop penalties (when compared with a smooth channel), resulting in a lower thermal performance.

- At higher values of e/D and Re, the smooth surface also displayed high Nu enhancement.

- Nusselt number enhancement ratio falls with an increase in Re, whereas friction factor ratio rises with an increase in Re, for smooth and ribbed surfaces.

- The heat transfer performance is found to be below unity for cases with large Reynolds number, and large values of e/D.

- A power law correlation is presented for Friction Factor and Nusselt number for the range studied.

- The correlation developed for heat transfer in sharp-edged ribs is found to correlate measured round-edged rib heat transfer data satisfactorily, indicating that the rib profile does not have an effect on heat transfer (for the range studied).

- Friction factors measured for round-edged ribs are found to be lower than those for sharp edged cases - especially at larger values of e/D. It is anticipated that this is because of reduced form drag in the round-edged rib case - due to smaller recirculation zones.

Further studies could focus on extending the correlation to cover the influence of aspect ratio, different rib angles and rib configurations (such as V-shaped and broken-v-shaped ribs). Studies could also attempt to find local heat transfer coefficients (perhaps using IR or Liquid Crystal Thermography).

CHAPTER III

HEAT TRANSFER IN ROTATING 3-PASS CHANNEL

USING CFD

Designs for gas-turbine blade internal cooling passages often incorporate multiple turns as the hub and the tip, as pictured in Fig. 2. Experimental tests on a rotating 3-pass channel have been conducted, and a few issues with the results have been encountered.

A.   Issues with Experiment

Experimental results for the 3-pass rotating rig study show some anomalous features. At high Rotation numbers the inlet temperatures, recorded upstream of the first pass showed values exceeding the exit temperature (recorded at the exit of the third pass, shown in Fig.28(b)). This is physically impossible, since heat is added to the working fluid as it flows through the test section. Temperatures at the hub end wall (located between the second and third passes, also shown in Fig.28(b)) showed an anomalous increase compared to the local bulk mean temperatures. Reported Nusselt numbers also showed a deterioration at higher Rotation numbers - on both leading and trailing surfaces (Fig.28(c)). Open literature reports a deterioration in only on the trailing surface in the radially outward first and third passes, and on the leading surface in the radially inward flowing second pass.

It was suspected that the anomalies in the experimental data were due to secondary flows induced by Rotational buoyancy and Coriolis forces encapsulating flow temperature measuring thermocouples. (Figs.29(a) and (b)).
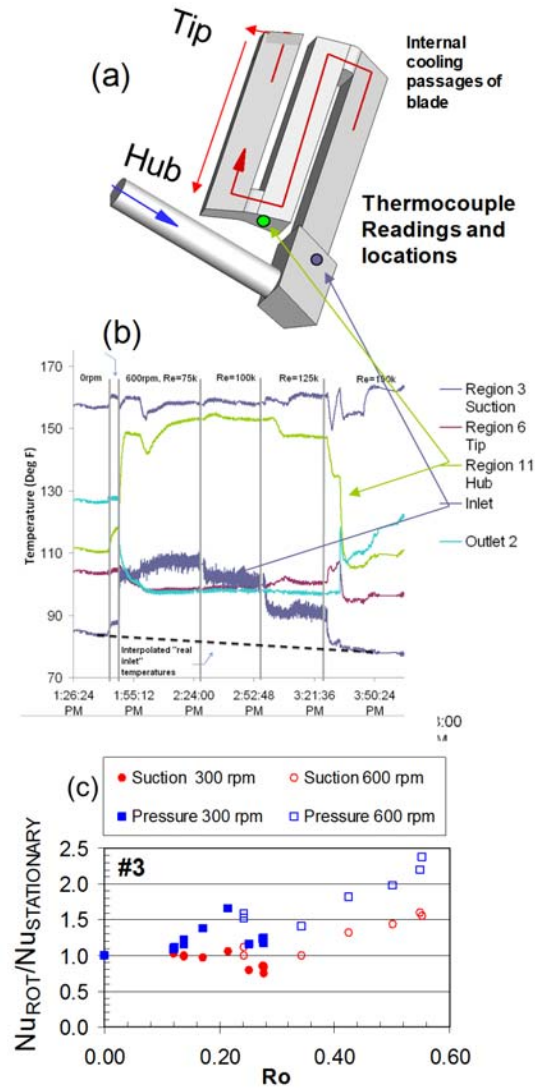
Fig. 28. (a)Flow domain inside 3-pass serpentine channel (b) Temperature record for inlet and hub temperatures, showing anomalies at high RPM / Low Re (c) Anomalous effect of rotation on pressure side, 1st pass (blue).
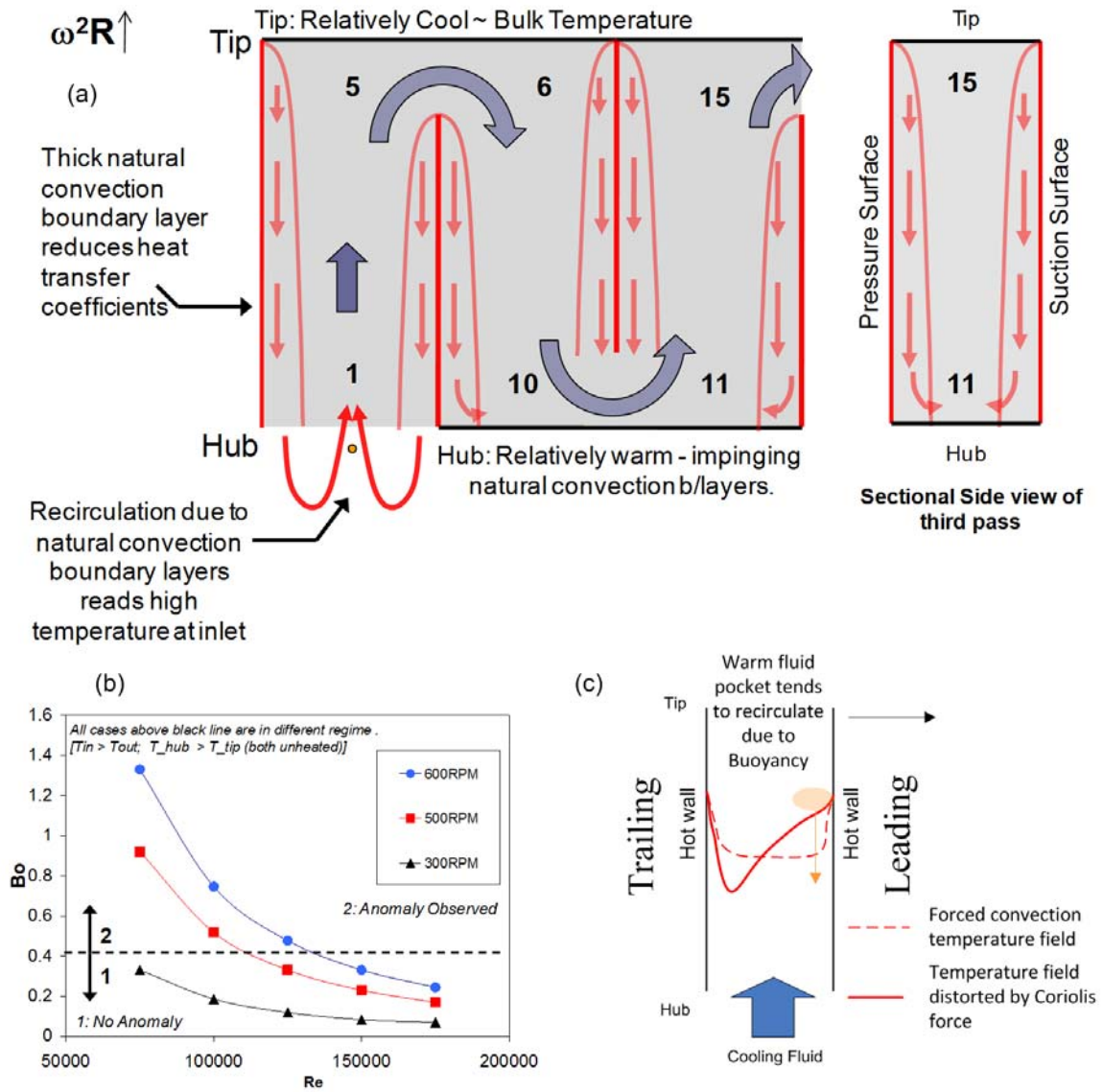
Fig. 29. (a)Suspected flow-field due to buoyancy domination (b) Flows beyond a critical Bo $= Gr/Re^2$ show anomalous behavior (c) Physics of cobmined Coriolis and buoyancy effect.

B.   Literature Survey

1.   Effect of Rotation

The effect of rotation on heat transfer in internal flow configurations has been studied extensively in the literature. Of special significance are the works of Wagner, Johnson and co-workers at the UTRC, (Wagner et al. [28, 29] and Johnson et al. [30, 31]). The fluid dynamics in rotating turbine blades with heated walls is a complex interplay of various forces: inertial, viscous, Coriolis and centrifugal buoyancy. In radially outward flow configurations, the Coriolis force induces counter-rotating secondary circulations within the flowfield, which results in the accumulation of the warmer fluid near the leading surface (reducing heat transfer), and cooler fluid near the trailing surface (increasing heat transfer). Further, the warm fluid near the leading surface experiences a buoyancy force radially inward, creating a recirculation tendency in the flowfield. (Fig.29(c)).

For radially outward passes, various studies [28, 29, 30, 31, 32, 33, 34, 35, 36, 37] show an increase in heat transfer on the trailing surface and a deterioration on the leading surface (even when roughness elements are provided in the channel e.g. Johnson et al. [30]).

Studies into the effect of rotation on pin-fins (Wright et al. [34] and Willett et al. [33])conclude that the effect of rotation is subdued due to the disturbance offered to the Coriolis force induced secondary flows by the large blockage provided by the pin-fins.

2.   Effect of Rotation: CFD

The development of powerful computational methods over the past decade has made it possible to accurately predict heat transfer coefficients under rotating conditions

for ducts with simple geometries. A few landmark works will be discussed to exposit various issues and limiations of the computational work.

Dutta et al (1994). [38] performed a CFD analyis on a channel with radially outward flow, and discussed the combined effect of coriolis and buoyancy forces. A k-ϵ model was used for the computations. Shih et al. [39] used a SST k-ω model with near wall refinement to predict heat transfer in a duct with a U-turn at the tip-region. While their study did show the expected parametric effects of buoyancy and coriolis forces, the match of their results with experiment was poor. Su et al. [11] used a Reynolds Stress model (with near-wall refinement) with in-house code, and matched experimental measurements. More recently, Sleiti and Kapat (2007) [40] used commercial code (FLUENT) to predict the measurements of Wagner et al. [28] with accuracy.

It is therefore clear that commerical code is adequate to predict heat transfer in rotating systems - and has been used for the current study.

C.   Objectives

As explained earlier, the experimental data shows anomalous features. It is suspected that these features are due to the flow-field being tipped into a buoyancy dominated mixed convection regime.

The CFD program was instituted to verify these suspicions and explain the various anomalies encountered with the data. In order to do so, the CFD is run at high RPM using commerical code with temperature dependence of density switched on and off. Also, the geometry considered in the experiment has a tangential inlet to flow in the 1st pass rather than a radial inlet. The simulation tests the sensitivity of the flowfield to the tangential inlet by comparing an 'ideal' (radial) inlet with the

'actual' tangential inlet.

D.   Model Details

Flow is modeled in a rotating frame of reference using source terms to represent the pseudo-forces (centrifugal and Coriolis). All computations are performed using commercial FLUENT code, with conformal near-wall meshes, integrating up to the wall (rather than using wall functions). A total of 4.5M points are used, and the tests were run on the Supercomputer. The SST k-omega model is used to model turbulence. Density is prescribed to vary with temperature ('incompressible ideal gas') to enable the simulation of the rotating buoyancy effect.

Using the Einstien summation notation, the equation for mass-balance is:

$$\frac{\partial \rho}{\partial t} + \frac{\partial \rho u_i}{\partial x_i} = 0 \tag{3.1}$$

The mean-momentum equation (RANS for 3 dimensions) is:

$$\frac{\partial \rho u_i}{\partial t} + \frac{\partial \rho u_i u_j}{\partial x_j} = \frac{\partial p}{\partial x_i} + \frac{\partial}{\partial x_j}\left[\mu\left(\frac{\partial u_i}{\partial x_j} + \frac{\partial u_j}{\partial x_i} - \frac{2}{3}\delta_{ij}\frac{\partial u_k}{\partial x_k}\right)\right] + \frac{\partial}{\partial x_j}(-\rho\overline{u_i'u_j'}) + \phi_i \tag{3.2}$$

Here, ϕ corresponds with the body forces - the coriolis and centrifugal forces. In instances where the radially ourward direction corresponds with the x axis and the angular velocity vector is aligned along the z direction, the vector becomes:

$$\phi = \left[\rho\Omega^2 x + 2\rho v\Omega, \rho\Omega^2 y - 2\rho u\Omega, 0\right]$$

The total energy (E) balance equation (neglecting viscous dissipation terms due to the low Mach numbers involved) is:

$$\frac{\partial}{\partial t}(\rho E) + \frac{\partial}{\partial x_i}[u_i(\rho E + p)] = \frac{\partial}{\partial x_j}\left(k_{eff}\frac{\partial T}{\partial x_j}\right) \tag{3.3}$$

Here, $k_{eff} = k + \frac{c_p \mu_t}{Pr_t}$. FLUENT assumes a default turbulent prandtl number of 0.85.

Since the Mach numbers involved in the flowfield do not exceed 0.1 the flow is assumed to be within the incompressible regime. Density variations, however, are brought about due to significant temperature variations in the flow-field - which gives rise to the Buoyancy force.

Density is specified to be a function of temperature:

$$\rho = \frac{P_{ref}}{RT} \tag{3.4}$$

For the current case, P_{ref} is taken to be 4.5 bar, which is the operating pressure of the experiment.

The closure of the above turbulent mass, momentum and energy balance equations, requires local turbulent viscosities. For the current work, these quantities are estimated by the SST k-ω model.

FLUENT solves the turbulent kinetic energy (k) and specific dissipation rate ($\omega = k/\epsilon$) transport equations simultaneously to estimate the turbulent viscosity.

$$\frac{\partial}{\partial t}(\rho k) + \frac{\partial}{\partial x_i}(\rho k u_i) = \frac{\partial}{\partial x_j}\left(\Gamma_k\frac{\partial k}{\partial x_j}\right) + G_k - Y_k \tag{3.5}$$

$$\frac{\partial}{\partial t}(\rho \omega) + \frac{\partial}{\partial x_i}(\rho \omega u_i) = \frac{\partial}{\partial x_j}\left(\Gamma_\omega\frac{\partial \omega}{\partial x_j}\right) + G_\omega - Y_\omega \tag{3.6}$$

Γ_k and Γ_ω are effective diffusivities. G_k and G_ω are the production terms for k and ω respectively; Y_k and Y_ω are the dissipation terms for k and ω respectively. Further details are available in the FLUENT manual. [41].
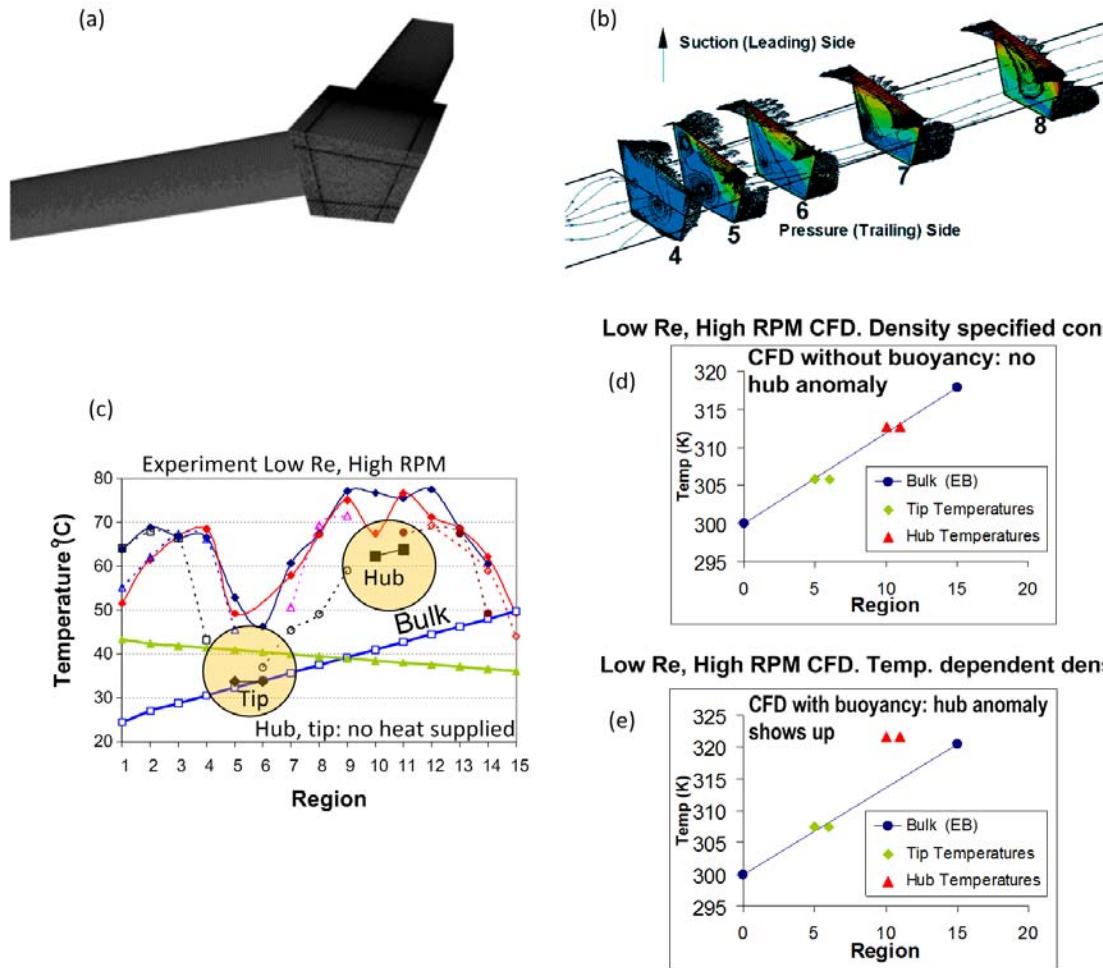
Fig. 30. (a)Mesh for 1st pass (similar for all 3 passes) (b) Flow reversal in 1st pass for typical high Ro cases (c) Details of experimental hub anomaly for high Ro case. Low Ro cases do not see anomaly. (d) Hub and tip temperatures predicted using CFD with constant density at high Ro (no Buoyancy) (e) Hub and tip temperatures predicted using CFD with Temp. dependent density at high Ro. Hub anomaly shows up in CFD.
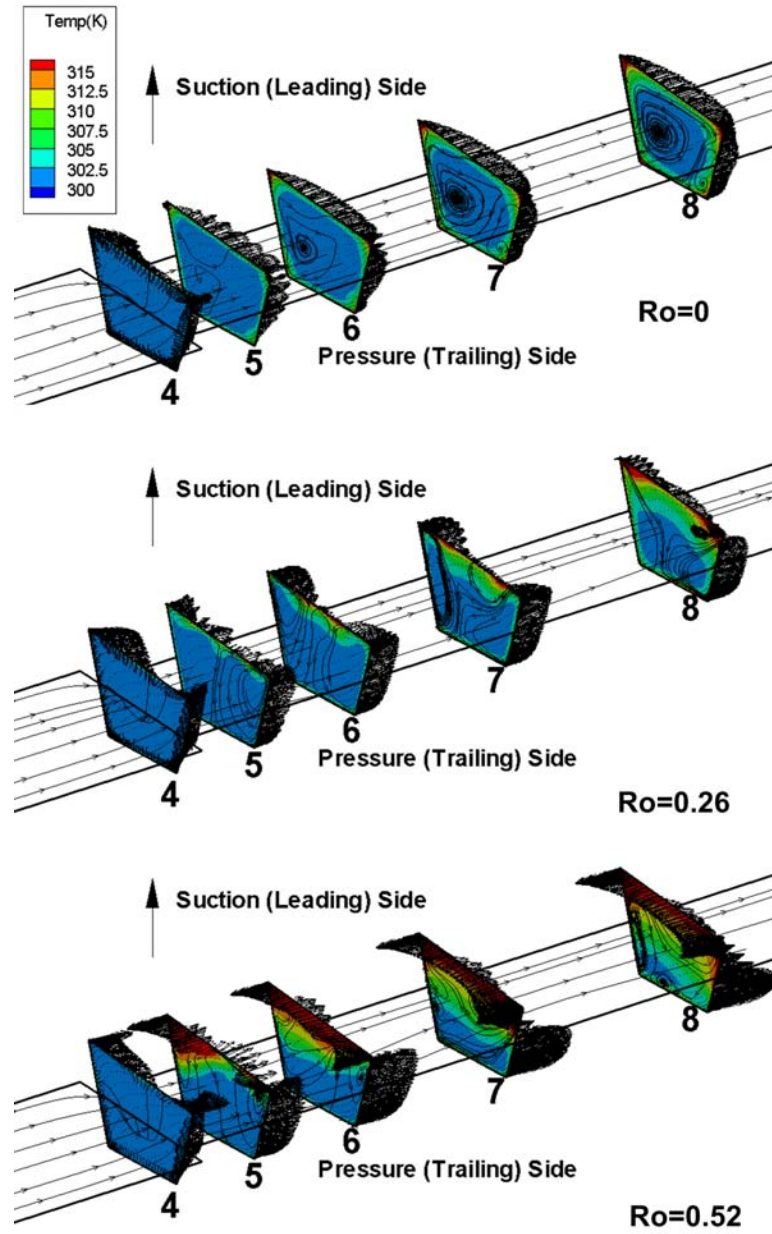
Fig. 31. Computed flow-field for 3 different rotation numbers, indicating large Buoyancy induced recirculation for higher rotation number.

Table II. Recirculation tendency: CFD and experiment.

Ro	Experiment Temperature Anomaly	CFD: Recirculation Tendency
0	None	None
0.13	None	None
0.26	Yes	Mild
0.39	Yes	Strong
0.52	Yes	Massive

E.   Important Results

For the radial inlet case, at higher rotation numbers, results show the establishment of a significant temperature gradient within a stream-wise cross section of the passage. Fluid more proximate to the leading side (the suction side) is much warmer than the fluid adjacent to the trailing side. This stratification of the flow field is expected, as per open literature - and is attributed to the Coriolis force. Also, in the simulations, a tendency for flow reversal is observed in the zone of the warmest pocket (located adjacent to the leading surface). Massive recirculation of the flow is observed at the highest Rotation number (Fig.30 and 31) This tendency to recirculate is correlated with the experimental cases that experience the inlet temperature anomaly (Table II). However, this recirculation observed in the CFD is not powerful enough to penetrate into the plenum and encapsulate the temperature measuring thermocouple. The experimental configuration included a tangential inlet to the plenum that feeds the first pass, rather than a conventional radial inlet. A couple of screens were provided upstream of the test section, with the expectation that they would straighten the

flow out. In the computations, using a tangential inlet, (rather than a purely radial inlet) does change the flow field in the first pass under rotating conditions. The swirl induced by the tangential inlet interacts with the secondary vortices induced by the Coriolis force, strengthening one and weakening the other (Fig.32). This strengthening and weakening of vortices results in a change in the location of the pocket of warm recirculating flow from the leading surface to the outer wall, encompassing portions of both the leading (suction) and trailing (pressure) surfaces. This explains the deterioration of heat transfer in on the pressure (trailing) surface in the first pass. The CFD results do not match exactly the experimental trend, but hint at deterioration on the both the leading and trailing side for the tangential inlet. No deterioration on the trailing side is observed by the CFD in the radial inlet case.

In the experiment, the hub end wall heater (between the second and third passes) was not operational, so the wall was essentially adiabatic. From fundamental theory, the temperature at the hub should have been equal to the local bulk mean temperature. This was indeed the case for the low-Ro non-anomalous cases. But in high Ro cases, the experiment showed anomalously high hub temperatures - even higher than the coolant exit temperature, on occasion. (Fig.30). Temperature fields computed by the 3 pass CFD (Fig.33) did indeed report similar behavior to that shown in the experiment. The temperatures on the hub (assumed adiabatic) are anomalously higher than the local bulk mean temperature at higher values of Ro. This anomaly seems to increase in magnitude with Ro - another trend consistent with experiment. To investigate whether this anomaly was caused by rotating buoyancy as speculated, test are run stipulating that the density of the fluid remain constant, rather than vary with temperature. thus eliminating centrifugal buoyancy. And on doing so, it is noticed that the hub anomaly disappears. (Fig.30).This provides *conclusive proof* that rotational buoyancy causes the hub anomaly. The constant density solution does
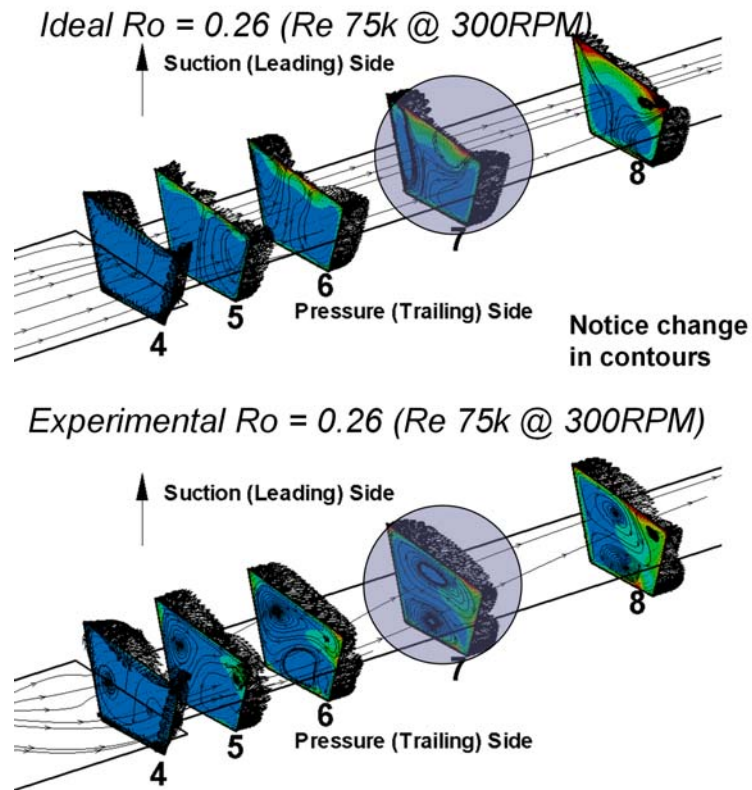
Fig. 32. Comparison of computed flow-fields using ideal and actual indicated for intermediate rotation numbers.
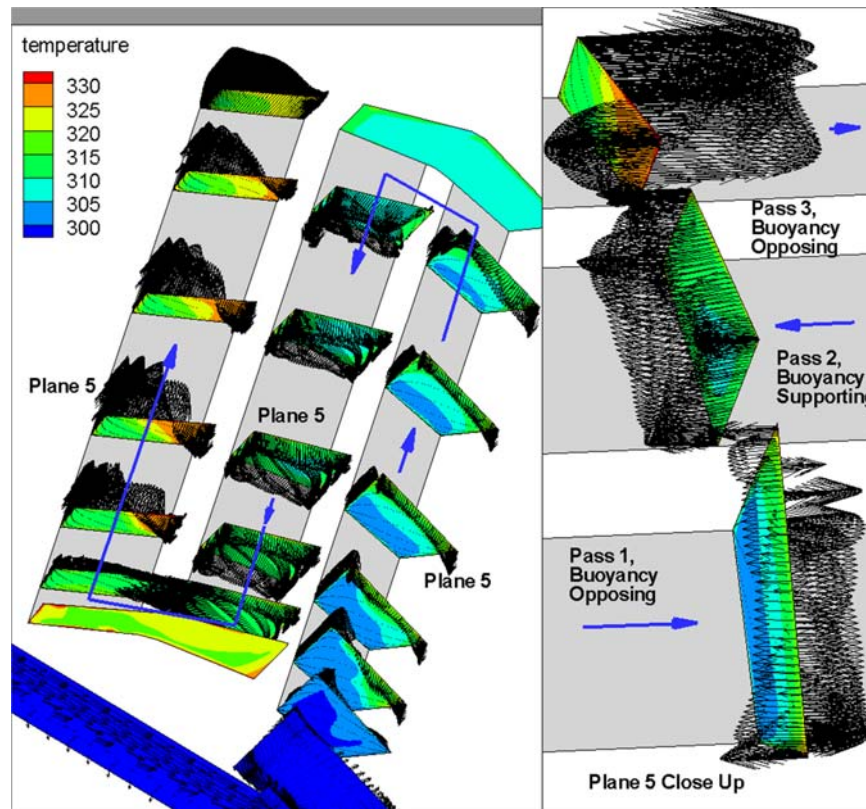
Fig. 33. Computed three-pass flow-field.

not show any recirculation in the first pass - and only a relatively minor recirculation in the third pass.

The hub anomaly, in the experiment was also accompanied with very low heat transfer coefficients in regions proximate to the hub. This resulted in very high local temperatures. These low heat transfer coefficients are also observed in CFD in regions proximate to the hub.

F.   Conclusions

In conclusion, the computational simulations prove that the flow does indeed recirculate (at the same Ro values as experiment) due to rotational buoyancy; a severe deterioration in heat transfer can occur near the hub (between radially inward and radially outwards passages). CFD also suggests that the complexity of the geometry (tangential inlet, changes in cross section and angle between various passes, asymmetric U-turns etc.) alters the secondary Coriolis induced vortices, thus making the data deviate from open literature.

While the CFD does hint at several experimental trends, there are significant differences between the CFD and experiment. These differences do not invalidate the experiment, because, the CFD model does not have the resolution and capacity to pick up the intricacies of separated / recirculating flows.

CHAPTER IV

EXPERIMENTAL INTERNAL HEAT TRANSFER WITH ROTATION -

ROTATING TRAILING EDGE WITH PIN-FINS*

Earlier chapters focused on experimentally measuring heat transfer coefficients on a stationary channel and numerically assessing the impact of rotation on heat transfer. This chapter will focus on experiments which measure the effect of rotation on heat transfer in an important configuration the trailing edge region of a rotor blade. High quality experimental data is scarce in the open literature for this configuration.

A.   Introduction

Pin-fins are widely used to cool the trailing edge of gas turbine engine rotor and stator blades. Pin-fins offer significant heat transfer enhancement, are relatively easy to fabricate and also offer structural support to the hollow trailing edge region.

The flow physics in a pin-fin roughened channel is very complicated and three dimensional. Flow proximate to the bounding walls of the pin-fins has characteristics similar to internal flow inside a duct. Flow separation and laminar-turbulent transition occur on each individual pin - at different circumferential locations dependent on the configuration of the pin in an array, as reported by Metzger and Haley [42].

Studies by Goldstein and Chyu [43] and later, Chyu et al. [44] show the heat transfer coefficient distribution on the endwall due to a single pin-fin. Regions of flow separation immediately downstream of each pin-fin resulting in low heat transfer and

* Reprinted with permission from A.P. Rallabandi, Y.H. Liu and J.C. Han, Heat transfer in trailing edge wedge-shaped pin-fin channels with slot ejection under high rotation numbers, in: Proc. ASME Turbo Expo 2010 Paper No: GT2010-22832 (2010).

regions of flow reattachment (with high heat transfer) further downstream are shown clearly.

In gas turbine engines, an array of pin-fins is used rather than a single pin-fin. Heat transfer is enhanced due to an increase in total area due to the pin-fins as well as the alteration of the flow-field due to pin-fins. This results in a sensitivity of heat transfer coefficient to pin-fin arrangement. A consensus in literature (Vanfossen et al. [45], Chyu et al. [46] and Metzger et al. [47], for example) is that staggered arrangements provide higher heat transfer coefficients than in-line arrangements - both on the end wall as well as the fin itself. Chyu et al. [46] provide a graphite-oil streakline visualization of flow-fields associated with in-line and staggered pin-fin arrangements. The staggered arrangement clearly shows a more disturbed (and hence more turbulent) flowfield than the in-line case, suggesting higher overall heat transfer (and higher pressure drop).

The first row of pin-fins in both in-line and staggered arrays registers a lower heat transfer coefficient than subsequent inner rows. As the flow progresses into the pin-fin array, more turbulence is created, blockage due to pin-fins speeds up the flow in certain zones, flow separation occurs along the pin-fins, horseshoe vortices associated with the pin-fin and endwall further turbulate the flow-field and high heat transfer reattachment zones are created. This significant increase in turbulence results in an increase in heat transfer. At around the fourth row, however, these flow phenomena appear to become periodic - and the heat transfer coefficient stops increasing, and settles at a final 'fully developed' value. This is also a common observation in literature, [42], [45], and more recently, Ames et al. [48].

In general, a lower Reynolds number typically results in a larger enhancement in heat transfer in comparison with a corresponding flow in a smooth channel. These trends are valid for both the pin-surface and endwall, as reported by Chyu et al.

[49]. It was also observed that the end-wall has a 10%- 20% lower heat transfer coefficient than the pin-fins themsevles. Packing in more pin-fins into the channel results in higher total heat transfer rates from the channel, for the various spacing ratios studied by Metzger et al. [50]. Since turbine blades are manufactured by the investment casting process, a prominent fillet occurs between the base of the pin-fin and the endwall. This fillet results in a reduction of heat transfer coefficient [51], due to the suppression of the horseshoe vortices formed at the base of each pin-fin. Partial pin-fins with tip clearance have been studied by Arora and Abdel-Messeh [52] to simulate the placement of a stator insert inside the stator casing. A reduction in the friction factor at large tip clearances due to partial pin-fins was observed.

Pin-fins are typically used in the trailing edge of the blade. Spent cooling fluid is often discharged into the mainstream through holes machined within the trailing edge. The effect of trailing edge ejection on heat transfer in a pin-fin roughened channel has been studied by Lau et al. [53] and Kumaran et al. [54]. Heat transfer inside the channel is found to decrease as fluid is removed through ejection holes, along the channel. Also, heat transfer inside long ejection holes was found to be well predicted by the Dittus Boelter correlation. The effect of lateral ejection was also studied by Hwang and co-workers [55, 56], where it was determined that ejection resulted in an increase in heat transfer proximate to the extraction region, and a reduction in heat transfer in the wall opposite to the ejection slot.

The effect of rotation on heat transfer in internal flow configurations has been studied extensively in the literature. Of special significance are the works of Wagner, Johnson and co-workers at the UTRC, (Wagner et al. [28, 29]and Johnson et al. [30, 31]). The fluid dynamics in rotating turbine blades with heated walls is a complex interplay of various forces: inertial, viscous, Coriolis and centrifugal buoyancy. In radially outward flow configurations, the Coriolis force induces counter-rotating

secondary circulations within the flowfield, which results in the accumulation of the warmer fluid near the leading surface (reducing heat transfer), and cooler fluid near the trailing surface (increasing heat transfer). Further, the warm fluid near the leading surface experiences a buoyancy force radially inward, creating a recirculation tendency in the flowfield.

For radially outward passes, various studies [28, 29, 30, 31, 32, 33, 34, 35, 36, 37] show an increase in heat transfer on the trailing surface and a deterioration on the leading surface (even when roughness elements are provided in the channel e.g. Johnson et al. [30]).

Studies into the effect of rotation on pin-fins (Wright et al. [34], Willett et al. [33] and Chang et al. [57])conclude that the effect of rotation is subdued due to the disturbance offered to the Coriolis force induced secondary flows by the large blockage provided by the pin-fins.

More recently, heat transfer in wedge shaped trailing edge channels (with a U-turn at the tip region) in stationary and rotating conditions was studied by Wright et al [58]. Lower heat transfer in the narrower region of the wedge away from the U-turn was recorded. An increase was measured on all surfaces (including the leading surfaces) due to rotation. Liu et al. [59] studied a similar trailing edge model including slot ejection along the length of the channel rather than a U-turn at the tip. Heat transfer coefficients in the narrower region of the duct, which seemed subdued in [58] were found to increase due higher local velocities associated with flow ejection. Also, the increase in local rotation number (due to a reduction of the local Reynolds number because of flow ejection) results in a larger asymmetry in heat transfer between the leading and trailing surfaces due to prominent Coriolis vortices.

Chang et al.[60] report centerline data in a rotating trailing edge model with flow extraction along the length, roughened with rib-turbulators, and report a significant
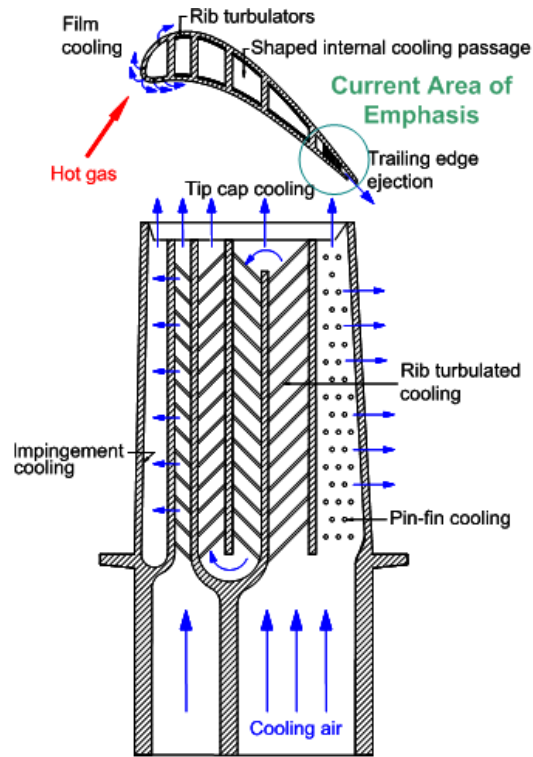
Fig. 34. Schematic of gas turbine blade, showing various different cooling techniques commonly used. Current area of emphasis is the trailing edge region, as shown.

Buoyancy number for the parameter range studied.

Experimental methods used to determine heat transfer coefficients in pin-fin channels include the napthalene sublimation mass-transfer analogy as well as the copper-plate regional average method, where pin-fins are affixed to the copper plate with good thermal contact. This thermal method is subject to a 'fin effect' within the pin-fin, wherein a temperature variation from the base to the center of the pin-fin also occurs. This fin effect is much less pronounced in scaled down laboratory tests than actual engine conditions, where the heat transfer coefficients are higher and materials have a much lower thermal conductivity.

B. Objective of Current Work

In the current work zone-wise detailed effect of rotation on a pin-fin roughened wedge-shaped trailing edge model is presented. The region of emphasis on the gas turbine blade is highlighted in Fig.34.

The pin-fins in consideration are full (i.e they extend from the leading wall to the trailing wall of the trapezoidal channel) as well as partial, with a height equal to the diameter. Partial pin-fins are studied because they offer a lower friction factor than comparable full pin-fins. A typical staggered ($S_x = 2.75d$ and $S_y = 0.95d$) pin-fin distribution is studied.

Reynolds, rotation and buoyancy numbers encountered are similar to those in an actual aero-engine. The mean density ratio (Eq.4.5) tested for all cases is approximately 0.12. The copper plate regional average temperature method is used to simulate the buoyancy effect inside the channel. All results reported are based on projected (smooth) area, unless otherwise mentioned.

C. Experimental Setup

A pressurized rotating rig (Fig.35) is used to perform the experiments. Pressures up to 6 bar (abs) are reached inside the pressure vessel. This allows the flow configuration to reach high rotation numbers at the inlet of around 0.6, for Reynolds numbers around 10,000. Compressed air is ducted into the test section as shown in Fig.35, through a rotary union provided at one end of the shaft. This air then flows through a specially designed test section installed inside the pressure vessel from which heat is extracted. This air then flows out through another rotary union installed at the other end of the shaft. The mass flow rate of the air is measured upstream of the first rotary union, using a 12.7mm (0.5") dia square edged orifice flowmeter.
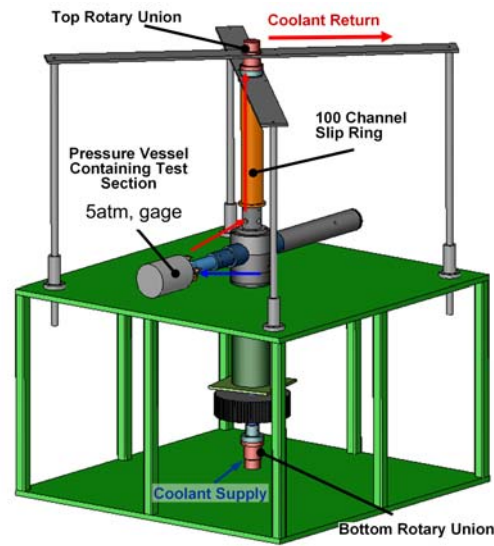
Fig. 35. Image showing rotating arm, pressure vessel, slip ring and rotary unions.

A 100 channel slip ring assembly is used for communication with the test section. Thermocouple wires are connected through the slip ring to the test section inside the pressure vessel. Temperatures of the copper plates within test section are monitored using NI's SCXI hardware through the LABVIEW program. Each heater installed in the test section is controlled by a variac, also connected through the slip ring assembly.

Figure 36 shows the test section in consideration. As shown in the image, the test section is comprised of seven streamwise arrays of copper plates, labeled A-G. The leading and trailing walls have three of these arrays each, and the outer sidewall has one such array (G). Each of these arrays has six sequential thermally isolated regions extending from low x/D to high x/D, numbered 1 through 6. The heat supply to the plates in a given array is controlled by a single heater, as shown in Fig.36. Seven silicone rubber coated resistance heaters, corresponding to plate arrays A-G are installed overall. Heaters are custom manufactured by Watlow Inc. with
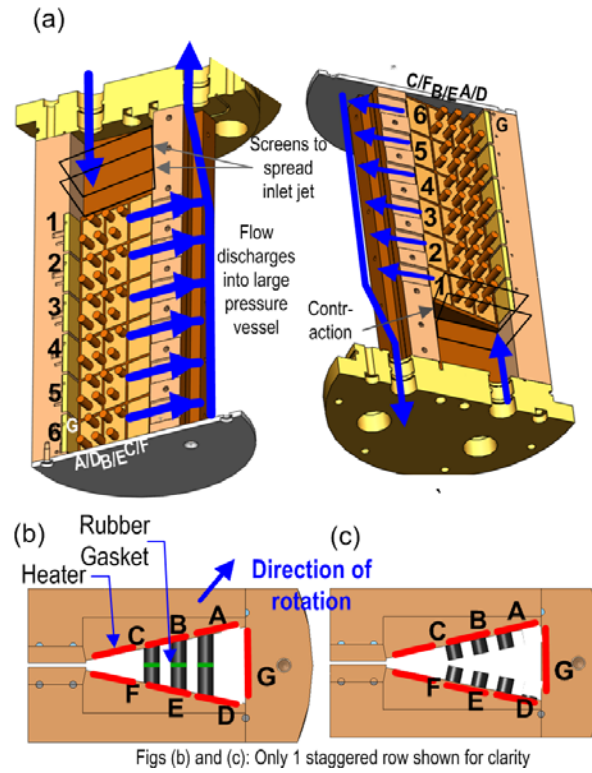
Fig. 36. Arrangement of pin-fins in test section.
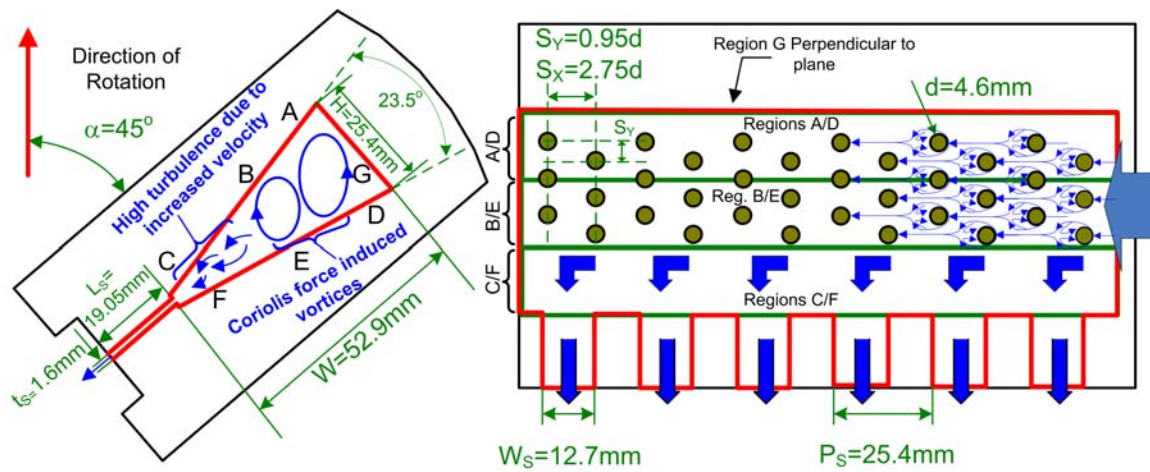
Fig. 37. Various important dimensions in test section, showing details of pin arrangements and flow schematics.

accommodation to secure the copper plates to the test section using a bolt.

The test section is made of garolite, a low conductivity plastic. Grooves for each plate are machined into the garolite to provide thermal insulation between the plates. A thermocouple junction is buried inside each copper plate and is routed to the DAQ module through the slip ring assembly.

Pressure taps are machined into copper plates adjacent to the slot to obtain the local pressure. Also, static pressure is measured downstream of the slots by means of a pressure probe. The difference in static pressures across the slots gives information regarding the local Reynolds number in the test section. These pressures from the rotating frame of reference are communicated to the stationary frame by means of a rotating manifold, commercially available from Rotary Systems Inc. They are then measured by a Dwyer U-Tube manometer. Since the pressures in question are very large, only differential pressures are measured.

Channel dimensions. Important dimensions of the channel have been documented in Fig.37. Further, the heated length of the channel is 155.7mm and the hydraulic diameter is 22.16mm. Each copper plate on the leading and trailing surfaces is 24mm in length (streamwise direction), and 16mm in width (spanwise dimension). The copper plates on the outer wall (G) are 24mm long and 25.4mm wide. The thickness of the insulating garolite layer between two copper plates is 1.4mm. The six slots provided on the narrow edge of the channel are also shown in Fig.37. The cross sectional area of the channel to the combined six slot area ratio is 6.

Enterance and exit conditions. A sectional view of the channel (including two screens upstream of the test section) is shown in Fig.36. The flow undergoes an expansion, passes through two screens and undergoes a contraction upstream of the test section, which helps generate a developing boundary layer.

Figures 36 and 37 show the ejection slots machined into the test section. Flow is

Table III. Total (wetted) area to smooth (projected) area ratios for full and partial pin fins.

Region	Num. of Pins	Full Pins A_t/A_s	Partial Pins A_t/A_s
A/D	3	1.99	1.52
B/E	3	1.65	1.52

discharged from the slots to the relatively large isobaric pressure vessel which houses the test section. The volume of the pressure vessel is much larger than that of each individual slot, and crossflow effects are not anticipated to be significant. Concerns regarding the effect of the enterance and exit conditions on the data are discussed in the results section.

Pin-fin arrangement details. The diameter(d) of the pin-fins in both cases (partial and full) is equal to 4.6mm. The spacing between the pins in the streamwise direction (S_x) is 2.75d and the spanwise (S_y) directions is 0.95d, as defined in Fig.37. The height of the partial pin-fins is equal to the diameter, yielding a blockage ratio (e/D) of 0.2. The solidity of the partial pin-fin roughened channel is 5% and the full pin-fin channel is 9%. Pin-fins made of high thermal conductivity copper as well low thermal conductivity garolite are tested. A thin layer of super-glue adhesive is used to attach the pin-fins to the copper plates. Heat transfer enhancements recorded for the garolite pin-fin case are expected to reflect the enhancement at the hub region alone. Each conductive pin fin is divided by an insulating layer (rubber gasket, 0.5mm thick) at its middle to ensure that heat does not leak from the leading side to the trailing side (or vice-versa).The arrangement is shown in detail in Fig.36. Area enhancements due to pin fins are shown in Table III. The area enhancement for the leading surfaces

(Table III) includes half the area of the full pin fins shared by the leading surfaces and the trailing surfaces - as does the area enhancement reported for the trailing surfaces.

D.   Data Reduction

1.   Local Reynolds Number

In order to estimate the flow rate through each of the six slots accurately, differential pressures are recorded through the pressure taps installed upstream and downstream of each slot. Based on the recorded differential pressure for slot i, ΔP_i, assuming that the discharge coefficient through each slot (C_D) is identical, one can estimate the velocity through each slot thus:

$$\sqrt{\frac{2\Delta P_i}{\rho C_D}} = V_i \tag{4.1}$$

Also noting that mass balance requires:

$$\sum_{i=1}^{i=6} \rho V_i A_S = \dot{m} \tag{4.2}$$

Solving Eqs.(4.1) and (4.2) simultaneously, one obtains unique discharge coefficients for every Reynolds number, as well as velocities through each slot. Knowing the flow rate discharged through each slot, one can estimate the local Reynolds number $(Re_x = \frac{4\dot{m}_x}{\mu P})$ number based on the known local mass flow rate $\dot{m}$ and perimeter P. In this current work, the velocity scale used for the Reynolds number is equal to the bulk mean velocity at a given cross section, and not the maximum velocity.

2.   Heat Transfer Coefficients

Silicone rubber heaters are used to generate heat which is dissipated within the test section. The resistance of each heater, R Ω is measured before each run. The voltage, V Volts, supplied across each heater is measured by a multi-meter. The thermal power generated by the resistance heater is given by V^2/R Watts.

Each heater is affixed to six copper plates (regions 1-6). The heater provides constant heat flux along its length. Changing the voltage across the heater changes the steady state temperature measured on each copper plate. Since heat transfer coefficients vary from region to region, it is not possible to control the temperature recorded for each plate to a constant value. The voltages across the seven heaters (A-G) are actively controlled to ensure that the temperatures measured at region 4 are as close as possible to 65^oC.

An energy budget for each plate is performed to obtain the heat transfer coefficient.

$$h = \frac{q/A_s - q''_{loss}}{(T_w - T_B)} \tag{4.3}$$

Here, q''_{loss} is the heat loss, which is determined based on a test. A low conductivity material is placed inside the test section inhibiting heat transfer within the test section. The heaters are energized, with zero bulk flow. The voltage across the heaters is adjusted to control the steady state temperature at region 4. Two steady state temperatures are studied - one lower than the range encountered in the test, and one higher. Based on these two temperatures, a heat loss characteristic is obtained for each of the copper plates. Heat loss tests are run at all RPM values, to account for the higher heat losses associated with higher velocities of ambient air relative to the rotating can.

The local bulk mean temperature T_B in Eq.4.3 is linearly interpolated from the value measured at the exit of slot 6 (the slot located at the largest value of x/D). A_s

is the projected (smooth) surface area, which corresponds to the area of the copper plate.

The Nusselt number for the current study is defined as $Nu = hD/k_{air}$.

A non-dimensional analysis similar to that provided by Guidez et al. [32] identifies the following parameters that govern the heat transfer phenomena under rotating conditions:

The Rotation Number:

$$Ro = \frac{\Omega D}{V} \tag{4.4}$$

Density Ratio:

$$DR = \left(\frac{\Delta \rho}{\rho}\right)_x = \left(\frac{T_w - T_i}{(T_w + T_i)/2}\right)_x \approx 0.12 \tag{4.5}$$

The effect of these parameters can be combined into the buoyancy parameter, Bo. In this current work, the mean buoyancy parameter $\overline{Bo}$ is computed thus:

$$\overline{Bo} = \frac{\overline{Gr}}{\overline{Re}^2}\frac{\overline{R}}{D} = \left(\frac{\overline{\Delta \rho}}{\rho}\right)\frac{\overline{R}}{D}\overline{Ro}^2 \tag{4.6}$$

The over-bar denotes the mean values of the parameters in question. The mean radius $(\overline{R})$ corresponds to the distance betwen the axis of rotation and the center of the test section (Region 4); the mean density ratio corresponds to the bulk mean temperature at the center of the test section and the mean Reynolds number is based on the mass flow rate at region 4.

In order to isolate the effect of rotation and to eliminate the Reynolds number effect, data for rotating conditions is presented as a ratio: Nu/Nu_s, where Nu_s is the measured stationary Nusselt number for the same Reynolds number. For a given region, data acquired for different runs (of Re and RPM) can be correlated against

either Ro or Bo, with the bulk-to-wall coolant density ratio as a parameter. Thus obtained correlations are scaleable to engine conditions.

3. Uncertainties

The main source of error in determining the Reynolds number (based on [27]) is the resolution of the inclined manometer used to measure the pressure across the orifice. Reynolds numbers are estimated with an error of 5%. The error estimate for the Nusselt number is 4%. The error estimate for the Nusselt number enhancement due to rotation (Nu/Nu_s) is 6%. The measured resistance of the heaters is found to change less than 0.5% for the operating range of temperatures.

Based on a thermal resistance model, it has been determined that using super-glue layer (around 0.02mm thick) to affix pin-fins to the copper plates does result in a minor conservative bias (less than 10%) in heat transfer coefficients reported on regions A and D at the highest Reynolds number for the full copper pin-fin case. The corresponding error for all other locations, pin-configurations and Reynolds Numbers is lower.

E. Results and Discussion

Entrance effects. It is possible that the enterance condition (detailed in Fig.36(a)) could result in the inlet fluid jet passing unbroken through the two screens, lending a negative bias to the data in regions C and F located in the narrow region of the trailing edge.

That this is not the case is proven by the following consideration based on acquired data: In the current scenario, where slot ejection is also incorporated, the data shows relatively *high* heat transfer in regions C and F proximate to the slot -
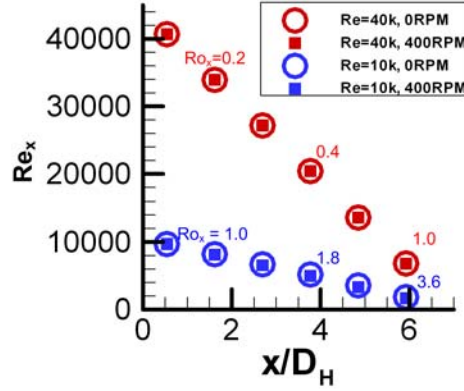
Fig. 38. Local Reynolds number distribution for 0 and 400rpm at Re = 10,000 and 40,000 for partial pin-fins. Data for smooth channel and full copper pin-fins channels are also measured to be identical.

for the smooth and pin-fin roughened cases (compared with Regions A,B,D and E). Futher, regions C and F report constant heat transfer along the entire length of the test section (suggesting uniform discharge, as discussed next section) for the smooth (and rough) cases. This alone strongly suggests that the reported data does not suffer from any significant enterance bias. Further, prior data acquired on the same test section (with slot ejection into a cross-flowing channel [59] shows higher heat transfer coefficients in Regions C and F compared with other regions, corroborating current observations.

1.   Local Reynolds Number

For the different cases measured (smooth, partial pin-fins and full pin-fins), it is found that the pressure difference across each slot is very similar, regardless of the streamwise location or RPM. This results in a linear decline in the local Reynolds number of the flow, as shown in Fig. 38. This can be attributed to the large ratio of the channel cross sectional area to the cross sectional area of each slot (36). Since the

tests are run in a pressure vessel, velocities within the slot are in the incompressible regime, with the Re=40k case registering a 33m/s velocity.

That the flow rate though each slot is approximately equal is further corroborated by the heat transfer coefficient distribution on Regions C and F in Fig. 39(a), as discussed in the following section.

<div align="center">2.   Stationary Heat Transfer Coefficients</div>

Smooth channels. The slot geometry in consideration is very similar to that studied in [59], which provided a discharge from the slot into a cross-flowing section. Consequently, results pertaining to the smooth channel are qualitatively similar. Regarding the stationary cases, on observing Fig. 39(a) and Fig. 40(a), the following trends are noticed:

1. Heat transfer coefficients on the side wall (G), inner wall (A,D), and mid span (B,E) regions show a tendency to decrease with increasing x/D_H, along the channel. This can be attributed, both, to a weakening of the inlet enterance effect as the flow progresses downstream, as well as to a reduction in local Reynolds number due to discharge through the slots machined in the trailing edge. This effect is most prominent on the side-wall, and reduces in strength closer to the outer wall.

2. Heat transfer coefficients on the outer walls (C,E) are the highest, and do not show a decrease with increasing local x/D_H. Since local pressure measurements indicate that the mass flow rate through each slot is almost identical, the amount of fluid flowing in the span-wise direction over regions C and E, to be discharged through the slots is also almost identical. This high velocity flow rate (due to the converging nature of the flowfield proximate to the slot in regions C and E)
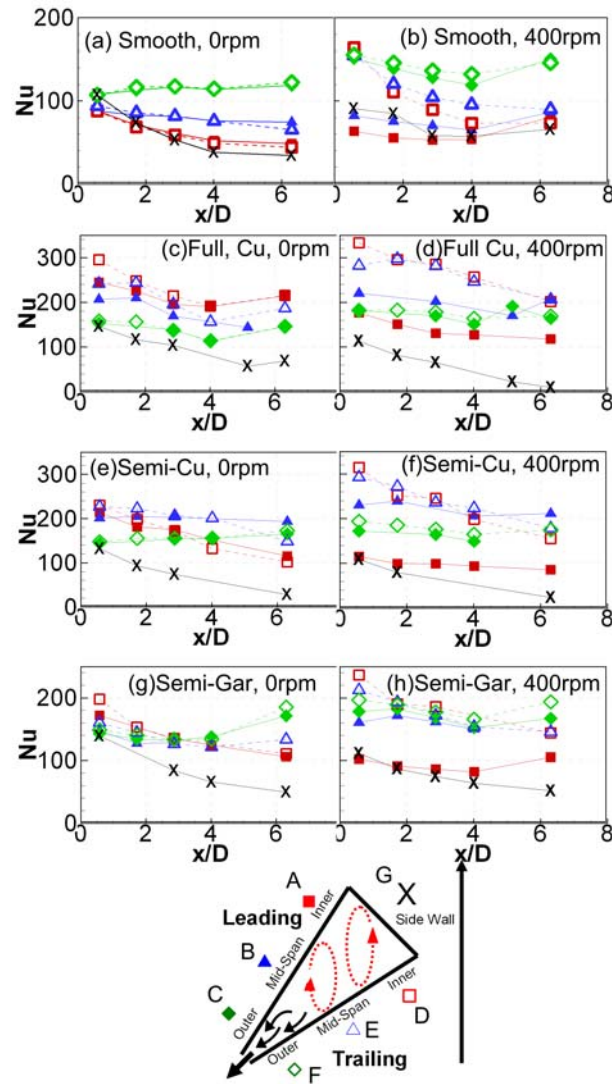
Fig. 39. Local Nusselt number distributions for 0 and 400rpm at Re = 10,000, for (a,b)Smooth (c,d)Full copper pin-fins (e,f)Partial copper pin-fins (g,h)Partial garolite pin-fins.
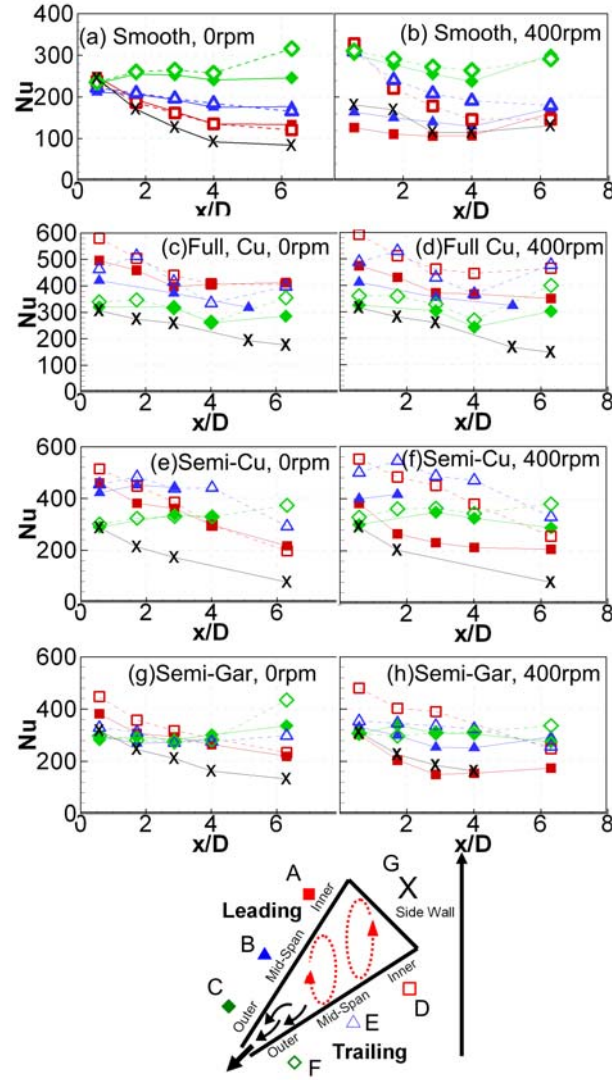
Fig. 40. Local Nusselt number distributions for 0 and 400rpm at re = 40,000, for (a,b)Smooth (c,d)Full copper pin-fins (e,f)Partial copper pin-fins (g,h)Partial garolite pin-fins.

enhances mixing and increases the local heat transfer coefficient on the outer walls.

Full conducting pin-fins. For a stationary channel, the effect of using full copper pin-fins can be appreciated by comparing Fig.39 (a) and (c) as well as Fig.40 (a) and (c). The arrangement detailed in Figs.36 and 37 shows that pin-fins are installed only on the inner and mid-span walls. The benefits of using pin-fins from a heat transfer perspective are apparent in the measured Nusselt number plots. Regions A and D, corresponding to the inner-wall show an increase of 250% to 300% compared to smooth cases for both the Reynolds numbers in question. Mid-span regions, B and E also show an enhancement of around 200%. Outer wall Regions C and F show a relatively small increase (around 10-20%) in the already-high heat transfer coefficient. Heat transfer enhancement due to the copper pin-fins can be due to both, an increase in surface area due to the pins, (TableIII) as well as due to increased heat transfer on the endwall due to various coherent structures induced by the fins. A summary of various structures, pertient to full conducting pin-fins gleaned from literature is presented in Fig.41(a).

Partial conducting pin-fins. Comparing Figs.39(c) and (e), Figs.40(c) and (e), it can be noted that using partial pin-fins instead of full pin-fins results in a minor reduction ($\approx$ 20%) in heat transfer coefficient. Since all the partial pin-fins are of equal length, the area enhancement due to each pin-fin is identical. Inner wall regions A and D benefit from longer full pin-fins due to their larger physical separation. Measurements for partial pin-fin roughened configurations therefore show significant reduction of Nu in regions A and D compared to full pin-fins. In the mid-chord region (B and E), since the area reduction due to using partial pin-fins instead of full pin-fins is less significant, the difference in measured heat transfer coefficients for
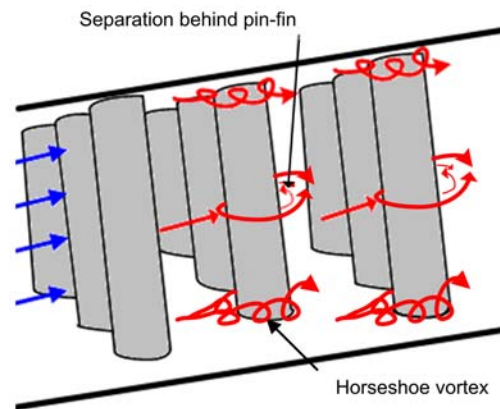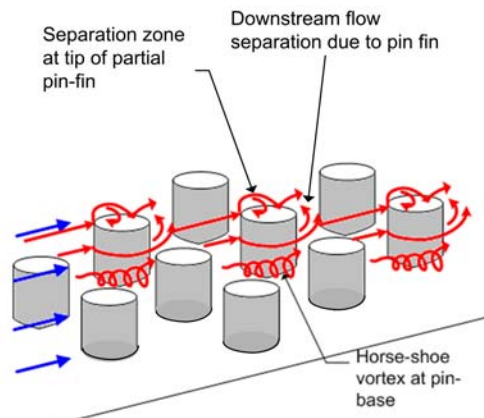
Fig. 41. (a) Sketch of anticipated flow structures due to full pin-fins (b) Sketch of anticipated flow structures due to partial pin-fins.

regions is also lower. A minor increase in heat transfer is observed for some regions, possibly due to additional turbulence generated by the tip of the pin-fin, as detailed in Fig.41(b). Heat transfer coefficients in region C and F (outer wall regions) remain unaffected, when comparing full and partial pin-fins.

Partial non conducting pin-fins. Heat transfer enhancement due to pin-fins can occur because of area increase as well as due to the turbulent coherent structures induced by the pin-fins increasing the heat transfer coefficient on the end-wall. In order to get a handle on the relative contribution of each enhancement mechanism, comparisons between partial conducting pin-fins(Figs. 39 (e) and 40(e)) and partial non-con conducting pin-fins (Figs.39 (g) and40 (g)) can be made. Regions not roughened by pin-fins (C,F and G) do not show any difference. The overall recorded heat transfer coefficient falls by around 25% in all regions roughened by pin-fins. The Nusselt numbers recorded in the partial non conducting case represent the heat transfer enhancement on the endwall alone. When the non conducting pin-fins are compared to the smooth case (Figs.39 (a) and 40 (a)), a considerable increase is noticed ($\approx 100\%$).

In actual turbine blade applications, pin-fins used are made of low conductivity stainless steel, and their efficiency will deviate from unity more significantly than the copper pin-fins. Actual heat transfer enhancement will therefore lie between the non-conducting pin-fin case and the conducting pin-fin case.

3.   Effect of Rotation

Smooth channels. For low inlet Reynolds numbers, comparing Fig. 39(a) and (b), regions A and B (leading inner and mid-span regions) show a significantly lower heat transfer coefficient than regions D and E (corresponding trailing regions). This difference is less pronounced at higher Reynolds Numbers. (Fig.40). Heat transfer coefficients recorded for regions C and E (corresponding to the outer walls) do not

show a sensitivity to rotation. These observations are further corroborated in Fig. 42, which shows heat transfer enhancements as a function of rotation number for two different streamwise regions. For certain rotation numbers, a heat transfer deterioration can be noted for regions A and B. Heat transfer coefficients corresponding to the side wall (region G) are found to increase with rotation number.

A counter-rotating pair of vortices is set up in the flow-field due to the Coriolis force, as depicted schematically in Fig.37. This results in the vortices "thinning" the boundary layer on the trailing region, thereby increasing heat transfer. In the current configuration, in the absence of obstruction due to pin-fins, the side-wall (region G) experiences an increase in Nusselt number due to rotation. In regions proximate to the slot the high velocity of the coolant is less susceptible to the effect of the Coriolis force.

Full conducting pin-fins. Several differences are observed on comparing the effect of rotation on a smooth surface (Fig.42) to that on a full copper pin-fin roughened surface (Fig.43). By installing pin-fins in the test section, a significant resistance to the aforementioned counter-rotating vortex system is created. The effects of rotation are significantly more subdued due to the full copper pin-fins. The deterioration in heat transfer on the leading surfaces at higher rotation numbers encountered for the smooth channel is absent in the mid-span (B) region, and is significantly reduced in the inner wall (A) region. The increase in heat transfer on the trailing surface is also diminished. A surprising difference between the smooth and full copper pin-fin case is the reversal in trend for side-wall G. G now begins to show a deterioration in heat transfer coefficient due to rotation, and this can be attributed to a re-arrangement of the secondary flow configuration, as is shown in the legend pertaining to Fig.43.

Partial pin-fins. For the stationary channel cases, the partial conducting pin-fins case reported a Nusselt number intermediate between the smooth and the full pin-
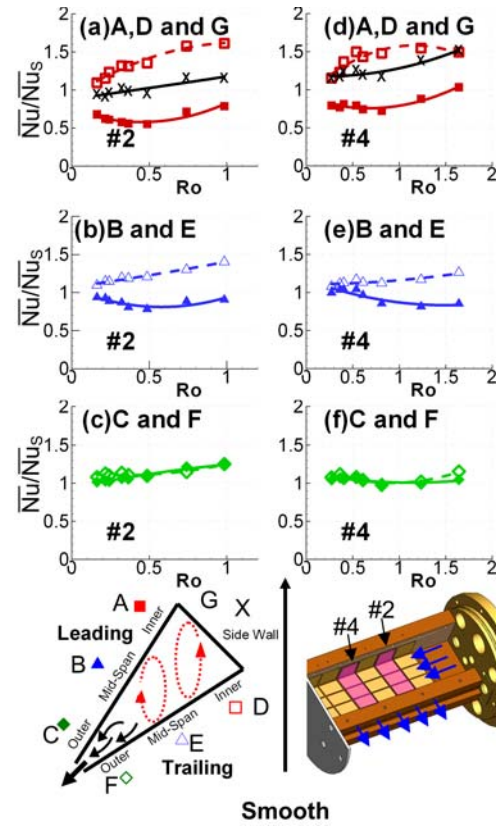
Fig. 42. Effect of local rotation number on local Nusselt number distributions for smooth channel for two different regions (#2 and #4).
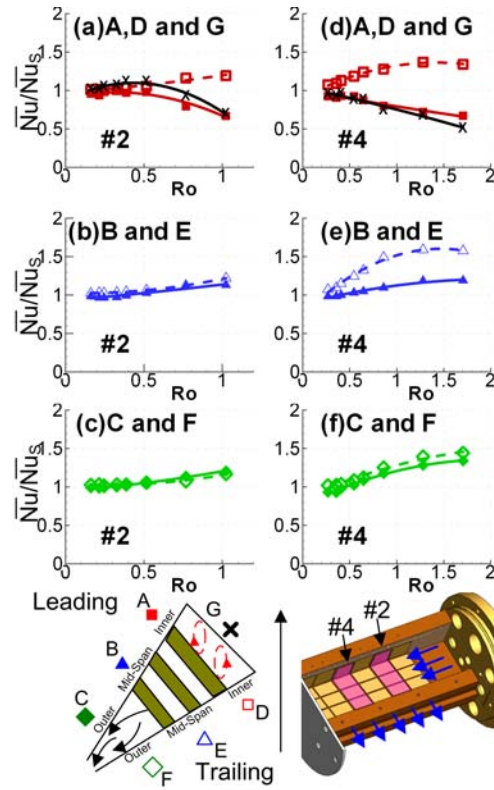
Fig. 43. Effect of local rotation number on local Nusselt number distributions for full-conductive pin-fin roughened channel for two different regions (#2 and #4).
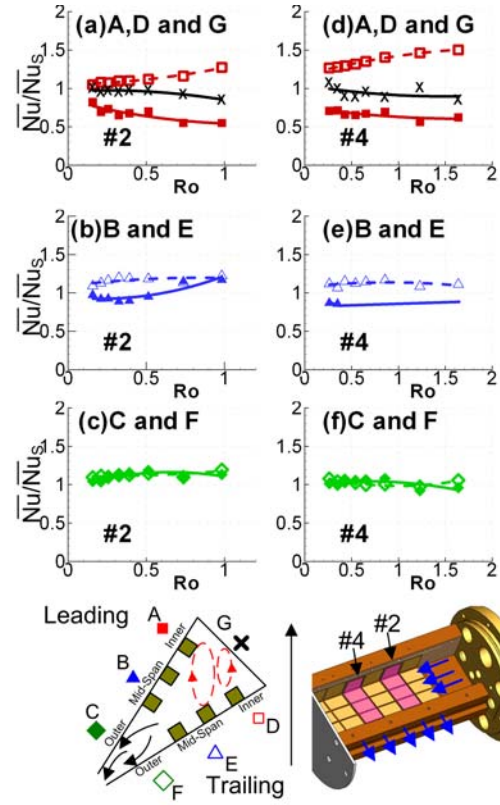
Fig. 44. Effect of local rotation number on local Nusselt number distributions for partial-conductive pin-fin roughened channel for two different regions (#2 and #4).
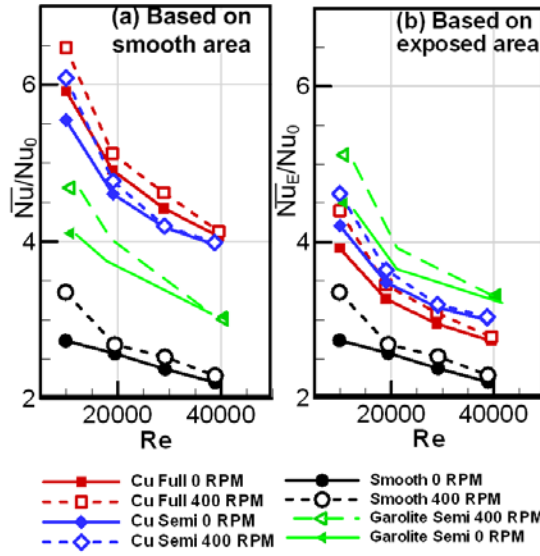
Fig. 45. Effect of Reynolds number on channel averaged normalized Nusselt number. Channel average includes both leading and trailing surfaces.

finned cases. The effect of rotation also follows a similar trend. For the partial pin-fins, observations (Fig.44) indicate a more subdued effect of rotation than in the smooth channel, but a more pronounced effect than in the full pin-finned case. Deterioration in heat transfer coefficient due to rotation is observed in both A (inner wall)and B (mid-span). Region G, the side wall shows a mild deterioration at increasing Ro, intermediate between the larger deterioration of the full pin-fin case and the appreciation in the smooth case. This seems to indicate that some level of disturbance to the counter-rotating vortex system is offered by the partial pin fins - though not as significant as the full pin-fins.

4. Overall Trends

Figure 45(a) shows the dependence of measured heat transfer coefficients (based on the copper-plate area, as defined in Eq.4.3) on the Reynolds numbers, for the various

rotational speeds tested. Thus defined, the heat transfer coefficient is a metric of the rate of heat extracted from the channel by the fluid, regardless of the area enhancement due to the roughness elements. The Nusselt Number is Normalized with Nu_0, which corresponds to the Dittus-Boelter equation for a rectangular duct.

$$Nu_0 = 0.023Re^{0.8}Pr^{0.4} \tag{4.7}$$

The Reynolds number used in the above is the inlet Reynolds number, and not the local Reynolds number. The corresponding average Nusselt numbers include regions A through F, and exclude region G. This is done since G corresponds to the inner wall of the turbine blade; a wall which is shared with another internal cooling passage and not exposed to the hot mainstream flow.

It is observed that the normalized Nusselt numbers fall on increasing the Reynolds number for all cases. Clearly, the full copper pin-fins offer the best performance, followed closely by the partial copper pin-fins.

Increasing the rotational speed has a larger effect at a lower Reynolds number, since a lower value of Re corresponds with a higher Ro. The rotational speed has a monotonic relationship with the overall heat transfer coefficient. This is because the enhancement in heat transfer on the trailing surface is more than deterioration in heat transfer on the leading surface. This implies that rotation has positive impact on the trailing edge cooling channel heat transfer.

Figure 45(b) plots the measured Nusselt number (Nu_E), which is based on the total exposed area. This is the "true" heat transfer coefficient. For the copper pin-fin cases, this incudes the exposed areas of the pin-fins and the copper plates. For the garolite cases, it includes the exposed area of the copper plates only - and does not include the area of the copper plates under the pin-fins.

Using the "true" heat transfer coefficient as a metric, it is noticed that almost all
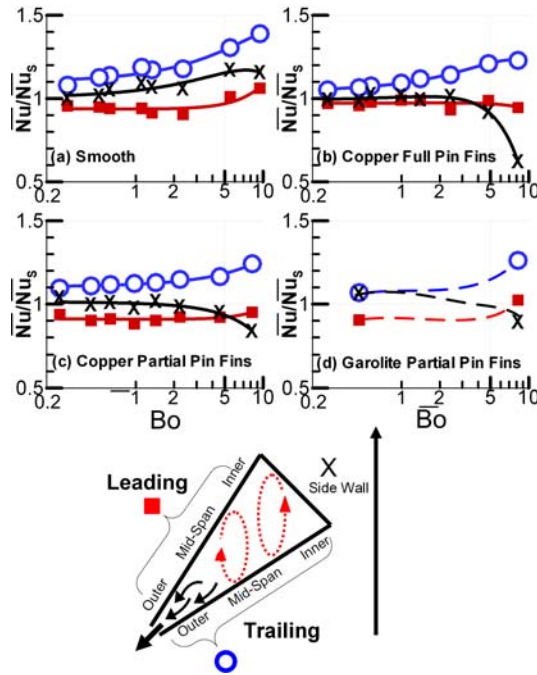
Fig. 46. Effect of buoyancy parameter nusselt number enhancement, on leading, trailing surfaces and side-wall.

the curves for the roughened cases collapse together, to a value much higher than the smooth channel case. This indicates the positive effect of pin-fin inducted turbulence in the flow-field. The garolite pin-fin case, however, reports a slightly higher value than the other roughened cases, because fails to act as a perfect insulator, and some finite heat transfer occurs through the garolite pin-fins.

A more relevant summary of the data in the current work is presented in Fig.46. The Buoyancy parameter has been used in literature to absorb the rotation number and the density ratio effects into a single non dimensional parameter. This figure plots the Nusselt number enhancement due to rotation (Nu/Nu_s) for the leading surfaces (average of A,B and C), trailing surfaces (average of D,E and F) and side wall (G) against the mean buoyancy number (Eq.4.6) encountered in the test section.

The overall trends for the effect of the buoyancy parameter follow the trends discussed for Regions #2 and #4 for effect of the rotation number. Figure 46 also shows that the effect of rotation on the partial garolite pin-fins - which seems identical to the partial copper pin-fin case.

F.   Conclusions

The heat-transfer performance of a pin-fin roughened duct under rotating conditions has been studied at realistic engine Rotation and Buoyancy numbers. Various trends regarding the Nusselt number based on smooth (projected) area of the duct have been discerned:

1. **Effect of trailing edge ejection.** Heat transfer coefficients in the regions proximate to the ejection slot in the narrow region of the wedge are measured to be higher. This is due to the higher velocities associated with the converging geometry. Heat transfer coefficients on the inner wall (opposite to the trailing edge slot) are seen to reduce due to ejection.

2. **Effect of pin-fins.** Pins fins increase heat transfer coefficients by increasing area available for heat exchange as well as increasing the heat transfer on the endwall by creating turbulence in the flowfield.

3. **Effect of rotation on smooth channels.** Increasing the rotation number creates counter-rotating vortices in the flow field, which results in a decrease in the heat transfer on the leading surfaces which are not near the ejection slot. Heat transfer coefficients on the trailing surfaces away from the ejection slot show an increase in the heat transfer coefficient. Regions proximate to the slot show a greater resistance to the effect of rotation due due to higher local velocities.

4. **Effect of rotation on channels with pin-fins.** Pin-fins provide resistance in the flow-field to the Coriolis force induced counter-rotating vortices. Pins fins spanning the entire height of the channel provide a more resistance to this than partial pin-fins. Pin-fins also force a re-arrangement in the secondary flows resulting in a reduction in heat transfer on the inner side wall.

5. **Overall rotation effect.** For all tested (smooth and pin-fin roughened) wedge shape geometries with slot ejection, rotation increases the averaged internal heat transfer coefficients due to the interaction of pin-fin-induced vortical structures and the rotation-induced vortices.

CHAPTER V

FILM COOLING EFFECTIVENESS MEASUREMENT:

EXPERIMENTAL STUDY*

Film cooling involves ejecting a relatively cool (and therefore, dense) jet onto the surface of the turbine blade, so as to form an insulating film between the blade and the hot mainstream. These jets are inclined at an angle to the mainstream, and are also further deflected by the mainstream. The fluid dynamics of film cooling involve an inclined jet in crossflow - a configuration very difficult to quantify. Measurements and simulations indicate the formation of a counter-rotating pair of vortices in the film cooling jet, which entrap the mainstream inside the film.

A.   Two Layer Model for Film Cooling Effectiveness

The two layer model (Fig.47) to analyze film cooling effectiveness stipulates that the cooling air exiting the film cooling holes forms an insulating layer of temperature T_f on the surface of the blade. The heat transfer between the layer and the blade surface is given by Eq.5.2. These parameters (η and h) are convenient to measure in scaled down laboratory tests.

For a surface without film cooling, the heat load is

$$q_o'' = h_o(T_\infty - T_w) \tag{5.1}$$
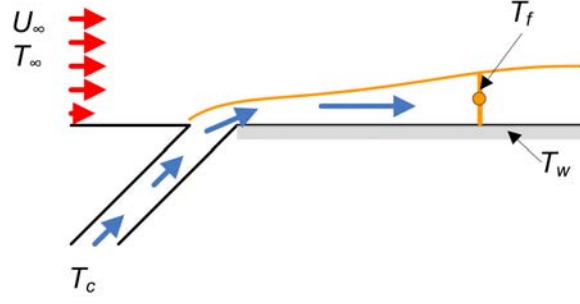
Fig. 47. Film cooling two layer model - schematic.

For a surface cooled by a film, injected at temperature T_c

$$q'' = h(T_f - T_w) \tag{5.2}$$

The temperature T_f dilutes progressively, downstream of the hole because the film interacts with the turbulent mainstream. The film cooling effectiveness is a non dimensional version of T_f.

$$\eta = \frac{T_\infty - T_f}{T_\infty - T_c} \tag{5.3}$$

If blade materials with very low conductivity can be used, then the wall temperature, T_{aw} can be used as a proxy for the film temperature, T_f. The resulting effectiveness is called 'adiabatic' effectiveness - and is identical to the film cooling effectiveness. These quantities can be combined to yield the heat flux reduction, the figure of merit relevant to the engine designer. The benefit of film cooling is realized only of this parameter is below 1.0.

$$\frac{q''}{q''_o} = \frac{h}{h_o} \left(1 - \eta \frac{T_\infty - T_c}{T_\infty - T_w} \right) \tag{5.4}$$

An alternative approach to assessing the performance of film cooling is the superposition approach, where heat transfer coefficients for the case *with* film cooling are
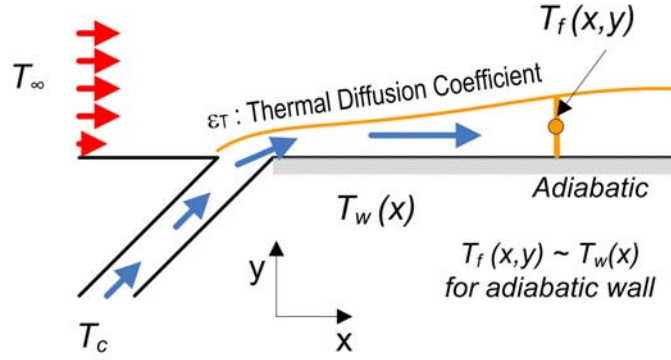
(a) Thermal boundary conditions
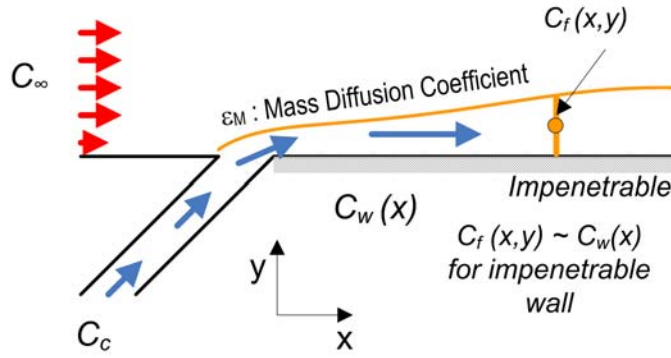
(b) Mass transfer boundary conditions

Fig. 48. Measurement of film cooling effectiveness using the heat/mass transfer analogy. Here, the y is the boundary-layer direction and x is the streamwise direction. The film temperature/concentration is a function of x,y, while wall temperatures/concentrations are functions of x only.

calculated using the mainstream temperature as a reference rather than the film temperature. (defined by Eq.5.1, by measuring T_∞, T_w and q_o''). Results computed using this approach are conventionally presented using a parameter called Stanton Number Reduction (SNR).

$$SNR = 1 - \frac{St_{film}}{St_{no-film}} \qquad (5.5)$$

Both approaches are conceptually equivalent.

A detailed discussion of these models is available in [61], [62], [63]. The focus of this review paper is on the film cooling effectiveness only.

B. Measurement Theory

1. Mass Transfer Analogy for Film Cooling Effectiveness

Consider the configuration shown in Fig.48(a), where a protective coolant (at T_c) is injected into a hot mainstream (at T_∞).

Governing equations for heat transfer in a two-dimensional turbulent boundary layer (in x-y co-ordinates) for a homogeneous fluid are ([22]):

$$G_x \frac{\partial T}{\partial x} + G_y \frac{\partial T}{\partial y} = \rho(\epsilon_T + \alpha) \frac{\partial^2 T}{\partial y^2} \tag{5.6}$$

Here, ϵ_T is the turbulent thermal diffusivity. The adiabatic wall boundary condition (based on Fig. 48(a)) is:

$$y = 0 : \frac{\partial T}{\partial y} = 0, T = T_{aw} \tag{5.7}$$

The mainstream temperature beyond the film is:

$$y > \delta_f : T = T_\infty \tag{5.8}$$

The temperature of the injected coolant:

$$x = 0 : T = T_C \tag{5.9}$$

Consider an analogous case, where the 'hot' mainstream has a tracer element/gas concentration of C_∞, and the coolant gas discharged through the film cooling holes has a tracer concentration of C_C, as detailed in Fig.48(b).

Corresponding governing equations for mass transfer (with C being the mass fraction either a tracer element or a component gas) are:

$$G_x \frac{\partial C}{\partial x} + G_y \frac{\partial C}{\partial y} = \rho(\epsilon_M + D)\frac{\partial^2 C}{\partial y^2} \tag{5.10}$$

Here, ϵ_M is the turbulent mass diffusivity. The impenetrable wall boundary condition (based on Fig. 48(b)) is:

$$y = 0 : \frac{\partial C}{\partial y} = 0, C = C_w \tag{5.11}$$

The corresponding concentrations of the tracer/foreign gas in the mainstream and coolant are given by:

$$y > \delta_f : C = C_\infty \tag{5.12}$$

$$x = 0 : C = C_C \tag{5.13}$$

Equations 5.7 and 5.11 reflect the analogous adiabatic wall and impenetrable wall conditions respectively. It can be noticed that Equations 5.6 and 5.10 and their boundary conditions have a similar structure. In the event that the turbulent Lewis number, $Le_T = \frac{(\epsilon_T + \alpha)}{(\epsilon_M + D)} = 1$, it is evident from the governing equations and boundary conditions that appropriately non dimensionalized solutions (temperatures or mass concentrations) will be identical.

Based on the work of [64] and [22], the stipulation $Le_T \approx 1$ holds for turbulent gaseous flow fields, such as those encountered in gas turbine engines. And therefore:

$$\eta = \frac{T_f - T_\infty}{T_C - T_\infty} \approx \frac{T_{aw} - T_\infty}{T_C - T_\infty} \approx \frac{C_w - C_\infty}{C_C - C_\infty} \tag{5.14}$$

The underlying assumption governing the heat/mass transfer analogy ($Le_T \approx 1$)
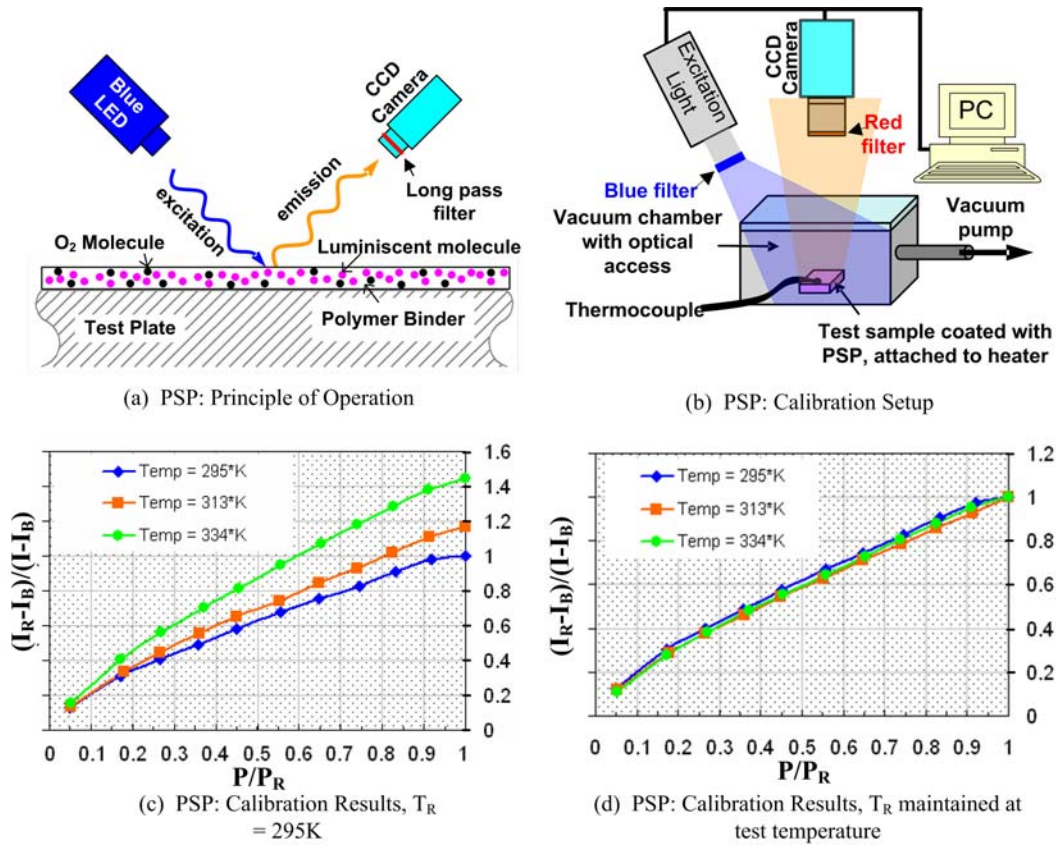
Fig. 49. PSP working principle, calibration.

requires that the flow-field be highly turbulent. This assumption is usually valid over the surface of the gas turbine vane/blade/end-wall due to the high Reynolds numbers involved as well as various secondary mechanisms further inducing turbulence in the flow-field (such as leakage vortices, horse-shoe vortices, film cooling jets and periodic rotor/stator wakes). However, measurements have shown that the flow proximate to the leading edge portion of the blade is usually either laminar or intermittent, even with film cooling. This invalidates the governing assumption in the leading edge region, and more investigation is required to quantify this effect.

2. Pressure Measurement Using Pressure Sensitive Paints

Pressure sensitive paints (such as the UniFIB, composed of a blend of Fluoro Isopropyl Butyl polymer (FIB), Platinum tetra (pentafluorophyenyl) porphine (PtTFPP), and a white pigment) can be used to measure external pressure on a painted surface. When excited by a light in the blue region of the spectrum (around 400nm, usually thorough a LED array), the paint emits a light in the red region (>600nm). The excited electrons of the PSP emit a photon in the red range of the spectrum to fall back to their degenerate state. Another radiation-free path to the degenerate state is due to interaction with Oxygen molecules. This is known as *oxygen quenching*. The intensity of the emitted light reduces with an increase in concentration (i.e. partial pressure) of oxygen adjacent to the PSP layer (Fig.49(a),(b)).

The emitted light is recorded by a scientific grade CCD camera equipped with a red-filter (to ensure none of the exciting blue light is captured). The intensity of the emitted light (after correction for background noise) is related to the partial pressure of oxygen surrounding the painted surface using the Stern-Volmer equation. [65]

$$\frac{I_R - I_B}{I - I_B} = A(T) + B(T)\frac{P_{O_2}}{P_{O_2,R}} \tag{5.15}$$

Here, I_R is a 'reference' intensity, typically corresponding with images acquired at atmospheric conditions. The corresponding (atmospheric) pressure is given by P_R, and the atmospheric oxygen partial pressure is given by $P_{O_2,R}$. I_B is the 'black' intensity - the background noise of the CCD camera, which corresponds with images acquired in a dark room. I corresponds with intensities acquired at the calibration pressure/temperature. $A(T)$ and $B(T)$ are the Stern-Volmer constants. E_{nr} is the Arrhenius activation energy for the non-radiative process; E_p is the activation energy for oxygen diffusion. R is the universal gas constant.

$$A(T) = A(T_R) \left(1 + \frac{E_{nr}}{RT_R} \left(\frac{T - T_R}{T_R} \right) \right) \tag{5.16}$$

$$B(T) = B(T_R) \left(1 + \frac{E_p}{RT_R} \left(\frac{T - T_R}{T_R} \right) \right) \tag{5.17}$$

The emitted light intensity by the pressure sensitive paint depends on both, the partial pressure of oxygen as well as the temperature of the surface. Therefore, a calibration can be performed (typically inside a vacuum chamber with optical access) to quantify the pressure and temperature sensitivity of the paint. (Fig.49(c)). Further, ensuring that the reference temperature is identical to the tested temperature allows the curves to collapse together, compensating for the temperature effect (Fig.49(d)).

Rather than evaluate the Stern-Volmer coefficients, it is often more convenient to compute a polynomial curve fit for the data. For example, at dataset such as Fig.49(d) can be correlated by the following equation:

$$
\begin{aligned}
\frac{P_{O_2}}{P_{O_2,R}} \;=\; & 0.0059 + 0.3961 \left(\frac{I_R(T) - I_B}{I(T) - I_B} \right) + \\
& 0.9034 \left(\frac{I_R(T) - I_B}{I(T) - I_B} \right)^2 - 0.3002 \left(\frac{I_R(T) - I_B}{I(T) - I_B} \right)^3
\end{aligned}
\tag{5.18}
$$

Eq.5.18 relates the partial pressure of oxygen to the recorded intensities. Since the molar concentration of oxygen in air is constant at 21%, the parital pressure ratio $\frac{P_{O_2}}{P_{O_2,R}}$ is identical to $\frac{P}{P_R}$. So, based on the above equation (Eq.5.18), one can convert recorded intensities to pressures inside a wind tunnel. However, if a foreign gas is introduced into the wind tunnel, the molar composition of the mixture changes - and the oxygen partial pressure is no longer in constant proportion to the pressure inside the wind tunnel. This property is utilized in determining the film cooling effectiveness using PSP mass transfer analogy.
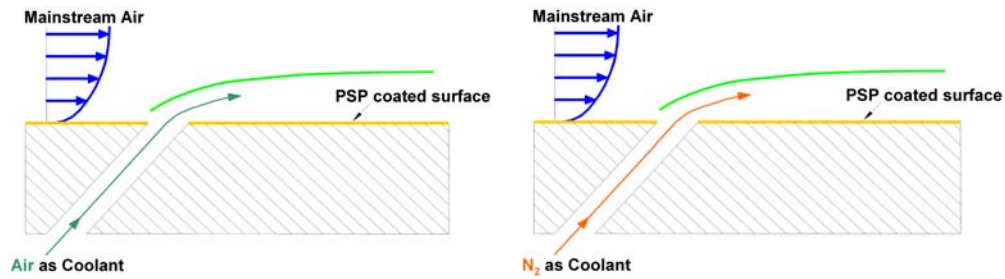
(a) Test with air used as coolant

(b) Test with foreign gas (here, nitrogen) used as coolant
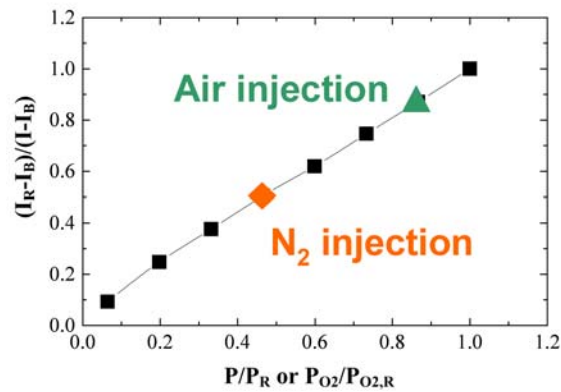
(c) Typical intesities recorded with air and nitrogen injection

Fig. 50. Measurement of film cooling effectiveness using the PSP analogy method.

3. The PSP Mass Transfer Analogy to Determine Film Cooling Effectiveness

The PSP method to determine film cooling effectiveness is fairly insensitive to the material of the base plate. Any rigid (non-deforming) material impervious to oxygen will suffice. The pressure sensitive paint is applied to the region of interest, which typically includes the region around and up to 30-40 diameters downstream of the film cooling holes. In the case of full-coverage film cooling, the entire blade surface can be coated with the PSP. A base layer of black acrylic paint is applied to the surface before the PSP is sprayed. The PSP is carefully sprayed using an airbrush. Care is taken to ensure that the PSP is sprayed uniformly - and that the layers are

amply thick. Over-spraying might result in thick layers of the paint peeling off from the surface.

Various foreign gases are injected through the film cooling holes to simulate the coolant-to mainstream density ratio effect. The foreign gas reduces the local concentration of oxygen near the wall in regions of finite film cooling effectiveness. The PSP senses this change in concentration. A relation between the local defect in oxygen concentration and film cooling effectiveness can be arrived at.

To determine film cooling effectiveness for a given configuration, four tests are required. In each test, several images are captured and averaged to reduce random noise. Test 1 involves switching off the excitation LED light and capturing an image in a dark room to determine the background noise intensity. The corresponding intensity field is called I_B. Test 2 involves turning on the excitation light, focusing the camera on the region of interest and acquiring a set of images without turning on the mainstream (I_R). Test 3 (Fig.50(a)) involves establishing mainstream and coolant flow rates at the appropriate blowing ratio using air as a coolant and acquiring a set of images, (I_{air}). The resulting oxygen partial pressure and concentration fields are $P_{O_2,air}$ and $C_{O_2,air}$. Finally, test 4 (Fig.50(b)) is conducted, establishing the desired blowing ratio using the foreign gas as a coolant (nitrogen injection shown in Fig.50(b))), with the averaged intensity recorded as I_{fg}. Corresponding oxygen partial pressure and concentration fields are $P_{O_2,fg}$ and $C_{O_2,fg}$.

The expression in Eq. 5.14, based on the foreign-gas mass transfer analogy relates the mass fractions of oxygen with film cooling effectiveness. An equivalent expression based on partial pressures of oxygen is sought in order to allow the application of the PSP based mass-transfer analogy.

For the air injection case, (Test 3), $C_{O_2,air}(=C_{O_2,\infty})$ is a constant value, since air is composed of 21% O_2 by volume. Injecting foreign gas (nitrogen injection shown in

Fig.50(b))) through film cooling holes (Test 4), reduces the local mass concentration of oxygen inside the film ($C_{O_2,fg}$), resulting in a higher emitted intensity (Fig.50(c)). Also, in the test where foreign gas is injected, $C_{O_2,C} = 0$. Eq.5.14 becomes:

$$\eta \approx \frac{C_w - C_\infty}{C_C - C_\infty} = \frac{C_{O_2,fg} - C_{O_2,air}}{C_{O_2,C} - C_{O_2,air}} = 1 - \frac{C_{O_2,fg}}{C_{O_2,air}} \tag{5.19}$$

In the special case where the molecular weight of the foreign gas is similar to that of air (e.g. nitrogen injection), the mass fraction ratio equals the mole fraction ratio, which in turn equals the partial pressure ratio. This yields:

$$\eta \approx 1 - \frac{C_{O_2,fg}}{C_{O_2,air}} = 1 - \frac{P_{O_2,fg}}{P_{O_2,air}} = 1 - \frac{P_{O_2,fg}/P_{O_2,R}}{P_{O_2,air}/P_{O_2,R}} \tag{5.20}$$

Eq. 5.20 can be used to estimate the film cooling effectiveness when nitrogen is injected through the film cooling holes, converting the intensities recorded in tests 1 through 4 to partial pressures of oxygen using Eq.5.18 (Fig.50(c)). Several papers have been published using this methodology. (e.g. [66], [67], [68]). When a coolant with a different density is injected through the film cooling holes (to simulate realistic density ratios), the above equation needs to be modified.

In the following equations, the mole fraction is given by X. $X_{O_2,air}$ represents the mole fraction of oxygen in air. The values of $X_{O_2,air}$ and $C_{O_2,air}$ are constant for air, regardless of absolute pressure and temperature. However, when a foreign gas (e.g. Nitrogen, Carbon Dioxide or Argon) is injected through the film cooling holes, a local variation in these values occurs inside the film. In this case, the local oxygen molar and mass concentrations are respectively, $X_{O_2,fg}$ and $C_{O_2,fg}$. Also in the foreign gas injection case, the chemical composition of the film changes the effective local molecular weight. The local effective molecular weight of the film is $W_{mix,fg}$. For the air injection case, the fluid has a constant molecular weight throughout of

W_{air}.

Starting from Eq.5.19,

$$\begin{aligned} \eta = 1 - \frac{C_{O_2,fg}}{C_{O_2,air}} &= 1 - \frac{X_{O_2,fg}(W_{O_2}/W_{mix,fg})}{X_{O_2,air}(W_{O_2}/W_{air})} \\ &= 1 - \frac{X_{O_2,fg}W_{air}}{X_{O_2,air}W_{mix,fg}} \end{aligned} \qquad (5.21)$$

The unknown molecular weight of the air-coolant mixture inside the film, $W_{mix,fg}$ can be related to the molecular weights of the component gases using by their mole fractions:

$$\begin{aligned} W_{mix,fg} &= X_{O_2,fg}W_{O_2} + X_{N_2,fg}W_{N_2} + X_{fg,fg}W_{fg} \\ &= X_{air,fg}W_{air} + X_{fg,fg}W_{fg} \end{aligned} \qquad (5.22)$$

because the effective molecular weight of air, W_{air} is defined to be:

$$X_{O_2}W_{O_2} + X_{N_2}W_{N_2} = X_{air}W_{air} \qquad (5.23)$$

Oxygen constitutes 21% of atmospheric air by volume (and hence by mole). So, $X_{air,fg} = 4.76X_{O_2,fg}$.

Since all mole fractions must add up to unity,

$$\begin{aligned} X_{O_2,fg} + X_{N_2,fg} + X_{fg,fg} &= X_{air,fg} + X_{fg,fg} \\ = 4.76X_{O_2,fg} + X_{fg,fg} &= 1 \end{aligned} \qquad (5.24)$$

Solving for the unknown $W_{mix,fg}$ in terms of the mole fractions of oxygen, Eq 5.22 becomes:

$$W_{mix,fg} = 4.76X_{O_2,fg}W_{air} + (1 - 4.76X_{O_2,fg})W_{fg} \tag{5.25}$$

Substituting for $W_{mix,fg}$ in Eq.5.21 and, solving for η in terms of only one unknown

$$
\begin{aligned}
\eta &= 1 - \frac{X_{O_2,fg}W_{air}}{X_{O_2,air}(4.76X_{O_2,fg}W_{air} + (1 - 4.76X_{O_2,fg})W_{fg})} \\
&= 1 - \frac{1}{(4.76X_{O_2,air} + (\frac{X_{O_2,air}}{X_{O_2,fg}} - 4.76X_{O_2,air})\frac{W_{fg}}{W_{air}})}
\end{aligned} \tag{5.26}
$$

Noting that $4.76X_{O_2,air} = X_{air,air} = 1$ and that the ratio of partial pressure of a constituent chemical to the static pressure is identical to the mole fraction of the component (i.e. $X_{O_2,fg} = \frac{P_{O_2,fg}}{P}$ where P is the static pressure).

$$
\begin{aligned}
\eta &= 1 - \frac{1}{(1 + (\frac{X_{O_2,air}}{X_{O_2,fg}} - 1)\frac{W_{fg}}{W_{air}})} \\
&= 1 - \frac{1}{(1 + (\frac{P_{O_2,air}/P_{O_2,R}}{P_{O_2,fg}/P_{O_2,R}} - 1)\frac{W_{fg}}{W_{air}})}
\end{aligned} \tag{5.27}
$$

In the above equation (Eq.5.27), $P_{O_2,air}/P_{O_2,R}$ and $P_{O_2,fg}/P_{O_2,R}$ correspond with pressures calculated from the intensity fields measured by test 3 and test 4 respectively. This expression (Eq.5.27) was originally derived by [69], and has been used by [70] and [71]. In the case $W_{fg}/W_{air} = 1$, Eq.5.27 reduces to Eq.5.20.

C.   Flat Plate Film Cooling Effectiveness Measurements

1.   Literature Survey

Effect of blowing and density ratios. Several studies have been performed characterizing the effect of coolant blowing ratio ($M = \frac{\rho_c V_c}{\rho_M V_M}$) and mainstream turbulence

intensity (Tu) on the film cooling effectiveness and heat transfer coefficient. Sinha et al. [72] studied the effect blowing ratio and density ratio ($DR = \frac{\rho_c}{\rho_M}$) on film cooling effectiveness using a plate with simple angled holes. At lower blowing ratios, the film coolant was found to cling to the surface of the plate. On increasing the blowing ratio, the film coolant tended to lift-off from the surface of the blade, owing to larger inertia due to the higher momentum of the coolant. Several studies in the open literature ([73, 74, 75]) draw similar conclusions using different experimental methods. The parametric effects of Blowing and Density ratios are similar on curved surfaces (such as suction and pressure surfaces of blades).

Typical coolant to mainstream density ratios in gas turbine engines range from 2.0 to 3.0. Simulating this density ratio in the laboratory is difficult, since it requires cooling the secondary air to temperatures much lower than the ambient, e.g. [72, 76]. Foreign gases have been used to simulate the effect of density ratio (e.g. [64] and [77]). Data in the literature expositing the effect of density ratio on film cooling effectiveness is fairly scarce, and does not cover a large parameter range. Sinha et al. [72] observed a significant improvement in film cooling effectiveness at higher density ratios due to the suppression of lift-off. They concluded that for lower blowing ratios (before lift-off), using mass flux ratio as a scale was appropriate, however, momentum-flux ratio was more relevant at higher blowing ratios (after lift-off).

Effect of hole shape, angle and configuration. The process of film cooling is found to be very sensitive to a variety of parameters. The angle that the axis of the hole makes with the blade surface has a significant effect on the film cooling effectiveness. Film cooling holes inclined along the mainstream direction (simple angled holes) are found to offer much better protection than holes perpendicular to the blade surface. In addition to being simple angled (inclined along the mainstream direction) , injecting the flow at an angle to the mainstream (using compound angled

holes) is found to further improve the spread the film coolant; as is utilizing holes with an expanded exit area (fan-shaped holes, for instance). These holes are found to reduce the shear mixing between the coolant and the mainstream, thereby improving the effectiveness of film cooling. [78]. A comprehensive literature review of shaped hole film cooling can be found in Bunker [79].

More recently, embedding film cooling holes in trenches has been attempted. [80, 81, 82]. Utilization of trenches has been found to increase the film cooling effectiveness considerably, albeit at the price of increasing the heat transfer coefficient by tripping the flow. Another attempt at increasing film cooling effectiveness has been made by Na and Shih [83] who introduced a ramp with a backward facing step upstream of the hole. Their computations indicated an enhancement of film cooling effectiveness in the region near the hole owing to the entrapment of the coolant in the recirculation zone formed immediately downstream of the step. Barigozzi et al. [84] experimentally verified the same and also measured the corresponding aerodynamic losses. The step in their study was placed 0.5d upstream of the hole and was roughly 0.5d in height.

Experimental methods. Several experimental techniques have been used in the literature to determine film cooling effectiveness. Researchers have found it challenging to reconcile measurements made using thermal (IR and thermocouple) measurements with mass transfer analogy measurements. For almost-identical conditions, the thermal methods show a much higher film cooling effectiveness than corresponding mass-transfer analogy methods. This issue has been discussed in some detail by Nicoll and Whitelaw [85] Goldstein and Jin [74] as well as Wright et al. [75]. When comparing film cooling effectiveness measured by the naphthalene sublimation mass transfer analogy [74] and the transient liquid crystal methodology [73] on a flat plate, Goldstein [74] finds a consistent 10-20% lower bias in the mass-transfer analogy data. A similar conclusion was arrived at by Wright et al. [75] using the Pressure Sensitive

Paint (PSP) mass transfer analogy. The difference in measured values of effectiveness between thermal and mass transfer methods can possibly be attributed to lateral conduction in the low conductivity substrate plate in regions of high thermal gradients (i.e. regions of high film cooling effectiveness).

The validity of the heat-mass transfer analogy for film cooling effectiveness measurement requires the reasonable approximation that the turbulent Lewis number be equal to unity, based on works by Nicoll and Whitelaw [85] and Jones [64]. Nicoll and Whitelaw used a Helium as a tracer gas and arrived at adiabatic effectiveness using gas chromatography. Goldstein and Jin [74] used the naphtalene sublimation mass transfer analogy technique to estimate film cooling effectiveness. More recently, the PSP analogy has made it possible to present high resolution conduction error free contours of film cooling effectiveness [75, 86, 87]. Rallabandi et al. [88] show that effectiveness data acquired on a flat-plate using PSP is similar to the naphtalene sublimation based data of Goldstein et al. [74].

2.   Objectives

We study the effect of placing a step immediately upstream of several simple and compound angled film cooling holes. We also study parametrically the effect of step width, height and location upstream of the hole. All studies on the step have been performed using the steady state PSP technique.

3.   Experimental Setup

A low speed suction type wind tunnel at a mainstream velocity of 25m/s (with a Turbulence intensity of 0.5%) was used to conduct all the tests. The wind tunnel has a 4:1 entrance contraction ratio in order to produce uniform flow. A 5 m cotton fiber plastic flow straightener box is utilized at the entrance of the wind-tunnel. The test

channel has a cross section of 30.48cm x 15.24cm. A 5.6KW axial blower is used in suction mode to establish the mainstream flow through the channel. The buildings central air conditioning system maintains the room at 22C.

The coolant is supplied either through a compressor (air) or through a pressurized tank (nitrogen). Temperatures in the plenum and in the mainstream have been measured by thermocouples. Pressures in the plenum are measured by an inclined manometer and the mainstream velocity is measured using a Pitot probe connected to a micro-manometer. The coolant loop flow rate is metered using a Dwyer rotameter.

The test section has a plenum which supplies the coolant to the mainstream through the film cooling holes on the plate. The ratio of the area of the plenum to the total area of the all the film cooling holes is of the order 6.

The inner surface of the wind tunnel has a recess above the coolant plenum. A 15mm thick film cooling plate is placed in the recess and caulked such that it is flush with the inner wall of the wind tunnel. It is also ensured that the joint between the plenum and the plate is air tight.

Four such plates are considered. The plate with simple angled cylindrical holes (plate 1) is fabricated using a poly-urethane foam; the compound angle cylindrical hole plate (plate 2) using Plexiglas; the simple angled fan-shaped hole plate (plate 3) using the EDM process on a stainless steel plate; the compound angled fan shaped hole plate (Plate 4) using SLA process on a Somos epoxy photopolymer. Plate material selection is based on availability; not on functionality as the PSP method is not sensitive to the substrate material. Details are shown in Fig.51.

The upstream step is simulated using gasket material with double sided tape used as an adhesive. The combined thicknesses of the gasket material and double sided tape are 0.5mm (12.5%d), 1.0mm (25%d) and 1.5mm (37.5%d).
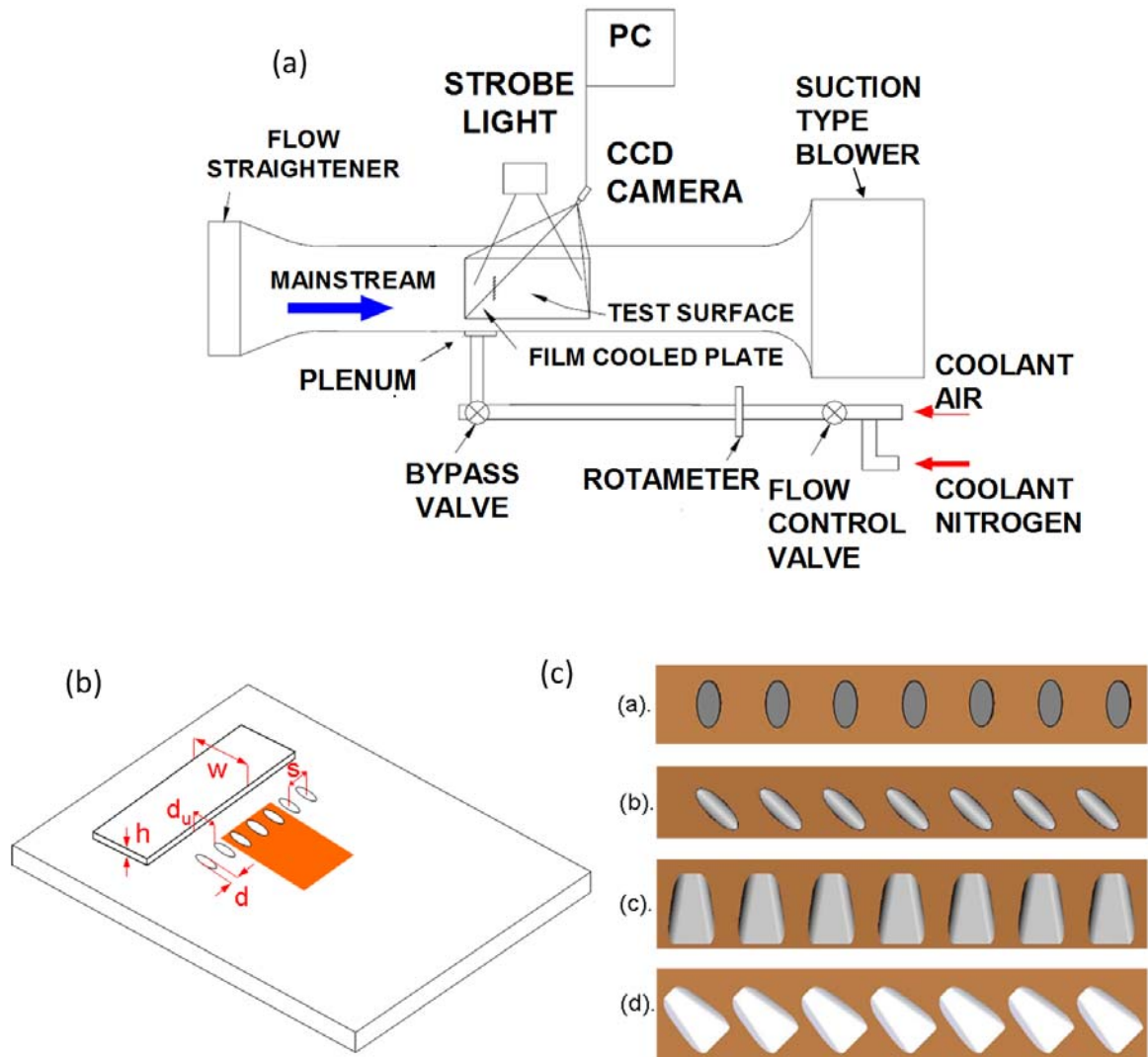
Fig. 51. (a) Test section details (b) Details definitions of various parameters varied (c) Details of various flat plates studied.
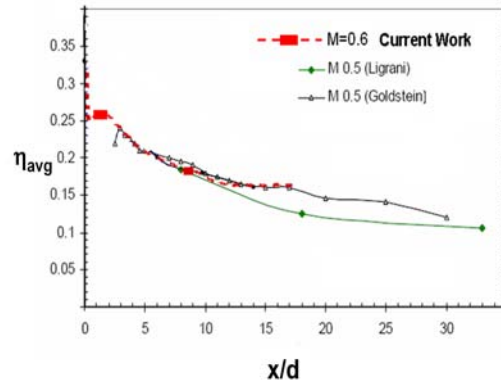
Fig. 52. Comparison of current results with similar tests available in literature. All holes are compound angled and details of each experiment are listed in Table 3.
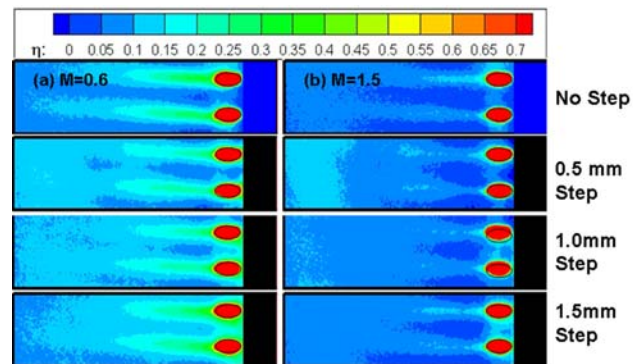
Fig. 53. Effect of upstream step height (h) on cylindrical simple angled holes: (a) M=0.6 (b) M=1.5.
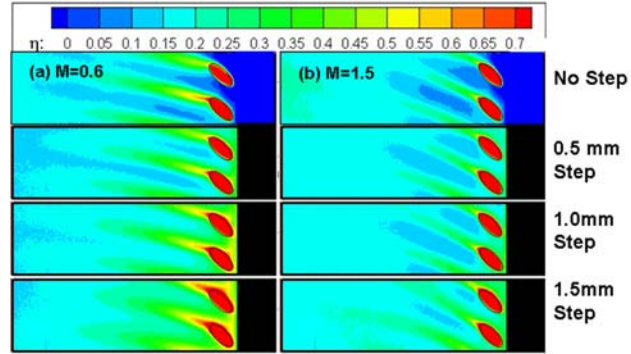
Fig. 54. Effect of upstream step height (h) on cylindrical compound angled holes: (a) M=0.6 (b) M=1.5.
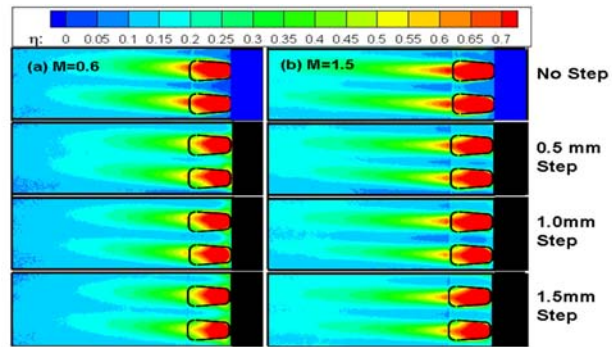
Fig. 55. EEffect of upstream step height (h) on fan shaped simple angled holes: (a) M=0.6 (b) M=1.5.
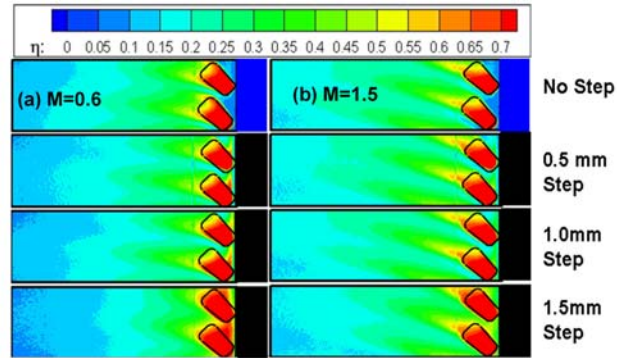
Fig. 56. Effect of upstream step height (h) on fan shaped compound angled holes: (a) M=0.6 (b) M=1.5.
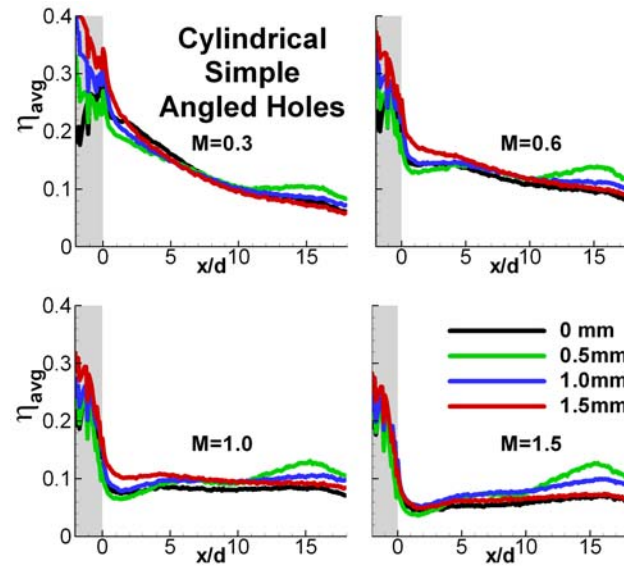
Fig. 57. Cylindrical simple angled holes: span-wise averaged effectiveness showing the effect of step-height h on film cooling effectiveness for four different blowing ratios.
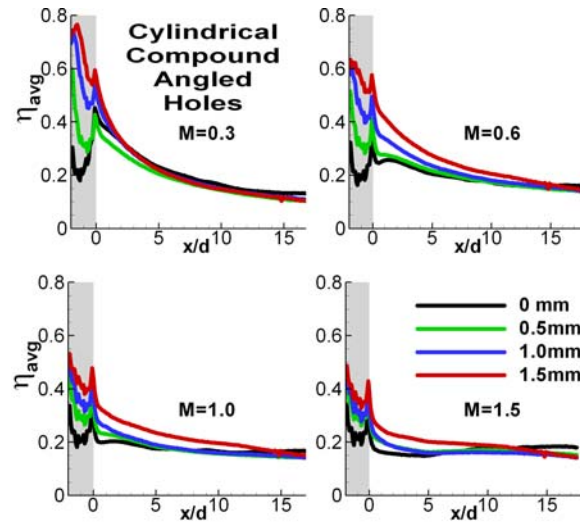
Fig. 58. Cylindrical compound angled holes: span-wise averaged effectiveness showing the effect of step-height h on film cooling effectiveness for four different blowing ratios.
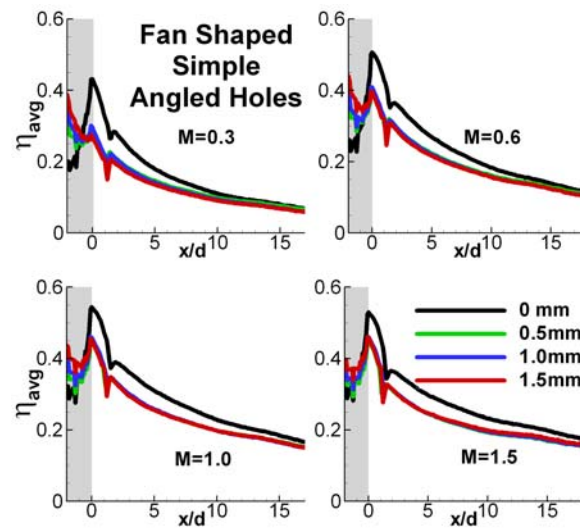
Fig. 59. Fan shaped simple angled holes: span-wise averaged effectiveness showing the effect of step-height h on film cooling effectiveness for four different blowing ratios.
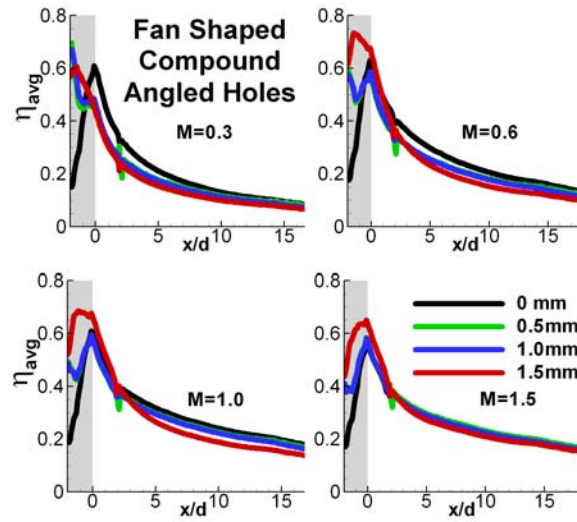
Fig. 60. Fan shaped compound angled holes: span-wise averaged effectiveness showing the effect of step-height h on film cooling effectiveness for four different blowing ratios.
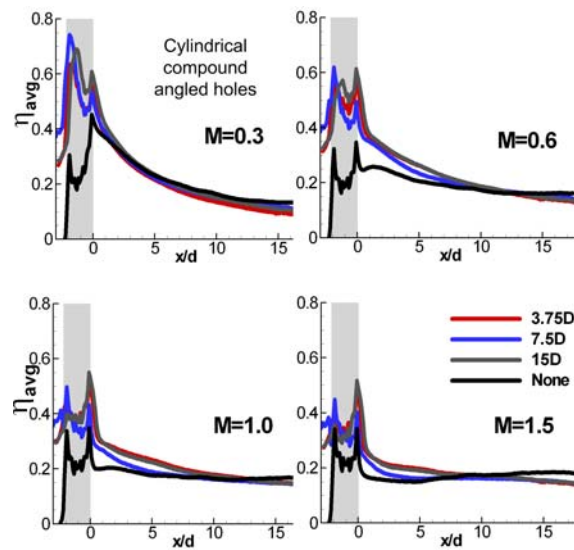
Fig. 61. The effect of step width (w) on the film cooling effectiveness: span-wise averaged plots.
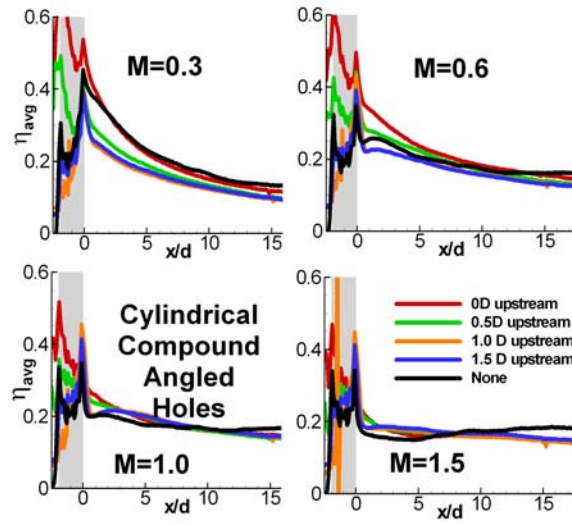
Fig. 62. The effect of step position (du) on the film cooling effectiveness: span-wise averaged plots.
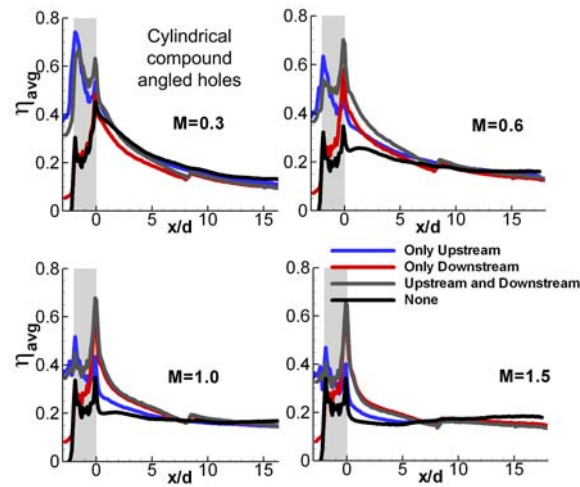
Fig. 63. The effect of downstream step (dd=0) on the film cooling effectiveness: span–wise averaged plots.

111
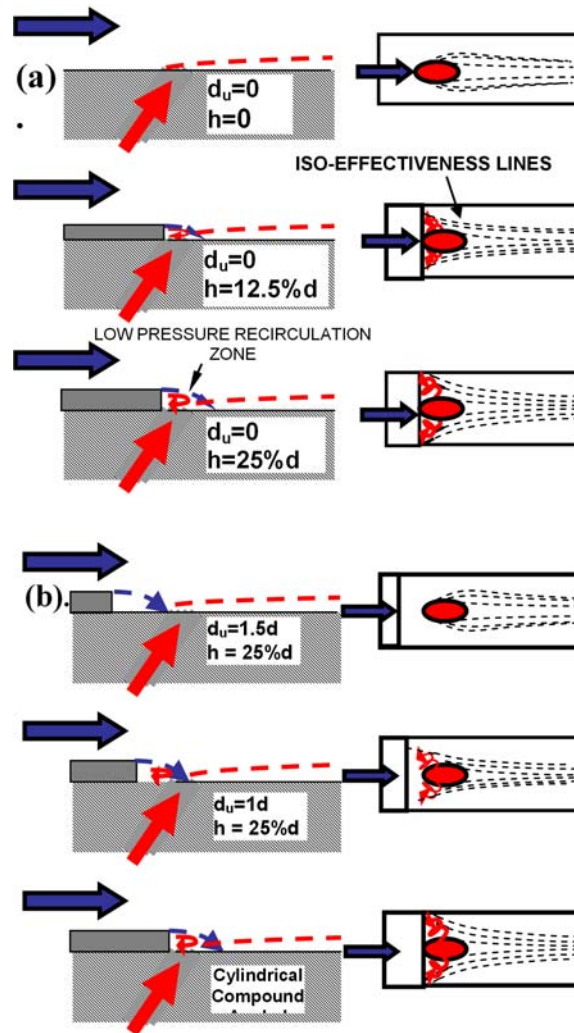
Fig. 64. Schematic of effect of upstream step on film-cooling effectiveness by entrapping coolant in recirculation zone formed immediately downstream of step (a) Effect of step height h (b) Effect of distance of upstream step from leading edge of hole d_u.

4. Results and Discussion

Obtained data has been benchmarked in Fig.52. Figs. 53-63 summarize the results obtained with the upstream step. The contour plots (Figs. 53-56) show only two out of the seven holes on the plates. The span-wise (Figs. 57-63) averages consider the three central holes as detailed in Fig.51. A schematic explanation of the step effect is provided in Fig.64.

The effect of blowing ratio(M) on plates without steps. The effect of coolant blowing ratio on the base-line cylindrical simple angled holes is as expected in literature: an optimum seems to lie around M=0.6 (depending on the value of x/d considered to report effectiveness). The higher blowing ratio jets (M=1.0 onwards) display a tendency to lift off from the surface owing to their own inertia, mixing with the mainstream - thereby resulting in low film cooling effectiveness values.

The compound angled cylindrical holes offer much better coverage in comparison with the simple angled holes. They also demonstrate signs of film cooling lift off at higher blowing ratios, as is expected in literature.

A comparison of current work with published literature has been presented in Fig. 52 for M=0.6 (compound angled). (Since the corresponding M=0.6 data is unavailable, the M=0.5 data is considered). The current data seems to be in excellent comparison with Goldstein et al [74] - a set of tests conducted with a very similar geometry and turbulence intensity using the naphthalene sublimation method, with naphthalene saturated air as the coolant. Since the naphthalene sublimation method is also a mass transfer method, it is not susceptible to conduction error.

Results show that fan-shaped holes improve film cooling effectiveness - especially at higher blowing ratios when compared with cylindrical holes. Since the expansion at the exit of the film cooling holes helps diffuse the flow, the jets have a lower

tendency to lift off from the surface and mix with the mainstream. These advantages are evident in Figs. 55,56,59,60.

Effect of the upstream step. The effect of the step on simple angled holes is most pronounced in the region proximate to the holes - and less pronounced in the regions farther downstream of the holes. As a matter of fact, the curves tend to collapse onto the h=0 (no step) curve for all blowing ratios at greater x/d values. The higher effectiveness at lower (and negative) values of x/d can be attributed to the entrapment of some coolant in the low-pressure recirculation zone immediately downstream of the backward facing step - as is demonstrated by the computations of Na et al. [83].

The height of the upstream step also has a direct impact on the effectiveness at low values of x/d. The higher the step, the greater the effectiveness at lower values of x/d. This could be attributed to the larger recirculation zones forming immediately downstream of the higher steps - and therefore entrapping more coolant. This effect is shown schematically in Fig. 64.

In the compound angled cylindrical hole case, the effect of the upstream step is observed to be much more significant in comparison with the simple angled case. The step is observed to have a significant effect upstream at every blowing ratio. For simple angled fan shaped holes, at lower (negative) values of x/d the effectiveness, on the introduction of the upstream step seems to follow the same trend observed for cylindrical holes.

However, as one considers data downstream (x/d>0), one notices that the upstream step is actually counter-productive. Compound angled fan-shaped holes, on the other hand, do not seem significantly affected by the upstream step (either positively or negatively) at larger values of x/d, though they show a slight increase in effectiveness at lower values of x/d - especially at higher h.

The following parametric studies have been performed on the compound angled cylindrical holes.

Film cooling hole shape. The step seems to improve the diffusion of the jet from the cylindrical film cooling holes. Since the expanded area of the fan-shaped holes already diffuses the film cooling jet - adding the upstream step does not have any additional positive effect. The disturbance caused to the mainstream flow due to the upstream step seems to be counter - productive to the film cooling effectiveness.

Effect of distance of step from upstream edge of film cooling holes (d_u). The distance of the upstream step from the film cooling holes is found to have a very significant effect on the film cooling effectiveness. (Fig.62) When the step is placed at du=1.5d or 1d, it is observed that the effect on effectiveness is minimal - and often, quite detrimental (M=0.3 and M=0.6). Placing the step at d_u=0.5d seems to improve effectiveness upstream - except for the M=0.3 case.

However, for all cases, positioning the step immediately upstream of the holes (du = 0 such that it is tangent to the holes) yields the most significant enhancement in effectiveness. This effect is illustrated in Fig.64(b). Introducing any upstream step seems to have a negative impact on the effectiveness at larger values of x/d ($>$10). This could be attributed to the flow disturbance created by the step, enhancing mixing further downstream.

Effect of width of upstream step (w). Changing the the width of the upstream step (w) in the range 3.75d to 15d did not show any effect on the film cooling effectiveness. (Fig.61) This seems to indicate that the contraction occurring upstream due to the forward facing step is much less significant compared to the effect of the backward facing step.

Effect of placing the step downstream of film cooling hole.

Placing the step downstream of the hole (Fig. 63) seems to have a positive effect

on the film cooling effectiveness - especially at high blowing ratios. Placing the step both upstream and downstream is similar to the trench geometry studied by Waye et al. [80]. Using both the upstream and the downstream step seems to improve the effectiveness at small values of x/d (¡0) due the upstream step and at moderate values of x/d (0 ¡x/d ¡5) due to the downstream step. Fig. 63 seems to indicate that the effect of the upstream and downstream steps is additive.

5.   Experimental Uncertainties

The Kline - McClintock scheme [27] has been used to determine the experimental uncertainties involved in determining the film cooling effectiveness. The uncertainties depend strongly on the local reference intensity - the better illuminated a point on the plate, the lesser the corresponding experimental uncertainty. For the current experimental case, the uncertainty for an effectiveness level of 0.2 works out 0.025 units. Uncertainties in the coolant flow rate and the mainstream flow of the order of 1-2%.

6.   Conclusions

Tests have been run characterizing the effect of a step upstream of the film cooling holes on a flat plate using the steady state Pressure Sensitive Paint Technique.

- The step is found to have a positive impact on the film cooling effectiveness for both simple angled and compound angled cylindrical holes in the region near the holes. The effect on the compound angled holes is more significant.

- The step, when applied to fan-shaped holes, tends to reduce film cooling effectiveness downstream of the hole. This negative effect is more pronounced in the simple angled case.

- The height of the step and the distance of the backward facing step from the upstream edge of the film cooling holes have a monotonic impact on the film cooling effectiveness (for the range studied in cylindrical holes). The higher the step and closer the step to the holes, the better the effectiveness.

- The width of the step does not have an effect on the film cooling effectiveness.

- Placing a step downstream seems to improve film cooling effectiveness - especially at higher blowing ratios. This study focuses only on one part of the two part problem of determining the heat load reduction due to film cooling holes with an upstream step. Further studies could involve experimentally determining the heat transfer coefficient and also determining the aerodynamic penalty imposed by the step. The effect of the downstream step could also be investigated more thoroughly.

D. High Pressure Turbine Blade Film Cooling Effectiveness Measurements with Unsteady Wake

1. Literature Survey

Blade surface heat transfer coefficient distribution. Rotor blades in a gas turbine engine experience intermittent wakes (typically $0.1 < S < 0.4$) and shocks due to the stator vanes located immediately upstream of the blades. These unsteady phenomena result in hastening the laminar-turbulent transition along the blade surface (bypass transition, [89]). An intermittency based model has been developed by Mayle and Dullenkopf [90] to predict transitional heat transfer along the blade surface. This model, implemented in the STAN5 boundary layer code has been shown to be fairly accurate by Han et al. [91] and Zhang and Han [92]. Transition to turbulence is

further hastened by the provision of film cooling holes, as reported by Mehendale et al. [93].

Guenette et al. [94] conducted a study using a scaled rotor-stator arrangement in the MIT blow-down facility and concluded that data acquired using a spoke-wheel type wake generator at Oxford [95] offers qualitatively similar heat transfer coefficients on the suction side. Since then, spoke-wheel wake generators have been used widely in literature to simulate the effect of the upstream stator wake, e.g. Zhang and Han [92] and Funazaki et al.[96].

More recently, experimental methods with better spatial resolution (LDV and traversing hot-wires) have been used to measure the phase averaged structure of the wake. Data of Stieger and Hodson [97] and Bijak-Bartosik and Elsner [98] shows flow-field inside the passage between two rotor blades due to a spoke wheel wake generator. An increase in turbulent kinetic energy along the suction surface is measured due to the wake. These measurements further confirm the picture of laminar-turbulent transition built in the literature.

Effect of turbulence and unsteady Wake. Several studies on a linear cascade with rotating a spoke-wheel wake generator installed upstream of a typical high pressure film cooled model turbine blade have been conducted in the Turbine Heat Transfer Lab at Texas A&M University. Mehendale et al. [93] presented film cooling effectiveness data on the blade surface (equipped with radial angled holes on the leading edge, two rows of simple angled holes on the suction side, and two rows of compound angled holes on the pressure side). A reduction in film cooling effectiveness due to the unsteady wake is observed across the board. Du et al. [99] acquired film cooling effectiveness data on the same configuration using thermochromic liquid crystals, and observed consistent trends with earlier work. Teng et al. [100] used cold-wire anemometry to measure the mean and fluctuating temperature profiles within the

film cooling jet. Increased turbulence in the boundary layer can be clearly observed in the unsteady wake case, which results in shorter coolant traces.

Experiments on the blade surface in a cascade characterizing the unsteady wake effect on leading edge film cooling have been conducted by Funazaki et al. [96] and Heidmann et al. [101]. A significant Strouhal number effect was identified by the researchers in both cases - and the conclusions were similar.

2. Objectives

The current work provides a comprehensive parametric study of film cooling effectiveness on a typical high pressure model rotor blade, with seven film cooling hole rows with an upstream spoke wheel wake generator to simulate the unsteady stator wake effect (for up to S = 0.36). Prior stuidies on this and other blades restricted the blowing ratios on the pressure side to less than 2.0. This study, more realistic blowing ratios of up to 4.0 are studied on the pressure side and 2.0 on the suction side. Also, the density ratios studied range up to 2.5, which is more representative of ratios encountered in actual engines.

The PSP mass transfer analogy, expanded to cover higher density ratios (based on the work of Narzary et al. [70] and Charbonnier et al. [69]) is used to present high-resolution conduction error-free film cooling effectiveness data on the entire mid-span portion of the blade.

The experimental details and results are detailed in the forth-coming paper, [71].

CHAPTER VI

SUMMARY

The first aspect of this study focuses on the internal cooling of gas turbine blades and vanes under stationary conditions. Studies are conducted at high Reynolnds numbers, as would be pertinent to internal flows inside land-based turbine blades/vanes, which are physically larger in size. Correlations for rib-turbulated heat transfer coefficients and friction factors have been developed in prior literature for lower Reynolds numbers with an emphasis on aviation gas turbine engine.

Using the copper-plate regional average method, the prior correlations have been successfully extended to higher Reynolds numbers. Various paremetric dependencies (rib height, shape and spacing) have been studied, and a comprehensive database has been generated. These results can be used by turbine designers for estimating heat transfer in turbine stators, as well as a base-line for estimating the heat tranfer in rotor blades. Results show a significant deterioration thermal performace at higher Reynolds numbers for the rib heights studied.

The second aspect of this study focuses on extending acquried stationary data to a rotating frame of reference. The effect of rotation has been studied numerically (Chapter 2) and experimentally (Chapter 3). A typical three-pass serpentine channel is simulated using a commercially available CFD program (FLUENT). The interaction of viscous, intertial, Coriolis and buoyancy forces results in a very complicated asymmetric turbulent flow-field. Asymmetries are noticed between leading and trailing sides due to secondary circulations induced by the Coriolis force. Further, recirculaltions induced by the centrifugal buoyancy forces are observed.

Heat transfer in a rotating frame of reference is measured in a model rotating trailing edge with pin-fins and flow ejection. The trailing edge is inclined at 45 degrees

to the plane of rotation - as is typical of a rotor trailing edge. Measurements are performed using the copper-plate regional average method, with communication to the rotating frame of reference using a slip-ring assembly. Results show a deterioration of heat transfer on the leading surface and an increase on the trailing surface. These differences are more subdued when roughness elements are introduced - which and be explained by the rearrangement of the secondary flow structures.

Modern gas tubine blades and vanes are also cooled externally by the film cooling technique wherein relatively cool and dense coolant, ejected through specifically drilled film cooling holes forms an insulating film on the blade surface protecting it from the hot mainstream. A metric of how well the film protects the blade from the hot gases is the film cooling effectiveness.

Film cooling effectivness is measured for two configurations: a flat plate and a heavily loaded turbine blade using the mass-transfer analogy based pressure sensitive paint method. This method yields high fidelity film cooling effectivness contour data. Parameters for the flat plate study include hole shape and coolant to mainstream mass flux ratio. In addition to these parameters, the effect of a step upstream of a row of film cooling holes is tested. A large positive effect of the step is found, specifically for compound angled cylindrical holes. This positive effect is due to the entrapment of the coolant in the low-pressure recirculation zone of the backward facing step. For fan-shaped holes, however, the effect of the is found to be negative.

For the high pressure turbine blade, parameters studied include coolant-to-mainstream mass-flux and density ratios and rotor-stator interactions (by a rotating spoke wheel). The rotating spoke wheel represents the stator - and the stationary blade represents the rotor. This simulates the relative motion between rotor and stator, as experienced in the engine. The film cooling effectiveness was found to depend strongly on the density ratio - with higher density coolants usually resulting in higher average

film cooling effectiveness values. The simulated rotor-stator interactions resulted in increased local turbulence intensities - and therefore, shorter effectiveness traces due to better mixing of the film with the hot mainstream.

Film cooling was found to be very sensitive to a variety of different parameters. Future work could focus on the determination of local heat transfer coefficients using another analogy based method, yielding high fidelity data.

REFERENCES

[1] M. Boyce, Gas turbine engineering handbook, Gulf Professional Publishing, Houston, 2006.

[2] N. Cumpsty, Preparing for the future: reducing gas turbine environmental impact, in: Proceedings of Turbo Expo 2009, Paper: GT2009-60367, Orlando, FL, United States, 2009.

[3] M. K. Chyu, S. C. Siw, V. G. Karaivanov, W. S. Slaughter, M. A. Alvin, Aerothermal challenges in syngas, hydrogen-fired, and oxyfuel turbines—part ii: Effects of internal heat transfer, Journal of Thermal Science and Engineering Applications 1 (1) (2009) 011003. doi:10.1115/1.3159480.

[4] J. Han, Heat transfer and friction characteristics in rectangular channels with rib turbulators, Journal of Heat Transfer 110 (1988) 321–330.

[5] J. Han, J. Park, Developing heat transfer in rectangular channels with rib turbulators, International Journal of Heat and Mass Transfer 31 (1) (1988) 183–195.

[6] J. Park, J. Han, S. Ou, R. Boyle, Heat transfer comparisons of five different rectangular channels with parallel angled ribs, International Journal of Heat and Mass Transfer 35 (11) (1992) 2891–2903.

[7] M. Taslim, T. Li, S. Spring, Measurements of heat transfer coefficients and friction factors in rib-roughened channels simulating leading-edge cavities of a modern turbine blade, Journal of Turbomachinery 119 (1997) 601–610.

[8] Y. Zhang, W. Gu, J. Han, Augmented heat transfer in triangular ducts with full and partial ribbed walls, Journal of Thermophysics and Heat Transfer 8 (3) (1994) 574–579.

[9] R. Kiml, S. Mochizuki, A. Murata, Effects of rib arrangements on heat transfer and flow behavior in a rectangular rib-roughened passage: Application to cooling of gas turbine blade trailing edge, Journal of Heat Transfer 123 (4) (2001) 675–681.

[10] M. Stephens, M. Chyu, T. Shih, Calculations and measurements of heat transfer in a square duct with inclined ribs, in: AIAA, ASME, SAE, and ASEE, Joint Propulsion Conference and Exhibit, 32 nd, Lake Buena Vista, FL, 1996.

[11] G. Su, H. Chen, J. Han, J. Heidmann, Computation of flow and heat transfer in rotating two-pass rectangular channels (AR= 1: 1, 1: 2, and 1: 4) with smooth walls by a Reynolds stress turbulence model, International Journal of Heat and Mass Transfer 47 (26) (2004) 5665–5683.

[12] M. Taslim, A. Lengkong, 45 deg staggered rib heat transfer coefficient measurements in a square channel, Journal of Turbomachinery 120 (1998) 571–579.

[13] J. C. Bailey, R. S. Bunker, Heat transfer and friction in channels with very high blockage 45[degree] staggered turbulators, ASME Conference Proceedings 2003 (36886) (2003) 451–458. doi:10.1115/GT2003-38611.
URL http://link.aip.org/link/abstract/ASMECP/v2003/i36886/p451/s1

[14] S. Lau, R. Kukreja, R. McMillin, Effects of V-shaped rib arrays on turbulent heat transfer and friction of fully developed flow in a square channel, International Journal of Heat and Mass Transfer 34 (7) (1991) 1605–1616.

[15] J. Han, Y. Zhang, C. Lee, Augmented heat transfer in square channels with parallel, crossed, and V-shaped angled ribs, Journal of Heat Transfer 113 (3) (1991) 590–596.

[16] J. Han, Y. Zhang, High performance heat transfer ducts with parallel broken and V-shaped broken ribs, International Journal of Heat and Mass Transfer 35 (1992) 555–562.

[17] M. Taslim, S. Spring, Effects of turbulator profile and spacing on heat transfer and friction in a channel, Journal of Thermophysics and Heat Transfer 8 (3) (1994) 555–562.

[18] J. Han, L. Glicksman, W. Rosenhow, An investigation of heat transfer and friction factor for rib-roughened surfaces, International Journal of Heat and Mass Transfer 21 (3) (1978) 555–562.

[19] P. Chandra, M. Fontenot, J. Han, Effect of rib profiles on turbulent channel flow heat transfer, Journal of Thermophysics and Heat Transfer 12 (1) (1998) 116–118.

[20] D. Dipperey, R. Sabersky, Heat and momentum transfer in smooth and rough tube at various prandtl numbers, International Journal of Heat and Mass Transfer 6 (1963) 329–353.

[21] J. Han, Heat transfer and friction in channels with two opposite rib-roughened walls, Journal of Heat Transfer 106 (4) (1984) 774–781.

[22] W. Kays, M. Crawford, B. Weigand, Convective Heat and Mass Transfer, McGraw-Hill, New York, 2005.

[23] S. Pope, Turbulent flows, Cambridge Univ. Press, London, 2008.

[24] L. Moody, Friction factors for pipe flow, Trans. ASME 66 (8) (1944) 671–677.

[25] J.-C. Han, J. S. Park, C. K. Lei, Heat transfer and pressure drop in blade cooling channels with turbulence promoters, Tech. Rep. 3837, NASA (1984).

[26] J.-C. Han, J. S. Park, M. Y. Ibrahim, Measurement of heat transfer and pressure drop in rectangular channels with turbulence promoters, Tech. Rep. 4015, NASA (1986).

[27] S. Kline, F. McClintock, Describing uncertainties in single-sample experiments, Mechanical Engineering 75 (1) (1953) 3–8.

[28] J. Wagner, B. Johnson, F. Kopper, Heat transfer in rotating serpentine passages with smooth walls, Journal of Turbomachinery 113 (1991) 321–330.

[29] J. Wagner, B. Johnson, R. Graziani, F. Yeh, Heat transfer in rotating serpentine passages with trips normal to the flow, Journal of Turbomachinery 114 (1992) 847–853.

[30] B. Johnson, J. Wagner, G. Steuber, F. Yeh, Heat transfer in rotating serpentine passages with trips skewed to the flow, Journal of Turbomachinery 116 (1994) 113–121.

[31] B. Johnson, J. Wagner, G. Steuber, F. Yeh, Heat transfer in rotating serpentine passages with selected model orientations for smooth or skewed trip walls, Journal of Turbomachinery 116 (1994) 738–745.

[32] J. Guidez, Study of the convective heat transfer in a rotating coolant channel, Journal of Turbomachinery 111 (1) (1989) 43–50.

[33] F. Willett, A. Bergles, Heat transfer in rotating narrow rectangular pin-fin ducts, Experimental Thermal and Fluid Science 25 (7) (2002) 573–582.

[34] L. Wright, E. Lee, J. Han, Effect of rotation on heat transfer in rectangular channels with pin fins, Journal of Thermophysics and Heat Transfer 18 (2) (2004) 263–272.

[35] W. Fu, L. Wright, J. Han, et al., Rotational buoyancy effects on heat transfer in five different aspect-ratio rectangular channels with smooth walls and 45 degree ribbed walls, Journal of Heat Transfer 128 (2006) 1130–1140.

[36] Y. Liu, M. Huh, J. Han, S. Chopra, Heat transfer in a two-pass rectangular channel (AR= 1: 4) under high rotation numbers, Journal of Heat Transfer 130 (2008) 081701.

[37] Y. Liu, M. Huh, D. Rhee, J. Han, H. Moon, Heat transfer in leading edge, triangular shaped cooling channels with angled ribs under high rotation numbers, Journal of Turbomachinery 131 (2009) 041017.

[38] S. Dutta, M. J. Andrews, J.-C. Han, Prediction of turbulent heat transfer in rotating smooth square ducts, International Journal of Heat and Mass Transfer 39 (12) (1996) 2505 – 2514. doi:http://dx.doi.org/10.1016/0017-9310(95)00319-3.

[39] T. Shih, Y. Lin, M. Stephens, M. Chyu, K. Civinskas, Flow and heat transfer in a ribbed U-duct under typical engine conditions, in: ASME Paper 98-GT-213, 1998.

[40] A. Sleiti, J. Kapat, Fluid flow and heat transfer in rotating curved duct at high rotation and density ratios, Journal of Turbomachinery 127 (2005) 659–665.

[41] Fluent Inc, Lebanon, NH, User's Manual (2006).

[42] D. Metzger, S. Haley, Heat transfer experiments and flow visualization for arrays of short pin fins, in: American Society of Mechanical Engineers, International Gas Turbine Conference and Exhibit, 27th, London, England, Apr. 18-22, 1982, Paper: 82-GT-138, 1982.

[43] R. Goldstein, M. Chyu, R. Hain, Measurement of local mass transfer on a surface in the region of the base of a protruding cylinder with a computer-controlled data acquisition system, Int. J. Heat and Mass Transfer 28 (5) (1985) 977–985.

[44] M. Chyu, V. Natarajan, Heat transfer on the surface of three-dimensional protruding elements, Int. J. Heat and Mass Transfer 39 (1996) 2–11.

[45] G. VanFossen, Heat transfer coefficients for staggered arrays of short pin fins, NASA STI/Recon Technical Report N 81.

[46] M. Chyu, Y. Hsing, V. Natarajan, Convective heat transfer of cubic fin arrays in a narrow channel, Journal of Turbomachinery 120 (1998) 362–367.

[47] D. Metzger, C. Fan, S. Haley, Effects of pin shape and array orientation on heat transfer and pressure loss in pin fin arrays, Journal of engineering for power 106 (1) (1984) 252–257.

[48] F. E. Ames, L. A. Dvorak, Turbulent transport in pin-fin arrays: experimental data and predictions, Journal of Turbomachinery 128 (1) (2006) 71–81. doi:10.1115/1.2098792.

[49] M. Chyu, Y. Hsing, T. Shih, V. Natarajan, Heat transfer contributions of pins and endwall in pin-fin arrays: effects of thermal boundary condition modeling, Journal of Turbomachinery 121 (1999) 257.

[50] D. Metzger, W. Shepard, S. Haley, Row resolved heat transfer variations in pin-fin arrays including effects of non-uniform arrays and flow convergence, in: ASME, International Gas Turbine Conference and Exhibit, 31st, Duesseldorf, West Germany, June 8-12, 1986. 9 p., Paper No:86-GT-132, 1986.

[51] M. Chyu, Heat-transfer and pressure-drop for short pin-fin arrays with pin-endwall fillet, Journal of Heat Transfer 112 (4) (1990) 926–932.

[52] S. Arora, W. Abdel-Messeh, Characteristics of partial length circular pin fins as heat transfer augmentors for airfoil internal cooling passages, Journal of Turbomachinery 112 (1990) 559–565.

[53] S. Lau, J. Han, T. Batten, Heat transfer. pressure drop, and mass flow rate in pin fin channels with long and short trailing edge ejection holes, Journal of Turbomachinery 111 (1989) 116–123.

[54] T. Kumaran, J. Han, S. Lau, Augmented heat transfer in a pin fin channel with short or long ejection holes, Int. J. Heat and Mass Transfer 34 (1991) 2617–2628.

[55] J.-J. Hwang, D.-Y. Lai, Y.-P. Tsia, Heat transfer and pressure drop in pin-fin trapezoidal ducts, Journal of Turbomachinery 121 (2) (1999) 264–271. doi:10.1115/1.2841310.

[56] J.-J. Hwang, C. Lu, Lateral-flow effect on endwall heat transfer and pressure drop in a pin-fin trapezoidal duct of various pin shapes, Journal of Turbomachinery 123 (2001) 133–141.

[57] S. Chang, T. Yang, G. F. Hong, T. Liou, Heat transfer in radially rotating pin-fin channel at high rotation numbers, in: American Society of Mechanical Engineers, International Gas Turbine Conference and Exhibit, Berlin, Germany, June 9-13, 2008, Paper: GT2008-50514, 2008.

[58] L. Wright, Y. Liu, J. Han, S. Chopra, Heat transfer in trailing edge, wedge-shaped cooling channels under high rotation numbers, in: American Society

of Mechanical Engineers, International Gas Turbine Conference and Exhibit, Montreal, Canada, May 14-17, 2007, Paper: GT2007-27093, 2007.

[59] Y.-H. Liu, M. Huh, L. M. Wright, J.-C. Han, Heat transfer in trailing-edge channels with slot ejection under high rotation numbers, Journal of Thermophysics and Heat Transfer 23 (2) (2009) 305 – 315. doi:http://dx.doi.org/10.2514/1.37982.

[60] S. Chang, T. Liou, S. Chiou, F. Chang, High rotation number heat transfer on rotating trapezoidal duct with 45-deg staggered ribs and bleeds from apical side wall, in: American Society of Mechanical Engineers, International Gas Turbine Conference and Exhibit, Montreal, Canada, May 14-17, 2007, Paper: GT2007-28174, 2007.

[61] R. Moffat, Turbine blade cooling, in: Heat transfer and fluid flow in rotating machinery; Proc. First International Symposium on Transport Phenomena, Honolulu, HI, Apr. 28-May 3, 1987, pp. 3–26.

[62] R. Goldstein, Film cooling, Advances in Heat Transfer 7 (1971) 321–379.

[63] J. Han, S. Dutta, S. Ekkad, Gas turbine heat transfer and cooling technology, Taylor and Francis, New York, 2000.

[64] T. Jones, Theory for the use of foreign gas in simulating film cooling, International Journal of Heat and Fluid Flow 20 (3) (1999) 349–354.

[65] T. Liu, M. Guille, J. Sullivan, Accuracy of pressure-sensitive paint, AIAA journal 39 (1) (2001) 103–112. doi:10.2514/2.1276.

[66] L. Zhang, R. Jaiswal, Turbine nozzle endwall film cooling study using Pressure-Sensitive Paint, Journal of Turbomachinery 123 (2001) 730–735.

doi:10.1115/1.1400113.

[67] S. Mhetras, J. C. Han, R. Rudolph, Effect of flow parameter variations on full coverage film-cooling effectiveness disribution on a gas turbine blade with compound shaped holes, in: Proceedings of the ASME Turbo Expo 2007, Paper GT2007-27071, Montreal, Canada, 2007.

[68] J. Ahn, M. Schobeiri, J. C. Han, H. Moon, Film cooling effectiveness on the leading edge region of a rotating turbine blade with two rows of film cooling holes using pressure sensitive paint, Journal of Heat Transfer 128 (2006) 879–888.

[69] D. Charbonnier, P. Ott, M. Jonsson, F. Cottier, T. Kobbe, Experimental and numerical study of the thermal performance of a film cooled turbine platform, in: Proceedings of Turbo Expo 2009 Paper: GT2009-60306, Orlando, FL, United States, 2009.

[70] D. P. Narzary, K.-C. Liu, J. C. Han, Influence of coolant density on turbine blade platform film-cooling, in: American Society of Mechanical Engineers Turbo Expo, GT2009-59342, 2009.

[71] A. Rallabandi, S. Li, H. J.C., Unsteady wake and coolant density effects on turbine blade film cooling using PSP technique, in: Proc. Fourtreeth International Heat Transfer Conference, Washington, DC, Paper No: IHTC14-22911, ASME, 2010.

[72] A. K. Sinha, D. Bogard, M. Crawford, Film-cooling effectiveness downstream of a single row of holes with variable density ratio, Journal of Turbomachinery 113 (3) (1991) 442–449. doi:10.1115/1.2927894.

[73] S. Ekkad, D. Zapata, J. Han, Film effectiveness over a flat surface with air and CO2 injection through compound angle holes using a transient liquid crystal image method, Journal of Turbomachinery 119 (1997) 587–595.

[74] R. J. Goldstein, P. Jin, Film cooling downstream of a row of discrete holes with compound angle, Journal of Turbomachinery 123 (2) (2001) 222–230. doi:10.1115/1.1344905.

[75] L. M. Wright, Z. Gao, T. A. Varvel, J. C. Han, Assessment of steady state psp, tsp, and ir measurement techniques for flat plate film cooling, in: Proceedings of the ASME Summer Heat Transfer Conference, Paper: HT2005-72363, San Francisco, CA, United States, 2005.

[76] M. I. Ethridge, J. M. Cutbirth, D. G. Bogard, Scaling of performance for varying density ratio coolants on an airfoil with strong curvature and pressure gradient effects, Journal of Turbomachinery 123 (2) (2001) 231–237. doi:10.1115/1.1343457.

[77] R. J. Goldstein, E. R. G. Eckert, F. Burggraf, Effects of hole geometry and density on three-dimensional film cooling, International Journal of Heat and Mass Transfer 17 (5) (1974) 595 – 607. doi:DOI: 10.1016/0017-9310(74)90007-6.

[78] K. Thole, M. Gritsch, A. Schulz, S. Wittig, Flowfield measurements for film-cooling holes with expanded exits, Journal of Turbomachinery 120 (1998) 327–336.

[79] R. Bunker, A review of shaped hole turbine film-cooling technology, Journal of Heat Transfer 127 (2005) 441–451. doi:10.1115/1.1860562.

[80] S. Waye, D. Bogard, High-resolution film cooling effectiveness measurements of axial holes embedded in a transverse trench with various trench configurations, Journal of Turbomachinery 129 (2007) 294–301.

[81] R. S. Bunker, Film cooling effectiveness due to discrete holes within a transverse surface slot, ASME Conference Proceedings 2002 (36088) (2002) 129–138. doi:10.1115/GT2002-30178.
URL http://link.aip.org/link/abstract/ASMECP/v2002/i36088/p129/s1

[82] K. Harrison, J. Dorrington, J. Dees, D. Bogard, R. Bunker, Turbine airfoil net heat flux reduction with cylindrical holes embedded in a transverse trench, Journal of Turbomachinery 131 (2009) 011012.

[83] S. Na, T. Shih, Increasing adiabatic film-cooling effectiveness by using an upstream ramp, Journal of Heat Transfer 129 (2007) 464–471.

[84] G. Barigozzi, G. Franchini, A. Perdichizzi, The effect of an upstream ramp on cylindrical and fan-shaped hole film cooling-Part II: adiabatic effectiveness results, in: Proceedings of the ASME Turbo Expo, American Society of Mechanical Engineers, 2007, pp. 115–125.

[85] W. Nicoll, J. Whitelaw, The effectiveness of the uniform density, two- dimensional wall jet(Two-dimensional wall jet effectiveness measurements and calculation procedures for injection conditions), International Journal of Heat and Mass Transfer 10 (1967) 623–639. doi:10.1016/0017-9310(67)90109-3.

[86] Z. Gao, D. Narzary, S. Mhetras, J. Han, Full-coverage film cooling for a turbine blade with axial-shaped holes, Journal of Thermophysics and Heat Transfer 22 (1) (2008) 50–58.

[87] Z. Gao, D. Narzary, J. Han, Film-cooling on a gas turbine blade pressure side or suction side with compound angle shaped holes, Journal of Turbomachinery 131 (2009) 011019.

[88] A. P. Rallabandi, J. Grizzle, J. C. Han, Effect of upstream step on flat plate film cooling effectiveness using psp, in: 2008 Proceedings of the ASME Summer Heat Transfer Conference, HT08-56194, Vol. 2, Jacksonville, FL, United States, 2008, pp. 599 – 609.

[89] R. Mayle, The role of laminar-turbulent transition in gas turbine engines, Journal of Turbomachinery 113 (1991) 509–537.

[90] R. Mayle, K. Dullenkopf, A theory for wake-induced transition, Journal of Turbomachinery 112 (1990) 188–197.

[91] J. Han, L. Zhang, S. Ou, Influence of unsteady wake on heat transfer coefficient from a gas turbine blade, Journal of Heat Transfer 115 (4) (1993) 904–911.

[92] L. Zhang, J. Han, Combined effect of free-stream turbulence and unsteady wake on heat transfer coefficients from a gas turbine blade, Journal of Heat Transfer 117 (1995) 296–302.

[93] A. Mehendale, J. Han, S. Ou, C. Lee, Unsteady wake over a linear turbine blade cascade with air and CO2 film injection: Part II Effect on film effectiveness and heat transfer distributions, Journal of Turbomachinery 116 (1994) 730–740.

[94] G. Guenette, A. Epstein, M. Giles, R. Haimes, R. Norton, Fully scaled transonic turbine rotor heat transfer measurements, Journal of Turbomachinery 111 (1) (1989) 1 – 7.

[95] D. Doorly, M. Oldfield, Simulation of the effects of shock wave passing on a turbine rotor blade, Journal of Engineering for Gas Turbines and Power 107 (4) (1985) 998–1006.

[96] K. Funazaki, M. Yokota, S. Yamawaki, Effect of periodic wake passing on film effectiveness of discrete cooling holes around the leading edge of a blunt body, Journal of Turbomachinery 119 (2) (1997) 292–301. doi:10.1115/1.2841112.

[97] R. Stieger, H. Hodson, The unsteady development of a turbulent wake through a downstream low-pressure turbine blade passage, Journal of Turbomachinery 127 (2005) 388–395.

[98] E. Bijak-Bartosik, W. Elsner, Investigation of wake transport in a turbine blade channel and its effect on the bounday layer development, in: ASME, International Gas Turbine Conference and Exhibit, Orlando, Florida, June 8-12, 2009, Paper: GT2009-59123, 2009.

[99] H. Du, S. Ekkad, J. Han, Effect of unsteady wake with trailing edge coolant ejection on detailed heat transfer coefficient distributions for a gas turbine blade, Journal of Heat Transfer 119 (1997) 242–252.

[100] S. Teng, D. Sohn, J. Han, Unsteady wake effect on film temperature and effectiveness distributions for a gas turbine blade, Journal of Turbomachinery 122 (2000) 340–346.

[101] J. Heidmann, B. Lucci, E. Reshotko, An experimental study of the effect of wake passing on turbine blade film cooling, Journal of Turbomachinery 123 (2001) 214–221.

VITA

Name:	Akhilesh Prabhakar Rallabandi
Address:	c/o Dr. Je-Chin Han,
	Department of Mechanical Engineering,
	TAMU 3123, College Station, TX, 77843-3123
Email:	akhlsh@tamu.edu
Education:	B.Tech. Mechanical Engineering, IIT Madras, India, 2004
	M.Tech. Mechanical Engineering, IIT Madras, India, 2005
	Ph.D. Mechanical Engineering, Texas A&M University, USA, 2010

The typist for this thesis was Akhilesh Rallabandi.